IEM JOURNAL

THE JOURNAL OF
THE INSTITUTION OF ENGINEERS, MALAYSIA

KDN PP5476/10/2010 (026477)
ISSN 0126-513X

Vol. 71, No.2
June 2010

THE INSTITUTION OF ENGINEERS, MALAYSIA
Bangunan Ingenieur, Lots 60 & 62, Jalan 52/4, P.O.Box 223, (Jalan Sultan) 46720 Petaling Jaya, Selangor.
Tel: 03-7968 4001/4002 Fax: 03-7957 7678 E-mail: sec@iem.org,my Homepage: http://www.iem.org.my

Vol. 71, No.2, June 2010
KDN PP5476/10/2010 (026477) ISSN 0126-513X

THE INSTITUTION OF ENGINEERS, MALAYSIA
Bangunan Ingenieur, Lots 60 & 62, Jalan 52/4, P.O.Box 223 (Jalan Sultan), 46720 Petaling Jaya, Selangor Darul Ehsan.
Tel: 03-7968 4001/4002 Fax: 03-7957 7678
E-mail: sec@iem.org.my Homepage: http://www.iem.org.my

Printed by: **WISE ORGANISATION (M) SDN. BHD.** (888671-H)
No. 5, Jalan Industri PBP 11, Taman Industri Pusat Bandar Puchong, 47100 Puchong, Selangor Darul Ehsan.
Tel: 603-5891 7363 Fax: 603-5891 7232
E-mail: weprint.wise@gmail.com

CONTENTS

ADVISORY PANELS

SUBSCRIPTIONS

To subscribe Journal of IEM please contact

DIMENSION PUBLISHING SDN BHD (449732-T)
Suite 29, 3A Floor, IOI Business Park,
1 Persiaran Puchong Jaya Selatan,
Bandar Puchong Jaya, 47170 Puchong,
Selangor Darul Ehsan, Malaysia.
Tel: (603) 8070 9949
Fax: (603) 8070 0047
Email: info@dimensionpublishing.com
Website: www.dimensionpublishing.com

PUBLICATION DISCLAIMER

COPYRIGHT

We are pleased to announce that the articles in the IEM Journals have been indexed by other organisation *i.e. Linda Hall Library of Science, Engineering and Technology, Kansas City.*

EXPERIMENTAL EVALUATION OF THE STATIC AND DYNAMIC CHARACTERISTICS OF AN OFFSHORE CRANE MODEL

(Date received: 24.10.2008)

T. L. Chan[1], J. I. Inayat-Hussain[2], K. S. Teoh[1] and Y. T. Liew[3]
[1]School of Engineering, Monash University, Jalan Lagoon Selatan, 46150 Bandar Sunway, Selangor Darul Ehsan
[2]College of Engineering, Universiti Tenaga Nasional, Km 7 Jalan Kajang-Puchong, 43009 Kajang, Selangor Darul Ehsan
[3]Favelle Favco Berhad, Lot 586, 2nd Mile, Jalan Batu Tiga Lama, 41300, Klang, Selangor Darul Ehsan
E-mail: [1]tlcha6@student.monash.edu

ABSTRACT

The knowledge of the static and dynamic characteristics of cranes is of utmost importance in their design and construction in order to optimise the construction material costs as well as to optimize their response to static and dynamic loadings during operation. Although numerical simulation of the crane response subjected to various loading conditions are routinely undertaken in the design stage, experimental verification of these numerical results are rarely performed due to the high cost involved. Experimental verification of the static and dynamic characteristics of these cranes can however be performed at a significantly lower cost on their scaled-down models. The results from the scaled-down models provide useful insights into the static and dynamic performance of these cranes. In the work presented herein, a scaled-down model of a boom angle luffing crane prototype, typically employed in offshore engineering applications, was developed using dimensionless p parameters. The model, which has geometric and dynamic similarities with the prototype, was numerically and experimentally examined for its static and dynamic characteristics. The numerical analysis of the model was undertaken using a commercially available finite-element computer program, ANSYS. This program was utilized to compute the stiffness and stresses in the model subjected to static loads, as well as the natural frequencies and mode shapes, which represent the dynamic characteristics of the model. An experimental rig was fabricated based on the scaled-down model, and measurements were performed to verify the computational results obtained from the finite-element analysis. The static strains measured at various positions on the boom were found to be within 14% of those obtained numerically. The natural frequencies and mode shapes of the model crane were obtained using modal testing technique and were found to be in good agreement to those obtained numerically, with discrepancies within 3% for the first three modes.

Keywords: *Dynamic Characteristics, Finite-element Analysis, Modal Testing, Offshore Crane and Static*

1.0 INTRODUCTION

In the design and construction of cranes the knowledge of their static and dynamic characteristics are of significant importance to optimize the construction material costs, their response to static loading due to suspension of the payload at different boom angles, and their response to dynamic loading due to acceleration of the payload during lifting and lowering operations. Offshore cranes in particular, are subjected to dynamic loading arising from ocean waves that cause the payload to rise and fall following the movement of these waves. The movement of these waves creates a relative velocity between the boom tip and the load, which in turn causes the boom to vibrate. The design of cranes requires the information on their dynamic properties, namely the natural frequencies and mode shapes. This information is essential for the development of suitable loading charts for the cranes [1] as well as for the incorporation of vibration absorbers in the design of these cranes [2].

Although numerical simulation of the crane response subjected to various static and dynamic loading conditions are routinely undertaken in the design stage, experimental verification of these numerical results are rarely performed due to the high cost involved. Experimental verification of the static and dynamic characteristics of these cranes can however be performed at a significantly lower cost on their scaled-down models. The results from the scaled-down models provide useful insights into the static and dynamic performance of these cranes.

Andreu *et al*. [3] employed the finite-element method to create deformable catenary elements that were used to simulate cable net systems by combining multiple elements. In order to create a more realistic model for a mobile crane, Sun *et al.* [4] coupled the drive system of the hoist along with the boom, which was modeled using nonlinear elements for the ropes and Timoshenko beam elements for the truss lattice structure. The cross section of the beam element for the boom was selected so that its stiffness was equivalent to the section of the truss lattice structure. Ju and Choo [5, 6] modeled a boom angle luffing crane using parameterised super elements to represent the 1 cabling system where the cable was modeled as a single element, and the cable passage over the pulleys was represented as a new degree of freedom. The boom and mast were represented as planar frame elements as the emphasis of the work was on the performance of the cable system. Wu *et al.* [7] and Wu [8,9] used finite-element method to model a gantry crane subjected to time varying loads. Shape functions were used to determine the location and magnitude of the force acting on the beam.

While computer simulations provide a convenient method of predicting the behavior of complex systems such as the dynamic characteristic of a crane, they are only as good as the assumptions that are included in the construction of the model. This largely lies in the experience of the modeler and the capabilities of the computer algorithms. Experimental verification can highlight neglected characteristics or underestimated assumptions, which can lead to a better model. Once the model has been successfully verified, it can be used for more complex simulations. For dynamic analysis, verification is carried out using modal identification techniques, which involve extraction of mode shapes and natural frequencies as they are exclusive to individual structures. Wu [8,9] built a 1/10 scaled experimental gantry crane model to verify a similar scaled-down model created using the finite-element method. Various issues that affected the compatibility between the experimental model and the finite-element model were identified. Jerman *et al.* [10] and Jerman [11] used a physical model to verify the characteristics of a slewing crane's mathematical model. The input to both models was via a velocity profile graph. Air friction and slewing ring resistance were also accounted for in these models. Al-Sweiti and Söffker [12] modeled the lower half of a ship mounted boom angle luffing crane using beam element to account for the flexural elasticity of the boom. The upper part of the boom where the rigging of the hoist rope is located was considered as rigid in their model. Their experimental rig was capable of simulating roll conditions through the use of a hydraulic cylinder to swing the entire crane structure. Henry *et al.* [13] used a test rig that was capable of simulating pitch, heave and roll of a ship mounted crane using a Carpal wrist 2 mechanism actuated using servo motors. The test rig was used to investigate the pendulation of the payload in a ship mounted boom angle luffing crane.

In the work presented herein, a numerical model and an experimental test rig that are based on a scaled-down model of a boom angle luffing crane prototype were analysed for compatibility. The scaled-down model was designed to include geometric and dynamic similarities with the prototype. The compatibility analysis was carried out by comparing the static and dynamic behaviour of both models. The numerical analysis of the model was undertaken using the finite-element computer program, ANSYS. This program was utilised to compute the stiffness and stresses in the model subjected to static loads, as well as the natural frequencies and mode shapes, which represent the dynamic characteristics of the model. The experimental rig of the model crane was analysed for its static and dynamic behaviour through static strain load test and frequency response test using an instrumented hammer to obtain its natural frequencies and mode shapes for verification of the computational results obtained from the finite-element analysis.

2.0 DESIGN OF THE SCALED-DOWN MODEL

The main components of the boom angle luffing crane, also known as the critical components [14], are the boom, luff, hoist ropes and the payload. These components determine the stiffness of the crane and were included in the scaled-down model developed in this work, Figure 1. The boom consists of a square hollow section. The vertical stiffness of the beam was designed to be dynamically similar to that of the prototype.

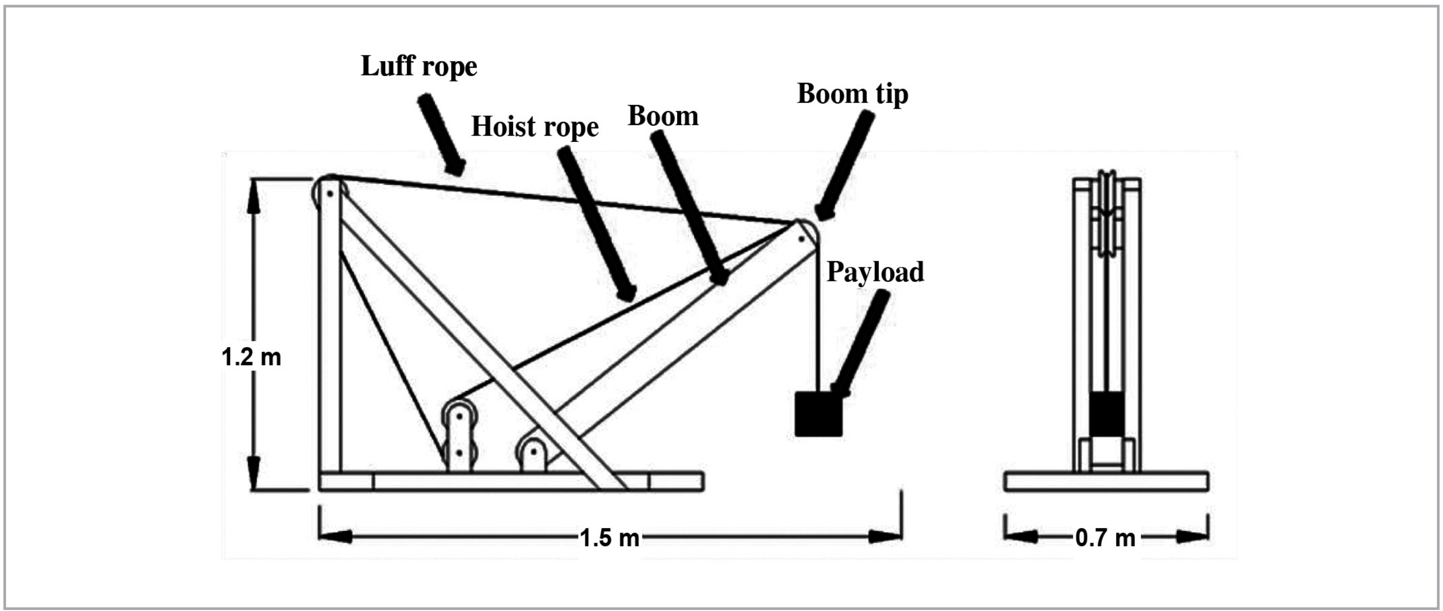

Figure 1: Schematic of the scaled-down model of the offshore boom angle luffing crane

The dimensions of the boom and wire rope stiffness were determined using the dimensionless groups. Three parameters were used to represent the geometry and dynamics of the crane. For geometric similarity, the relative distances between the boom pivot, mast head sheave, boom tip and the hoist and luff rope winch drum were arranged based on the relative distances of the prototype so that the lever arm lengths for the luff ropes and the vertical and inclined hoist ropes of the test rig were in proportion to the lever arm lengths of the full scaled prototype. The dimensionless parameters, which scaled the critical components of the model geometrically, were proposed by Jones [15] and are reproduced in Equations (1) and (2).

The dynamic characteristics of the model to the prototype were scaled using the equation proposed by Wu *et al*. [7] and reproduced in Equation (3). n w represents the natural frequency of the crane system and the variable t represents the time taken for the amplitude of the vibration to reach half of the maximum amplitude. These equations were derived using the Buckingham Pi theorem. To derive Equations (1) and (2), it was assumed that the static behaviour of the crane is a function of the boom length, boom cross sectional area, boom tip displacement, mass of the payload, gravity and force while in to derive Equation (3), it was assumed that the dynamic behaviour of the crane is a function of the displacement, damping ratio, natural frequency, mass, time and force. From the various combinations of dimensionless groups, these three groups were selected based on the availability of information on the behaviour of the crane.

$$\pi_1 = \frac{\textit{Boom tip displacement}}{\textit{Boom length}} \tag{1}$$

$$\pi_2 = \frac{\textit{Boom tip displacement}}{\sqrt{\textit{Boom cross section area}}} \tag{2}$$

$$\pi_3 = \omega_n t \tag{3}$$

The stiffness of the boom angle luffing crane prototype was computed by Lee and Gan [16] by loading their model with a 1 ton force at the maximum boom angle of 85° and calculating the resulting displacement. In order to determine the stiffness of the scaled-down model, iterations were carried out for various boom cross sectional areas and the payload sizes until matching dimensionless values were obtained. Table 1 shows the parameters used to calculate the values of the non dimensional groups. The size of the scaled test load that results in the values for the first and second non-dimensional group was found to be 2 kg and the dimensions of the boom cross section were 12.7 mm by 12.7 mm, with thickness of 0.4 mm. The elasticity of the steel wire rope, consisting of six strands of seven wires, used in the scaled-down model was estimated to be 80 GPa [17]. The resulting values of the non dimensional groups with the said boom dimensions are shown in Table 2. This set of values are the closest obtained from iterative analysis with various payload, rope and boom sizes, which indicates that this is the best scaled model to represent the full scaled prototype.

Table 1: Values of the parameters in the non – dimensional groups

	Model	Prototype
Boom tip displacement (m)	2.81×10^{-4}	0.006
Boom length (m)	1.5	36.6
Boom effective cross section area (m^2)	3.81×10^{-5}	0.01056
Natural frequency (rad/s)	210.5	6.28
Time (s)	0.1	2.5

Table 2: Comparison of the values of the non – dimensional groups between the scaled-downdown model and prototype

	Model	Prototype
$\pi 1$	1.9×10^{-4}	1.6×10^{-4}
$\pi 2$	0.046	0.058
$\pi 3$	21.05	15.7

3.0 NUMERICAL RESULTS

The displacement of the boom tip of the scaled-down model due to static loading was computed using ANSYS for two extreme conditions, *i.e.*, largest boom angle of 85° and smallest boom angle of 20°. These angles are the limits of the luffing angle and are often used for operational tests by crane manufacturers. The loading applied at the boom tip was 19.62 N. The material properties and elements used are shown in Table 3. The boom was modeled using beam elements while the ropes were modeled using single link element each since no lateral vibration was expected along the ropes. Vertical and horizontal displacement constraints were applied at the free nodes of the luff and hoists ropes and the boom while a downward vertical force of 2 kg was applied at the boom tip to simulate the payload. The finite element model is shown in Figure 2.

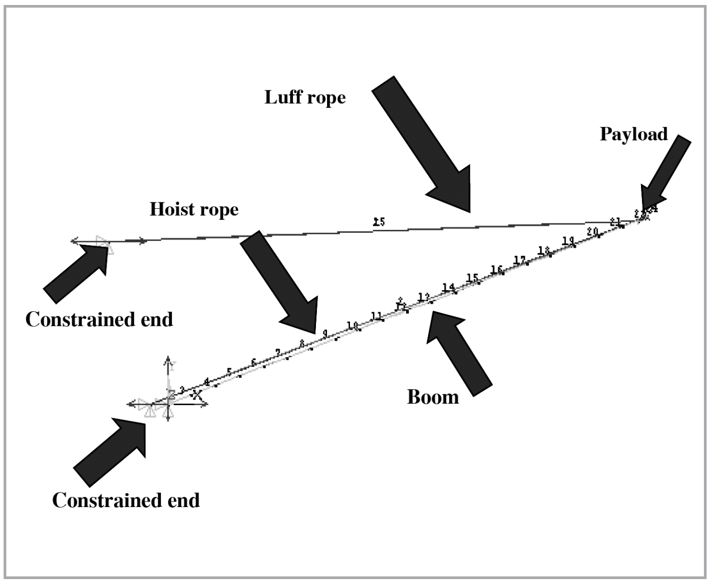

Figure 2: The finite element model at boom angle of 20°

Table 3: Material properties and element used for the crane components

Component	Material properties	Element
Boom	Steel Modulus of Elasticity: 200 GPa Density: 7870 kg/m^3 Poisson Ratio: 0.29	BEAM 3 Euler Bernoulli 3D Beam
Ropes of luff and hoist line	Steel rope Modulus of Elasticity : 80 GPa Density 7870 kg/m^3	LINK 8 uniaxial structural link
Payload	Mass : 2 kg	MASS 21 Structural point mass
Connection between components	None	MPC 184 rigid beam element

The static load results for these two conditions are shown in Table 4 and graphically represented in Figure 3. The darker and lighter shades represent compressive and tensile loading respectively.

Table 4: Static displacement results for the two extreme conditions of the boom angle

	Boom Angle 85°	Boom Angle 20°
Boom tip displacement (m)	1.234×10^{-6}	0.034
Compressive force on boom (N)	28.2	61.7
Tensile force in luff rope (N)	5.5	51.91

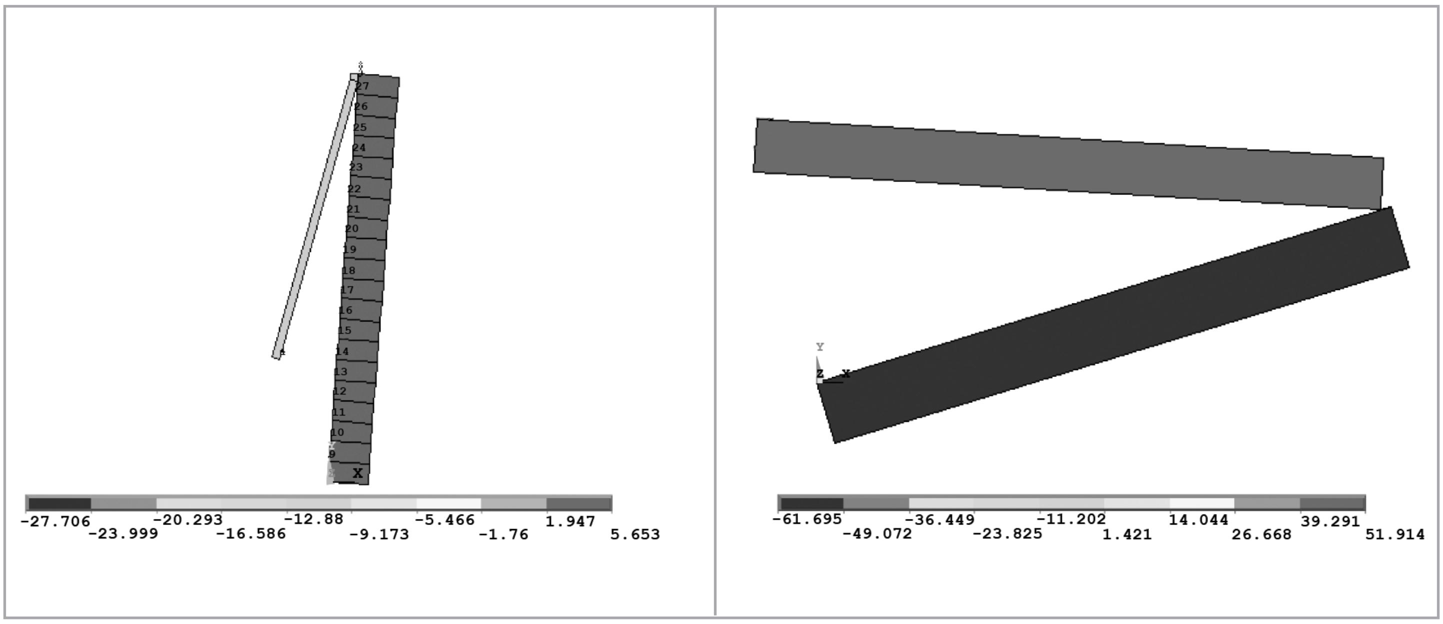

Figure 3: Tensile and compressive force contours of the finite element model for boom angle: (a) 85°, (b) 20°

From the static simulation with the two extreme boom angles, it was found that the boom experiences compression while the luff and hoist ropes undergo tension. The tensile and compressive forces are larger with the boom angle of 20^o. This is due to the larger pulling of the luff rope, which produced a larger compression in the boom. This confirms the analysis by Charrett and Hyden[14] on static loading of boom angle luffing cranes where the lowest boom angle was identified as the maximum loading angle.

The natural frequencies and mode shapes of the scaled-down model were determined using the Block Lanczos mode extraction method [18] that is available in the modal analysis module of the ANSYS finite element analysis software. The analysis was repeated with increasing number of beam elements to obtain a converged solution on the modal parameters. To avoid discretization errors in higher mode shapes, 20 beam elements were used to model the boom and to obtain a converged solution. The elements used for this model are shown in Table 3. The same displacement constraints were applied for this model with the exception of the loading that was omitted and replaced with the mass element. The boom was aligned at 20° for this analysis, which is the same angle used for the experimental verification. The simulation results are shown in Table 9.

4.0 EXPERIMENTAL VERIFICATION OF THE FINITE-ELEMENT MODEL

An experimental rig representing the scaled-down model, as shown in Figure 4, was built and instrumented with strain gauges as shown in Figure 5. The strain gauges were attached to the experimental rig at five different positions, *i.e.*, the base, lower-half, mid-span and upper-half of the boom, and the boom tip. In the static displacement test, a range of test load similar to the loads used in the static simulation using the finite element model was applied at the boom tip. The static strains were measured at all the points where the strain gauges were attached and compared to the simulated results to to check for compatibility between the finite element model and experimental test rig. The boom angle was fixed at 20^o during the experimental work. Experimental values of the strain are compared to those obtained from the finite-element analysis as shown in Tables 5 to 8. Results indicate percentage errors of less than 13% between the measured strains with those computed using ANSYS.

Figure 4: Experimental rig representing scaled-down model of an offshore crane

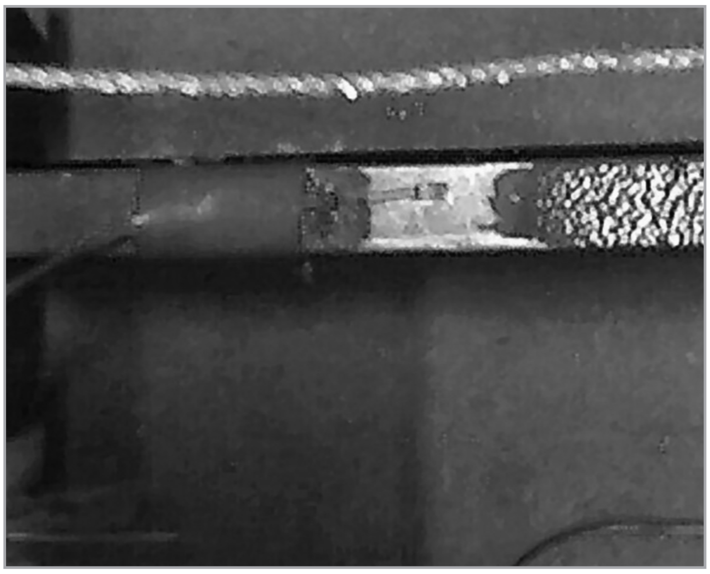

Figure 5: A strain gauge attached to the boom

Table 5: Comparison between the measured and simulated strain with a 10 N payload

	Measured	Simulated	% Error
Base	-4.85E-07	-5.24E-007	7.43
Lower half	-2.75E-06	-3.14E-006	12.52
Mid span	-5.47E-06	-5.76E-006	5.08
Upper half	-8.03E-06	-8.38E-006	4.21
Tip	-9.89E-06	-1.05E-005	5.61

Table 6: Comparison between the measured and simulated strain with a 20 N payload

	Measured	Simulated	% Error
Base	-8.50E-07	-8.98E-007	5.35
Lower half	-4.96E-06	-5.39E-006	7.95
Mid span	-9.59E-06	-9.88E-006	2.92
Upper half	-1.32E-05	-1.44E-005	8.14
Tip	-1.61E-05	-1.80E-005	10.36

Table 7: Comparison between the measured and simulated strain with a 30 N payload

	Measured	Simulated	% Error
Base	-1.40E-06	-1.27E-006	10.04
Lower half	-7.20E-06	-7.63E-006	5.69
Mid span	-1.37E-05	-1.40E-005	2.11
Upper half	-1.92E-05	-2.04E-005	5.68
Tip	-2.35E-05	-2.54E-005	7.65

Table 8: Comparison between the measured and simulated strain with a 40 N payload

	Measured	Simulated	% Error
Base	-1.81E-06	-1.65E-006	9.93
Lower half	-9.45E-06	-9.88E-006	4.34
Mid span	-1.78E-05	-1.81E-005	1.72
Upper half	-2.51E-05	-2.63E-005	4.72
Tip	-3.08E-05	-3.29E-005	6.47

In the verification of the dynamic properties of the scaled-down model computed using finiteelement analysis, modal testing was undertaken on the experimental rig to determine its natural frequencies and mode shapes. The modal extraction methods are well established and their details may be found in Ewins [19]. Twenty-one points corresponding to the nodes in the finite-element model of this rig were identified along the boom. An instrumented hammer, as shown in Figure 6, was used to apply impulsive force on these points and the response of the boom was measured using an accelerometer, as shown in Figure 7. The accelerometer was attached to the tip of the boom since large oscillations were expected there. The output signal from the hammer and accelerometer was fed into a dual channel spectrum analyser to obtain the natural frequencies and mode shapes of the test rig.

The natural frequencies measured for the first three modes are compared with those obtained using finite-element analysis in Table 9. The agreement between the measured and the computed natural frequencies was good with percentage errors less than 3%. The results further indicate that the finite-element computation overestimates the natural frequencies. This is because the finite element model is defined by a finite number of elements and thus it is stiffer than the experimental model. This is evident by the larger natural frequencies obtained from the simulated results. In addition to that, experimental results were affected by friction in the moving components and less than ideal boundary conditions. However the experimental mode shapes also compared relatively well with those computed as shown in Figure 8. The experimental mode shape results could have been improved if more points on the boom were used in the modal test.

Figure 6: Instrumented hammer for the experimental modal analysis

Figure 7: Accelerometer attached to the boom tip to measure dynamic response

Table 9: Comparison between the computed and measured natural frequencies

Mode No.	Finite-Element Analysis (Hz)	Experimental (Hz)	% Error
1	8.5	8.3	2.4
2	16.3	15.9	2.5
3	101.8	98.7	3.0

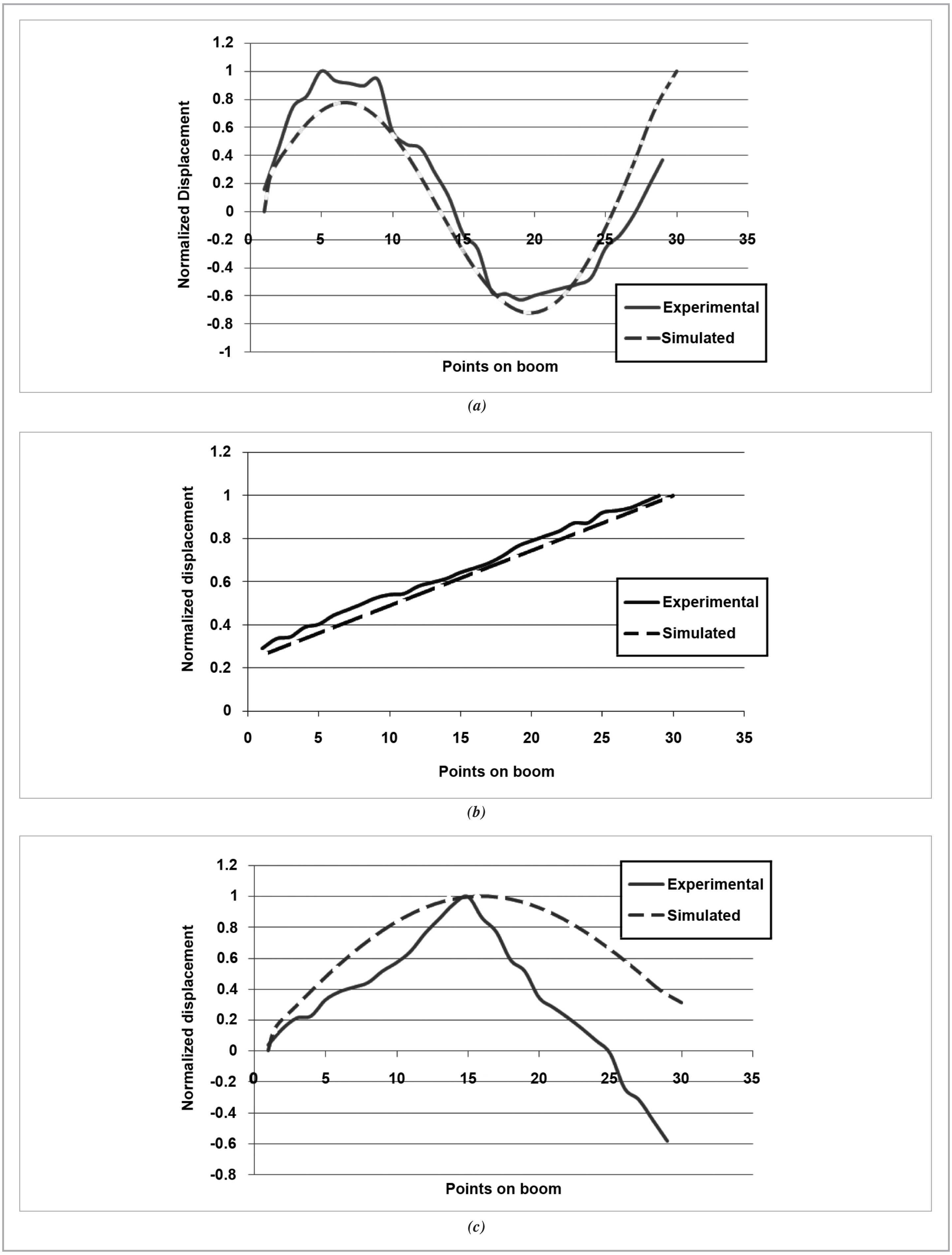

Figure 8: Comparison between the simulated and measured mode shapes: (a) first mode, (b) second mode, (c) third mode

5.0 CONCLUSION

The development of a scaled-down model of a boom angle luffing crane prototype using dimensionless π parameters is presented in this work. The model, which has geometric and dynamic similarities with the prototype, was numerically and experimentally examined for its static and dynamic characteristics. The numerical analysis of the model was undertaken using a commercially available finite-element computer program, ANSYS. This program was utilised to compute the stiffness and stresses in the model subjected to static loads, as well as the natural frequencies and mode shapes, which represent the dynamic characteristics of the model. An experimental rig of the model crane was fabricated, and measurements were performed to verify the computational results obtained from the finite-element analysis. The static strains measured at various positions on the boom were found to be within 14% of those obtained from the finiteelement analysis. The natural frequencies and mode shapes of the model crane obtained using modal testing technique was also found to be in good agreement to those obtained from the finiteelement analysis, with discrepancies within 3% for the first three modes. The numerical and experimental results from the scaled-down model may provide useful insights into the static and dynamic performance of the prototype cranes. They also serve as a less expensive alternative to evaluate the static and dynamic characteristics of prototype cranes, as full scaled testing of these prototypes are rarely undertaken due to the exorbitant cost involved. ■

REFERENCES

[1] J. Verschoof, Crane Design, Practice and Maintenance, Suffolk: Professional Engineering Publishing, 2002.

[2] W. Lacarbonara, R. R. Soper, A. H. Nayfeh and D. Mook, A Non Classical Vibration Absorber for Pendulation Reduction, Journal of Vibration and Control 7 (2001) 365-393.

[3] A. Andreu, L. Gil and P. Roca, A New Deformable Catenary Element for the Analysis of Cable Net Structures, Computers and Structures 84 (2006) 1882 – 1890.

[4] G. Sun, M. Kleeberger and J. Liu, Complete Dynamic Calculation of Lattice Mobile Crane During Hoisting Motion, Mechanism and Machine Theory 40 (2004) 447 – 466.

[5] F. Ju and Y.S. Choo, Super Element Approach to Cable Passing Through Multiple Pulleys, International Journal of Solids and Structures 42 (2004) 3533 – 3547.

[6] F. Ju, Y.S. Choo, Dynamic Analysis of Tower Cranes, Journal of Engineering Mechanics 131 (2005) 88 – 96.

[7] J. J. Wu, M.P. Cartmell and A. R. Whittaker, Prediction of the Vibration Characteristics of a Full Sized Structure from those of a Scaled Model, Computers and Structures 80 (2001) 1461 – 1472.

[8] J. J. Wu, Finite Element Modelling and Experimental Modal Testing of a Three Dimensional Framework, International Journal of Mechanical Sciences 46 (2004)1245 – 1266.

[9] J. J. Wu, Finite Element Analysis and Vibration Testing of a Three – Dimensional Crane Structure, Measurement 39 (2004) 740 – 749.

[10] B. Jerman, P. Podržaj and J. Kramar, An Investigation of Slewing – Crane Dynamics During Slewing Motion – Development and Verification of a Mathematical Model, International Journal of Mechanical Sciences 46 (2004) 729 – 750.

[11] B. Jerman, An Enhanced Mathematical Model for Investigating the Dynamic Loading of a Slewing Crane, Proceedings of the Institution of Mechanical Engineers 220 (2005) 421 – 433.

[12] Y. Al – Sweiti and D. Söffker, Planar Cargo Control of Elastic Ship Cranes with the Maryland Rigging System, Journal of Vibration and Control 13 (2007) 241.

[13] R. J. Henry, Z. N. Masoud, A. H. Nayfeh and D. T. Mook, Cargo Pendulation Reduction on Ship – Mounted Cranes Via Boom – Luff Angle Actuation, Journal of Vibration and Control 7 (2001) 1253.

[14] D. E. Charrett and A. M. Hyden, Dynamic Factors for Offshore Cranes, Proceedings of 8th Annual Offshore Technology Conference, Houston, Dallas, May 3 – 6, 1976.

[15] N. Jones, Structural Impact, Cambridge: Cambridge University Press, 1997.

[16] K. W. Lee and L. C. Gan, Mathematical Modeling and Conceptual Design of a Shock Absorber for Lifting Equipment. Undergraduate Thesis. Monash University, Malaysia, 2005.

[17] Latch and Batchelor Ltd, Wire Rope for Every Application, Latch and Batchelor Ltd, viewed 24th August 2007, http://www.latchandbatchelor.co.uk/rope-info/rope-data/

[18] ANSYS Inc, Release 10 Documentation for ANSYS, Pennsylvania: ANSYS Inc.

[19] D. J. Ewins, Modal Testing: Theory, Practice and Application, 2nd Edition, Hertfordshire: Research Studies Press Ltd, 2000.

PERBANDINGAN JUMLAH KANDUNGAN ELEKTRON DI ATAS VARIASI LONGITUD KHATULISTIWA DAN LATITUD MENGGUNAKAN MODEL IRI, NEQUICK DAN DATA IONEX

(Date received: 27.6.2008)

Mardina Abdullah[1, 2], D.A.A. Mat[3] dan S. S.N. Zulkifli[1]

[1]*Jabatan Kejuruteraan Elektrik, Elektronik dan Sistem, Fakulti Kejuruteraan dan Alam Bina, Universiti Kebangsaan Malaysia, 43600 Bangi, Selangor*

[2]*Felo Bersekutu, Institut Sains Angkasa, Universiti Kebangsaan Malaysia, 43600 Bangi, Selangor*

[3]*Fakulti Kejuruteraan, Universiti Malaysia Sarawak, 94300 Kota Samarahan, Sarawak*

E-mail: [1]mardina@eng.ukm.my

ABSTRACT

Pengetahuan mengenai jumlah kandungan elektron (total electron content, TEC) di sesebuah kawasan terutamanya di kawasan khatulistiwa adalah penting bagi pembangunan sistem komunikasi menggunakan lapisan ionosfera. Kajian ini meliputi perbandingan nilai TEC di sepanjang longitud di khatulistiwa dan latitud dengan mengkaji nilai TEC yang dianggarkan oleh model ionosfera iaitu International Reference Ionosphere (IRI) dan NeQuick. Sebagai perbandingan dan rujukan, data-data TEC harian yang diperolehi daripada Centre for Orbit Determination in Europe (CODE) dalam format IONosphere Map Exchange (IONEX) digunakan. Berdasarkan kajian tersebut, didapati nilai TEC yang dianggarkan oleh model IRI dan NeQuick mengalami sama ada terlebih anggar (overestimation) atau terkurang (underestimation) yang disebabkan oleh pengaruh nombor tompok matahari, R_{12}. Keputusan juga menunjukkan nilai TEC mencapai nilai maksima di sekitar kawasan laut yang disebabkan oleh kekurangan data yang diperolehi dari stesen-stesen penerima. Secara keseluruhannya, TEC yang dikira dari IRI, NeQuick dan IONEX menunjukkan corak yang hampir sama. Kajian yang lebih mendalam boleh dilakukan untuk mengkaji permasalahan yang dialami bagi setiap model dengan menggunakan versi baru IRI dan NeQuick yang mengalami pengubahsuaian pada beberapa bahagian tertentu dan lebih banyak data Khatulistiwa perlu dimasukkan bagi mendapatkan bacaan yang lebih tepat.

Kata Kunci: *Ionosfera, IONEX, IRI, NeQuick. TEC*

COMPARISON OF TOTAL ELECTRON CONTENT OVER EQUATORIAL LONGITUDE AND LATITUDE VARIATIONS USING IRI, NEQUICK MODELS AND IONEX DATA

ABSTRACT

Knowledge regarding total electron content (TEC) in a specific location, particularly at the equator, is necessary for the development of a communications system utilising the ionosphere. This research covers the comparison of TEC values along the equatorial longitude and latitude by analysing estimated TEC values using the International Reference Ionosphere model (IRI) and NeQuick. Daily TEC values obtained from the Centre for Orbit Determination in Europe (CODE) in Ionosphere Map Exchange format (IONEX) are used for comparison and reference purposes. Based on this research, it is found that TEC values estimated by the IRI model and NeQuick experience either overestimation or underestimation, caused by the number of sunspots present, R_{12}. Results also show that TEC values are at their maximum over larger bodies of water, due to the lack of data obtained from the receiving stations. Overall, the TEC calculated by IRI, NeQuick and IONEX show similar patterns. More thorough research can be done to study the problems encountered for each model by using newer versions of IRI and NeQuick that have been modified in several key areas. More equatorial data should also be input to obtain more accurate readings.

Keywords: *Ionosphere, IONEX, IRI, NeQuick, TEC*

1.0 INTRODUCTION

Ionosfera merupakan satu kawasan di atmosfera bumi yang memiliki zarah-zarah bercas dengan ketinggian sekitar 50 km hingga 2000 km dari aras laut [1]. Secara amnya, lapisan ionosfera terdiri daripada beberapa lapisan yang mempunyai perbezaan dari segi kandungan molekul-molekul, ketinggian dari aras laut dan ketumpatan elektron yang bergantung kepada keadaan siang dan malam. Hanya sebilangan daripada molekul-molekul atom yang terkandung dalam lapisan ini merupakan molekul-molekul yang berion, manakala selebihnya merupakan molekul-molekul neutral. Namun, para penganalisis lebih memberikan tumpuan kepada kawasan ionosfera yang kurang daripada 1000 km yang memainkan peranan penting dalam sistem komunikasi radio khususnya pada frekuensi tinggi (*High Frequency*, HF) sejak beberapa dekad yang lalu.

Kajian mengenai lapisan ionosfera bumi seringkali dikaitkan dengan TEC memandangkan anggaran nilai TEC sangat diperlukan bagi membolehkan pembetulan dilakukan pada sistem pencarian lokasi satelit [2]. TEC boleh ditakrifkan sebagai bilangan elektron di dalam suatu ruang yang berpusat di atas laluan isyarat dengan keluasan 1 meter persegi. TEC dikira dalam unitnya tersendiri dan satu unit TEC (TECU) mewakili 10^{16} elektron per meter persegi:

$$1 \text{ TECU} = 1\text{x}10^{16} \text{ el.m}^{-2} \quad (1)$$

Penghasilan model-model ionosfera telah membantu para penyelidik untuk mengkaji nilai TEC ini terutama semasa keadaan geomagnet tenang. Model yang mula-mula diperkenalkan ialah *International Reference Ionosphere* (IRI) yang banyak mengalami perubahan sehingga kini. IRI merupakan projek kerjasama antara *Committee on Space Research* (COSPAR) dan *International Union of Radio Science* (URSI) yang mempunyai objektif dalam menghasilkan satu model piawai untuk mengkaji lapisan ionosfera secara terperinci. Model ini memberikan nilai median dan purata ketumpatan dan kandungan elektron, komposisi ion dan suhu berdasarkan ketinggian, tempat, waktu tempatan dan nombor tompok matahari, R_{12} pada keadaan aman di ionosfera. Dengan usaha yang berterusan, terbitan pertama IRI telah merangkumi liputan global ketumpatan elektron [3].

Satu lagi model yang menggunakan parameter *ionosonde* telah dihasilkan berdasarkan pembaikan ke atas profil bahagian bawah (*bottomside*) ionosfera yang dilakukan oleh Dio Givanni dan Radicella (DGR). *Quick-run model* ini yang dikenali sebagai model NeQuick telah dibangunkan di makmal *Aeronomy and Radiopropagation Laboratory-International Centre for Theoretical Physics* (ARPL-ICTP) dan *IGAM-University of Graz* (Austria). NeQuick memberikan profil ketumpatan elektron menegak dan condong. Model ini yang telah diuji di sekitar kawasan latitud pertengahan dan kawasan kutub di Hemisfera Utara dari altitud 500 km hingga 1000 km telah memberikan nilai TEC yang lebih tepat berbanding data eksperimen yang diperolehi melalui satelit Intercosmos-19 [4].

Selain menggunakan model teori, nilai TEC juga boleh didapati dengan menggunakan Peta Ionosfera Global (*Global Ionosphere Maps*, GIMS). GIMS telah dihasilkan dengan mengumpulkan data-data dalam format *IONosphere map Exchange* (IONEX) daripada kira-kira 150 stesen *International GNSS Service* (IGS) dan institusi-institusi yang berkaitan di *Centre for Orbit Determination in Europe* (CODE), *University of Berne* di Switzerland [5]. TEC global ini dihasilkan secara harian dengan nilai TEC dicerap daripada stesen-stesen IGS. Walaubagaimanapun, di Malaysia tidak terdapat stesen IGS yang dinyatakan tersebut.

Kajian ini bertujuan untuk mengenalpasti variasi TEC di kawasan ionosfera khatulistiwa pada kedudukan longitud yang berbeza. Di samping itu, variasi TEC pada latitud yang berbeza juga dikaji. Perbandingan nilai-nilai TEC dilakukan dengan menggunakan model-model ionosfera dan data IONEX yang didapati daripada data nyata GPS sebagai rujukan.

2.0 KAEDAH KAJIAN

Penganalisaan data-data TEC yang diperoleh dilakukan dalam dua bahagian berdasarkan Rajah 1.

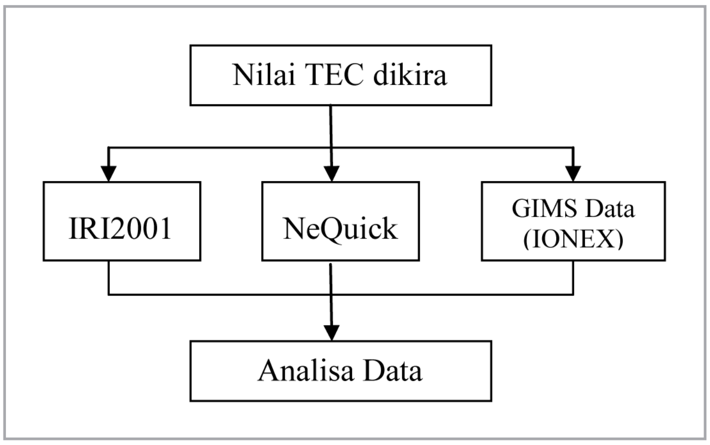

Rajah 1 : Kaedah analisa nilai bacaan TEC daripada model IRI2001, NeQuick dan IONEX

Nilai TEC yang diperoleh melalui model-model IRI2001 dan NeQuick dibandingkan dengan data IONEX yang diperolehi. Nilai TEC dari data nyata IONEX diambil dengan menginterpolasi sebahagian daripada data tersebut. Ini adalah kerana data yang diperlukan pada kedudukan yang dikehendaki adakalanya tidak terdapat dalam data IONEX tersebut. Perbandingan dibuat dengan merujuk kepada faktor-faktor kedudukan longitud dan latitud bumi. Analisa data dihasilkan dengan berpandukan permasalahan yang dihadapi dan ralat yang dianggarkan oleh setiap model mahupun IONEX. Ini dilakukan dengan menggunakan perisian Microsoft Excel untuk mengira nilai ralat TEC yang dianggarkan oleh setiap model. Malah sebuah program yang dihasilkan melalui perisian Matlab telah dihasilkan untuk mengira data interpolasi bagi menentukan bacaan TEC pada kedudukan yang dikaji. Sebagai contoh, untuk menganggarkan data TEC pada kedudukan latitud X, data TEC pada latitud yang berhampiran dengan latitud X iaitu pada latitud X_1 dan X_2 diinterpolasikan dengan menggunakan persamaan (2).

$$\frac{X - X_1}{X_2 - X_1}(\text{TEC pada } X_2 - \text{TEC pada } X_1) + \text{TEC pada } X_1 \quad (2)$$

Selain itu juga, penentuan penggunaan parameter merupakan faktor penting dalam kajian ini khasnya melalui model IRI2001 yang mana setiap parameter bahagian atas (*topside*) (800 km ke atas) dan bahagian bawah (300 km ke bawah) ionosfera boleh diubah mengikut kesesuaian pengguna [6]. Walaubagaimanapun, hanya parameter bahagian bawah yang menjadi tumpuan dan mengalami perbezaan. Kawasan di bahagian bawah puncak lapisan F2 atau dikenali sebagai *bottomside F region*, dihasilkan berdasarkan berdasarkan persamaan (3).

$$N(h) / NmF2 = \exp(-x^{B1}) / \cosh(x) \quad (3)$$

Dimana *NmF2* ialah ketumpatan elektron maksimum bagi puncak lapisan F2, dengan $x = (hmF2 - h)/B0$. *hmF2* ialah ketinggian puncak bagi lapisan F2 dan parameter B0 diperolehi dari pengukuran empirik bahagian bawah lapisan ionosfera iaitu daripada pengukuran ionosonde dari pelbagai ionosonde yang terlalu banyak bilangannya di seluruh negara lain di dunia. Walaubagaimanapun data ini tidak terdapat di Malaysia. B0 ialah parameter ketebalan bahagian bawah yang memberikan perbezaan antara ketinggian di antara lapisan puncak F2, *hmF2* dengan nilai profil ketumpatan elektron yang jatuh pada nilai 0.24*$NmF2(x=1)$, serta pada titik anchor, (*hmF2*/*NmF2*) dan (*hmF2*-B0/0.24**NmF2*). Senarai B0 yang digunakan dalam model IRI telah ada dalam model itu sendiri. Manakala parameter *B*1 menjelaskan bentuk profil di antara titik-titik ini. Nilai *B*1 yang tinggi memberi maksud bahawa kawasan tersebut mengandungi nilai kandungan elektron yang tumpat. Pada semua keadaan, model IRI menghadkan nilai *B*1=3. Parameter bahagian atas bagi model IRI2001 hanya menggunakan model yang disediakan dalam program tersebut. Dalam kajian ini juga, pungutan data TEC yang diperolehi melalui model IRI2001 adalah berdasarkan penggunaan parameter URSI kerana bacaan yang diperolehi adalah lebih baik berbanding dengan penggunaan parameter *International Radio Consultative Committee* (CCIR) berdasarkan kajian yang telah dibuat oleh Zhang *et al*. [7].

Namun bagi model NeQuick, parameter-parameter bahagian bawah dan bahagian atas yang digunakan dalam kajian ini berdasarkan kepada model itu sendiri yang tidak boleh diubah seperti mana model IRI2001. Selain itu juga, perisian *Satellite Pointer Controller* yang telah dihasilkan oleh Ling dan Masri [8] telah digunakan (dengan izin) untuk mengesan lokasi kawasan kajian pada peta dunia.

3.0 HASIL DAN PERBINCANGAN

Bagi mendapatkan perbandingan variasi TEC daripada model-model dan IONEX, bacaan dikira pada masa-masa tertentu di sekitar garisan geografi Khatulistiwa dengan nilai R_{12} yang berbeza-beza. Kajian ini terbahagi kepada dua bahagian yang mana bahagian pertama dijalankan bagi membandingkan nilai bacaan TEC pada kawasan sekitar longitud bumi manakala bahagian kedua bagi mendapatkan perbandingan nilai bacaan TEC pada kawasan sekitar latitud bumi.

3.1 Perbandingan nilai bacaan TEC pada longitud bumi - Khatulistiwa

Bagi mengelakkan kesan nombor tompok matahari, R_{12} (*Sun Spot Number, SSN*) mempengaruhi nilai TEC yang diperolehi melalui model-model ionosfera, bacaan TEC pada tarikh 23 Julai 2006 telah diplotkan dengan nilai $R_{12} = 0$ iaitu yang berdasarkan kepada data IONEX. Pengaruh SSN ke atas bacaan TEC perlu dielakkan kerana nilai SSN yang tinggi akan menyebabkan anggaran berlebihan (*overestimation*) dan berkurangan (*underestimation*) yang ketara pada bacaan TEC pada kedua-dua model. Hal ini telah dijelaskan dalam kajian yang dilakukan oleh Trísková dan Chum [9]. Rajah 2 dan 3 menunjukkan lokasi kawasan kajian dan kedudukan stesen-stesen penerima di bumi yang digunakan untuk data IONEX. Seperti yang dapat dilihat dalam Rajah 2, kajian dijalankan di sepanjang longitud 45ºB ke 45ºT dengan latitud 0 darjah Utara (kawasan Khatulistiwa) yang terdiri daripada kawasan lautan dan daratan bagi mendapatkan perbezaan nilai bacaan TEC antara kedua-dua bahagian bumi ini secara tidak langsung. Selain itu, kawasan kajian ini juga dipilih supaya kajian mengenai kesan keberadaan/kewujudan stesen-stesen penerima kepada nilai-nilai TEC yang diperolehi dapat dijalankan. Seperti yang kelihatan dalam Rajah 3, terdapat 8 buah stesen IGS yang berdekatan di sekitar kawasan kajian tersebut. Kajian dijalankan dengan perbezaan masa waktu tempatan (*local time*, LT) di kawasan kajian ialah ±3-LT bagi mengelakkan kesan radiasi matahari pada bacaan TEC.

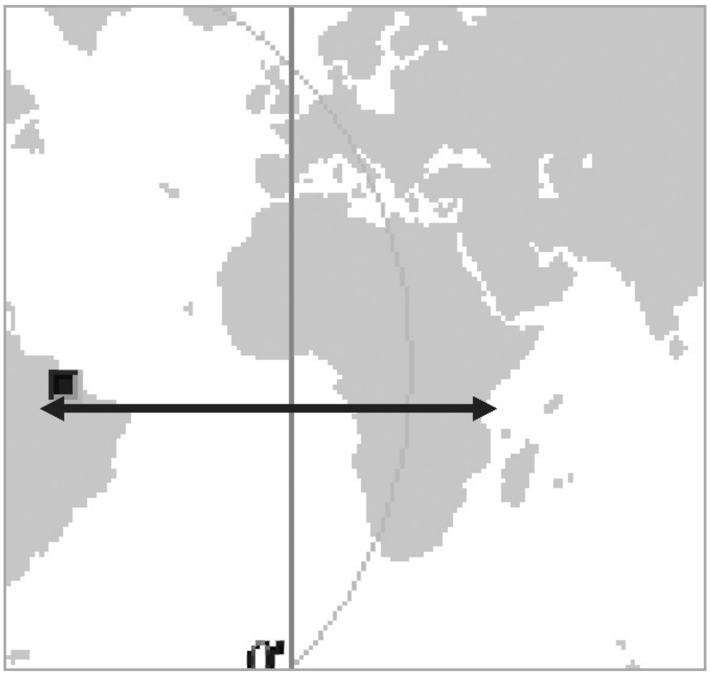

Rajah 2 : Kedudukan kawasan kajian pada peta dunia [8]

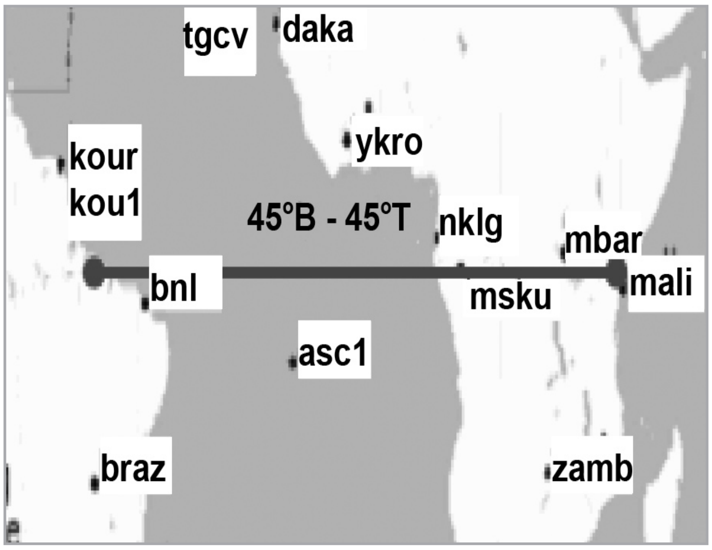

Rajah 3 : Kedudukan stesen-stesen IGS di sekitar kawasan kajian [10]

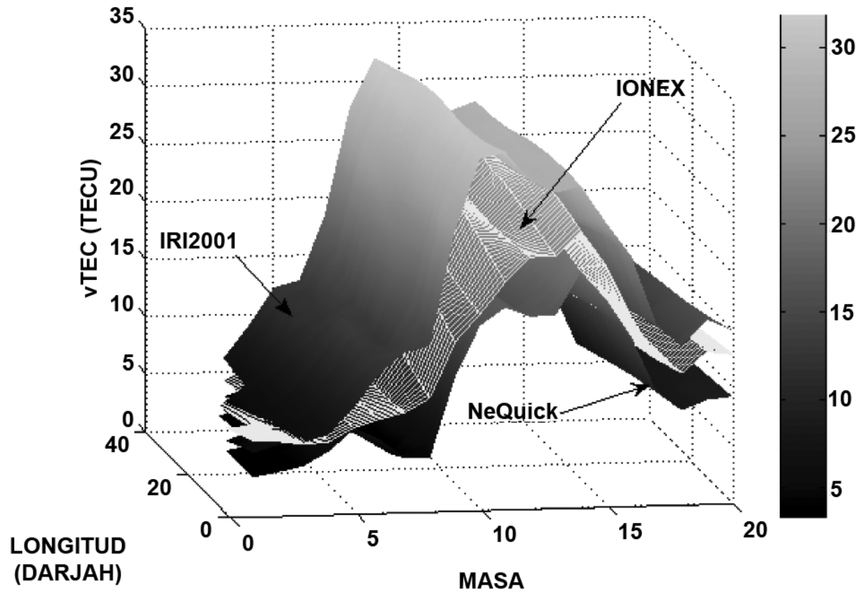

Rajah 4 : Nilai-nilai TEC yang diberikan oleh model-model IRI2001, NeQuick dan IONEX

Pengiraan TEC di sekitar kawasan kajian telah dilakukan dengan menggunakan model-model IRI2001, NeQuick serta data IONEX dan hasilnya telah diplotkan bersama dalam 3 dimensi seperti dalam Rajah 4. Perbandingan data-data TEC yang dicerap menunjukkan bahawa nilai TEC IONEX berada di antara nilai TEC yang dianggarkan oleh kedua-dua model IRI2001 dan NeQuick. Perolehan data-data TEC pada Rajah 4 diplotkan semula dalam Rajah 5 dengan menggunakan hasil interpolasi data TEC pada 3-LT di kawasan kajian.

Berdasarkan data IONEX yang diperolehi, nilai TEC yang diberikan pada kedudukan 45ºB hingga 15ºB adalah hampir sekata dengan nilai TEC di antara 7.10 TECU dan 7.40 TECU. Seperti yang dapat dilihat dalam Rajah 2, kawasan ini merupakan kawasan lautan yang mana bacaan TEC di sekitar kawasan ini tidak dipengaruhi oleh stesen-stesen penerima yang pada kebiasaannya terletak di kawasan daratan. Berdasarkan kajian yang telah dijalankan oleh Zhao *et al.* [11], ketepatan bacaan IONEX yang diberikan di sekitar kawasan lautan adalah sekitar 1-2 rms dengan data yang diberikan adalah stabil melalui penggunaan altimeter radar khusus untuk mengenalpasti perubahan paras laut.

Pada kedudukan 0º hingga 45ºT, nilai TEC daripada

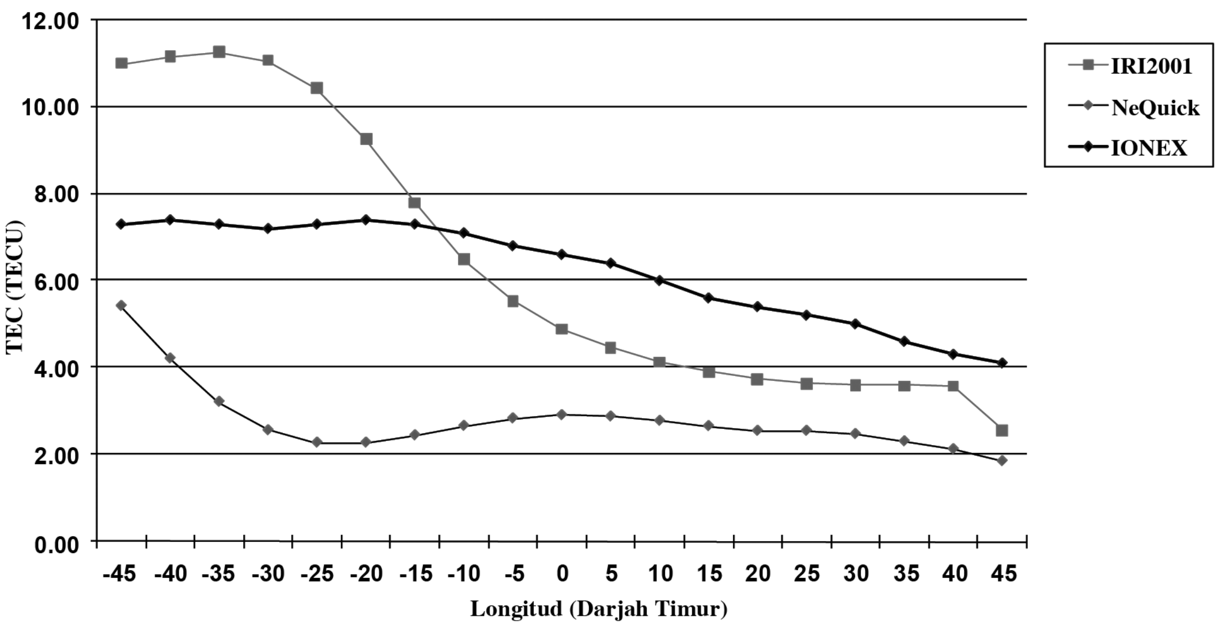

Rajah 5 : Perbandingan nilai TEC oleh model-model IRI2001, NeQuick dan IONEX

IONEX mengalami penurunan yang ketara. Perubahan ini adalah disebabkan oleh data-data daripada pelbagai stesen penerima in situ pada permukaan bumi yang menyebabkan berlakunya gangguan major pada nilai bacaan TEC [12]. Hal sebegini jarang berlaku di sekitar longitud bumi dan kawasan yang terletak pada permukaan lautan kerana kurangnya bilangan stesen-stesan penerima. Perbezaan yang terdapat dalam sistem pemodelan dan pengiraan nilai TEC bagi setiap stesen IGS yang berbeza juga menyebabkan berlakunya ralat dan ketidaktepatan pada bacaan TEC yang diberikan oleh CODE ini [13].

Bagi model IRI2001, bacaan TEC di sekitar garisan 45ºB hingga 0º menunjukkan nilai yang tinggi berbanding dengan IONEX dengan nilai maksimum TEC dicerap pada kedudukan 35ºB iaitu 11.26 TECU. Hal ini disebabkan oleh kekurangan data yang dihasilkan oleh satelit, *incoherent scatter radar* dan pengiraan roket [14]. Stesen bumi yang menyediakan data kepada IRI menghadapi masalah terutama semasa menganggarkan bacaan kandungan elektron pada lapisan atas ionosfera kerana wujudnya plasma-plasma yang memiliki frekuensi yang tinggi untuk ditembusi oleh peralatan *in situ*. Oleh sebab itu, berlaku anggaran berlebihan pada nilai TEC yang diberikan oleh IRI semasa menganggarkan kandungan ketumpatan elektron pada bahagian atas ionosfera tersebut. Pada kedudukan 0º hingga 45ºT pula, bacaan TEC yang diberikan oleh model IRI2001 mengalami penganggaran yang kurang bermula pada kedudukan -15ºT hingga 45ºT.

Bagi model NeQuick pula, keseluruhan nilai TEC yang diberikan adalah kurang berbanding IONEX dan IRI2001 dengan nilai maksimum anggaran berlaku pada kedudukan 45ºB iaitu 3.22 TECU. Walau bagaimanapun, nilai TEC yang dianggarkan menunjukkan bacaan TEC yang lebih sekata berbanding dengan IRI2001 dan IONEX. Untuk mengelakkan berlakunya ralat kepada bacaan TEC khasnya dengan penggunaan model NeQuick ini, waktu ±3- LT dipilih pada kawasan kajian. Walaubagaimanapun, perisian NeQuick ini telah dikaji semula [15]. Ini kerana terdapat kekeliruan pada model John Titheridge dengan peta klasik CCIR terutamanya pada waktu siang dan pertukaran antara siang dan malam yang berkaitan dengan parameter frekuensi kritikal pada waktu tersebut. Oleh yang demikian, pemilihan waktu kajian adalah bersesuaian bagi model NeQuick ini.

NeQuick menghasilkan nilai anggaran TEC berdasarkan data-data daripada rangkaian *ionosonde* dan diringkaskan ke dalam formula matematik yang dikenali sebagai *semi epstein layer*. Walaupun kelebihan lapisan ini ialah ia tidak dipengaruhi oleh nilai ketinggian ionosfera, namun ralat berlaku disebabkan oleh siri Fourier yang digunakan dalam peta CCIR bagi model NeQuick ini. Berdasarkan teknik pemetaan yang dihasilkan oleh Jones dan Gallet, yang dinyatakan dalam Rush [16], setiap data yang diperolehi akan ditukarkan dalam bentuk siri masa Fourier dan seterusnya diwakilkan dengan setiap pekali Fourier. Namun begitu jumlah pekali ini adalah terhad. Menurut Rush, peta CCIR terhad kepada kawasan terutamanya pada kawasan lautan dan selatan hemisfera kerana terdapatnya kekurangan alat ukur *ionosonde*. Disebabkan oleh permasalahan ini, nilai TEC yang dianggarkan oleh NeQuick mengalami ralat yang besar berbanding dengan IONEX dan IRI2001.

Jadual 1 : Perbezaan nilai TEC (TECU) pada longitud bumi

	Nilai Purata	Nilai Minimum	Nilai Maksimum
IONEX	6.23	4.10	7.40
IRI2001	6.42	2.56	11.26
NeQuick	2.79	1.86	5.42

Perbezaan bagi ketiga-tiga sumber TEC ini dijelaskan dalam Jadual 1. Daripada jadual ini didapati nilai purata bagi keseluruhan data TEC yang dianggarkan oleh setiap model dan IONEX adalah berbeza. Walau bagaimanapun, terdapat perkaitan yang hampir pada anggaran TEC yang diberikan oleh model IRI2001 dan IONEX, dengan nilai purata yang berdekatan iaitu 6.23 TECU (IONEX) dan 6.42 TECU (IRI2001) berbanding dengan 2.79 TECU (NeQuick). Selain itu juga, nilai minimum dan maksimum bagi TEC yang dianggarkan masing-masing menunjukkan perbezaan yang ketara. Ini kerana nilai maksimum model IRI2001, 11.26 TECU, merupakan nilai TEC yang tertinggi dibandingkan dengan IONEX dan NeQuick. Walau bagaimanapun, nilai minimum TEC yang dianggarkan oleh model NeQuick memberikan nilai yang terendah iaitu 1.86 TECU. Terdapat persamaan antara IRI2001, IONEX dan NeQuick di mana nilai maksimum TEC yang dicerap adalah pada kawasan lautan manakala nilai minimum TEC dicerap pada kawasan daratan. Ini jelas menunjukkan bahawa kesan kedudukan stesen-stesen penerima di bumi menyebabkan berlakunya ralat pada bacaan TEC terutamanya bagi model-model. Walaupun model IRI2001 juga memperolehi data daripada *topside sounder*, tetapi masalah berlaku kerana bacaan yang diperoleh ini hanya terhad kepada tempat-tempat tertentu sahaja dan data hanya boleh diambil pada dua atau tiga hari sahaja dalam jangka masa satu bulan [17]. Penghasilan *topside sounder* ini bertujuan untuk merekodkan amplitud dan tundaan masa hingar (*echo delay times*) pada hingar yang terdapat dalam lapisan ionosfera melalui penggunaan *topside sounder Aloutte*/ISIS dengan frekuensi di antara 0.1 hingga 20 MHz. Selain itu, penggunaan parameter B0 bagi data *ionosonde* yang digunakan oleh model ini menyebabkan nilai bacaan TEC yang diberikan tidak dapat menganggarkan ketepatan nilai di bahagian atas ionosfera [7].

Penggunaan peta klasik CCIR juga menyebabkan ralat pada bacaan TEC bagi model NeQuick. Disebabkan terdapat kekurangan rangkaian *ionosonde* di dunia, data yang diperoleh untuk menghasilkan peta CCIR ini agak terhad berbanding dengan penggunaan model pekali URSI yang digunakan oleh model IRI2001 dalam kajian ini. Walaupun kaedah pemetaan yang digunakan adalah sama dengan peta CCIR namun terdapat pengubahsuaian yang dilakukan melalui pengadaptasian teori aerodinamik kepada setiap ruang kosong antara data-data yang diperoleh daripada ionosonde sebelum pemetaan secara harmonik dilakukan [17; 18]. Malahan melalui model URSI ini, data yang diperolehi adalah dari kira-kira 180 stesen seluruh dunia (data bulanan sebanyak 45 000) berbanding CCIR yang hanya daripada 150 stesen dengan kira-kira 10 000 data bulanan sekitar tahun 1954 dan 1958 [20].

3.2 Perbandingan nilai bacaan TEC pada latitud bumi

Kajian turut dijalankan bagi mengenalpasti pengaruh kedudukan latitud bumi kepada nilai TEC yang dianggarkan bagi setiap model dan IONEX dan faktor-faktor yang mempengaruhi perbezaan nilai TEC tersebut. Pemilihan lokasi kawasan kajian adalah berdasarkan jumlah stesen IGS di kawasan tersebut dan mestilah berada pada bahagian daratan bumi. Ini adalah berdasarkan kajian yang dijalankan di sekitar longitud bumi, yang mendapati bahawa ralat daripada data IONEX dan model-model adalah disebabkan kekurangan stesen-stesen IGS. Kedudukan kawasan kajian yang dipilih dan lokasi stesen-stesen penerima IGS dapat dilihat pada Rajah 6 dan 7.

Rajah 6 : Kawasan kajian pada kedudukan 20ºT, 75ºU-35ºS [8]

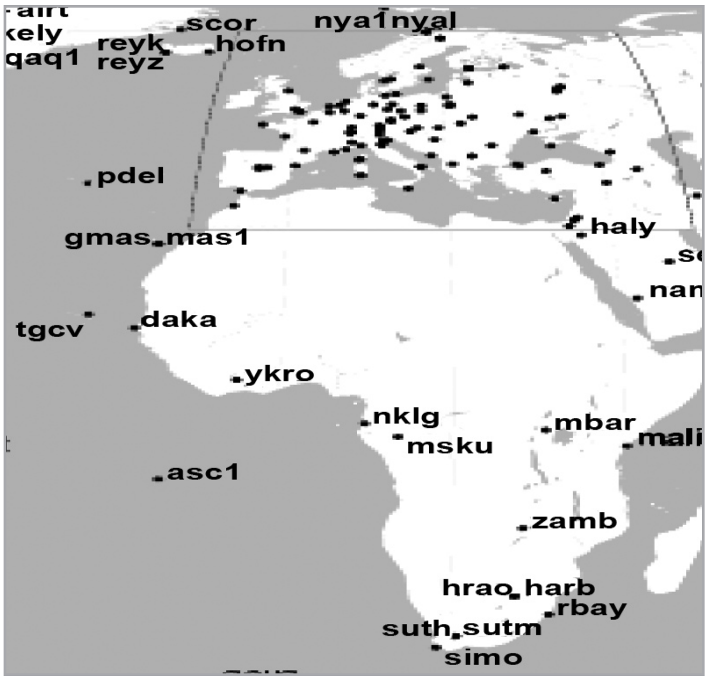

Rajah 7 : Lokasi stesen-stesen IGS di kawasan kajian [10]

Kajian telah dijalankan sewaktu berlakunya ekuinoks pada 8 Mac 2005 di kedudukan longitud 20ºT dan latitud dari 75ºU ke 35ºS dengan nilai R_{12} pada hari tersebut ialah 33. Tujuan utama kajian ini dijalankan pada musim ekuinoks adalah bagi mengelakkan kesan angin neutral yang bertiup dari Hemisfera Utara atau Hemisfera Selatan menuju ke garisan Khatulistiwa bumi atau ke bahagian Kutub Bumi [21]. Ini kerana kesan angin neutral hanya berlaku pada musim panas dengan tiupan angin yang menuju ke khatulistiwa (*equatorward*) dan menuju ke kutub (*poleward*). Selain itu, kesan tiupan angin neutral ini akan menyebabkan berlakunya bacaan TEC yang tidak simetri antara Hemisfera Utara dan Hemisfera Selatan bumi yang merujuk

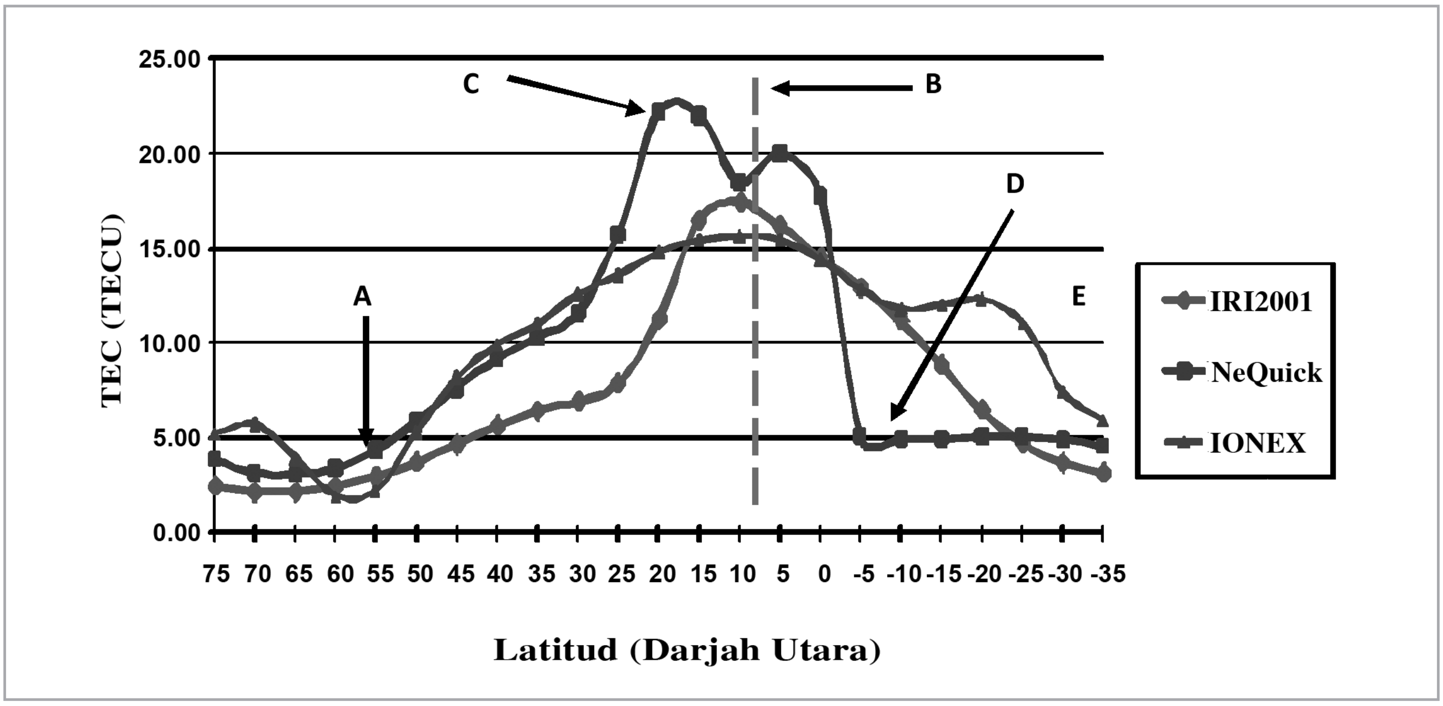

Rajah 8 : Nilai bacaan TEC pada kedudukan latitud bumi kepada garis geomagnet [21]. Tiupan angin neutral ini akan mempengaruhi elektron-elektron bertenaga tinggi di kawasan sekitar garisan Khatulistiwa yang terhasil semasa berlakunya kejadian Anomali Khatulistiwa melalui proses pertembungan medan magnet dan medan elektrik bumi. Fenomena ini akan menyebabkan elektron-elektron tersebut bergerak ke kawasan yang mempunyai daya tarikan yang kuat terutamanya pada waktu siang dan lewat petang yang mempunyai nilai R_{12} yang tinggi.

Dengan menggunakan data daripada model-model dan IONEX, nilai-nilai TEC dikira dengan menggunakan data pada 1-LT di kawasan kajian iaitu waktu awal pagi. Waktu ini dipilih bagi mengelakkan sinaran radiasi matahari yang kuat terutamanya pada waktu tengahari dan petang yang akan menyebabkan ralat pada nilai TEC yang dianggarkan oleh setiap model. Jika tidak, nilai TEC yang dianggarkan model IRI2001 akan mengalami ralat yang besar disebabkan oleh penggunaan parameter B0 dan pekali bagi model ini [7]. Bagi model NeQuick, penggunaan pekali CCIR juga akan menyebabkan ralat bacaan TEC khasnya pada waktu siang [16]. Rajah 8 menunjukkan hasil analisis dari setiap model dan data IONEX.

Seperti yang dapat dilihat dalam Rajah 8, kawasan A dengan latitud di antara 50ºU dan 65ºU, bacaan TEC yang dianggarkan oleh model-model IRI2001, NeQuick dan IONEX memberikan nilai yang hampir serupa iaitu dengan perbezaan nilai TEC ±2 TECU. Ini kerana jumlah stesen-stesen penerima di kawasan tersebut adalah lebih banyak berbanding kawasan yang lain. Kawasan ini adalah kawasan latitud tengah yang terdiri dari negara-negara di Eropah. Bacaan TEC yang diberikan oleh IONEX secara puratanya menghampiri nilai TEC yang dianggarkan oleh model-model, walaupun masih terdapat ralat kerana data-data TEC yang dihasilkan oleh setiap stesen-stesen tersebut adalah berbeza terutamanya dari segi penggunaan teknik pengiraan TEC yang berlainan.

Ini merupakan kelebihan kepada model IRI2001 kerana dengan data yang diperoleh daripada banyak stesen-stesen ini, ralat yang diberikan adalah berkurangan berbanding sebaliknya. Namun penggunaan parameter B0 bagi peralatan *in situ* telah menyebabkan berlakunya perbezaan bacaan TEC yang dianggarkan oleh model ini berbanding NeQuick dan IONEX. Ini kerana parameter ini terhad kepada lapisan bawah ionosfera bumi sahaja. Kawasan atas ionosfera yang memiliki zarah-zarah yang berfrekuensi tinggi tidak dapat ditembusi oleh parameter ini.

Bagi model NeQuick, ketepatan nilai TEC yang dianggarkan juga sekitar ±2 TECU berbanding dengan IONEX. Hasil data-data yang diperolehi daripada *ionosonde* yang diadaptasikan dengan penggunaan formula matematik menyebabkan model ini tidak mengalami permasalahan seperti yang dialami oleh model IRI2001. Namun, ralat TEC berlaku disebabkan oleh penggunaan formula matematik yang terlalu ringkas pada profil bahagian atasnya seperti yang dinyatakan juga oleh Cander *et al*. [15].

Kajian ini telah dilakukan pada musim ekuinoks, oleh itu kesan angin neutral sepatutnya tidak berlaku kepada bacaan TEC yang dianggarkan bagi setiap model dan IONEX. Namun seperti yang dilihat pada titik *B*, garis simetri telah dilukis untuk menunjukkan bahawa nilai TEC yang diberikan oleh data IONEX hampir sama pada kawasan Hemisfera Utara dan Selatan bumi dan nilai maksima TEC diperolehi sekitar garisan khatulistiwa. Garisan simetri ini merujuk kepada garis geomagnet khatulistiwa yang bernilai 0º pada garisan geografi khatulistiwa 10ºU. Ini juga ditunjukkan oleh nilai TEC yang dianggarkan oleh kedua-dua model. Walau bagaimanapun masih terdapat kekeliruan pada nilai TEC yang dianggarkan oleh model-model dengan merujuk garis *B* ini.

Bagi model IRI2001 pula, nilai TEC yang dianggarkan berbeza dan tidak simetri seperti yang ditunjukkan pada titik *C*. Nilai TEC pada kawasan Hemisfera Utara adalah lebih tinggi berbanding dengan Hemisfera Selatan bumi. Ini membuktikan kewujudan kesan angin neutral yang bertiup menuju ke arah garisan Khatulistiwa dengan nilai TEC pada kawasan ini adalah tinggi berbanding sebaliknya. Nilai TEC yang tidak simetri juga berlaku bagi model NeQuick dengan nilai TEC yang banyak pada kawasan Hemisfera Utara berbanding sebaliknya. Bacaan TEC NeQuick juga menunjukkan kewujudan angin neutral yang menyebabkan elektron-elektron berada pada kawasan yang mempunyai daya tarikan yang kuat.

Pada titik *D*, berlaku perubahan yang ketara pada nilai TEC yang diberikan oleh model NeQuick berbanding IONEX dan IRI2001. Model NeQuick menganggarkan nilai TEC yang paling rendah diikuti oleh IONEX dan IRI2001. Penurunan nilai TEC yang ketara pada kedudukan 5ºS hingga 35ºS menunjukkan bahawa model NeQuick hanya bersesuaian digunakan pada bahagian Hemisfera Utara berbanding Hemisfera Selatan bumi yang mana kebanyakan data-data hanya diperoleh dari kawasan tersebut. Pada titik *E*, ralat yang diberikan oleh model-model dan IONEX adalah sekitar ±3 TECU berbanding satu sama lain.

Nilai maksimum dan minimum TEC yang diperolehi melalui kajian ini telah diringkaskan pada Jadual 2.

Jadual 2 : Perbezaan nilai TEC (TECU) pada latitud

	Nilai Purata	Nilai Minimum	Nilai Maksimum
IONEX	9.93	1.90	15.60
IRI2001	7.55	2.16	17.37
NeQuick	9.25	3.17	22.14

Nilai purata bagi model NeQuick menghampiri nilai purata IONEX berbanding dengan IRI2001 seperti yang dilihat pada Jadual 2. Ini menyatakan bahawa model NeQuick dari segi purata yang menggunakan formula matematik dalam penganggaran nilai TEC memberikan ketepatan yang hampir serupa dengan IONEX bagi kajian di Hemisfera Utara dan Hemisfera Selatan. Nilai TEC maksimum telah diperoleh di kawasan sekitar garisan khatulistiwa manakala nilai minimum TEC diperolehi di kawasan jauh daripada kawasan khatulistiwa. Ini menunjukkan bahawa walaupun pengaruh angin neutral kepada kelajuan dan arah pergerakan zarah-zarah elektron dapat dielakkan dengan pemilihan musim ekuinoks, namun kesan anomali tidak dapat dielakkan pada pengiraan di sekitar garisan Khatulistiwa bumi ini. Ini kerana pada musim ini, matahari berada pada kedudukan 0º daripada garisan geografi Khatulistiwa dan kadar pengionan berlaku dengan kadar yang cepat. Ini dapat dilihat dengan jelas dari model NeQuick yang kelihatan seperti bongkah menunjukkan kewujudan anomali khatulistiwa.

Daripada analisis ini, dapat disimpulkan bahawa faktor lokasi kedudukan stesen-stesen bumi memberikan perbezaan bacaan TEC yang ketara bagi setiap model dan IONEX disebabkan oleh sumber utama data yang digunakan khasnya dalam permodelan IRI2001 ialah berdasarkan data *in situ* dan *ionosonde*. Selain itu, jumlah stesen-stesen penerima yang banyak di bahagian Hemisfera Utara berbanding dengan Hemisfera Selatan juga menyebabkan data yang dianggarkan oleh IRI2001 menunjukkan nilai TEC yang tinggi dan menghampiri nilai TEC IONEX pada kawasan tersebut berbanding sebaliknya. Faktor ini kurang mempengaruhi nilai anggaran yang diberikan oleh model NeQuick kerana pengiraan TEC yang dibuat adalah berdasarkan penggunaan formula matematik yang telah sedia ada dalam permodelannya.

Selain itu juga, kesan angin neutral menyebabkan tumpuan kawasan elektron berubah-ubah mengikut keadaan tertentu. Bagi IONEX, nilai TEC yang diberikan adalah simetri dengan merujuk garis geomagnet khatulistiwa yang dilukis pada garisan geografi 10ºU. Namun, kesan ini mempengaruhi bacaan TEC bagi setiap model. Daripada analisis, jelas menunjukkan bahawa dengan penggunaan model-model ini, berlakunya fenomena angin neutral yang menyebabkan tumpuan kawasan nilai TEC yang tinggi hanya pada kedudukan yang mempunyai kesan daya tarikan yang kuat iaitu menuju ke arah garisan khatulistiwa. Fenomena ini akan memberikan kesan yang amat ketara jika berlakunya fenomena anomali khatulistiwa yang selalunya berlaku pada waktu tengahari dan petang waktu tempatan. Dengan nilai elektron yang tinggi, nilai simetri yang diberikan akan lebih ketara lagi. Namun, walaupun analisis dilakukan pada awal pagi waktu tempatan di kawasan kajian, terdapat kekeliruan pada nilai TEC yang diberikan oleh setiap model terutamanya model IRI2001. Ini kerana kesan tidak simetri (adanya fenomena angin neutral) pada bacaan TEC di kedua-dua bahagian bumi telah ditunjukkan dalam anggaran TEC yang diberikan oleh model-model tersebut.

4.0 KESIMPULAN

Melalui kajian yang dijalankan di sekitar garisan longitud Khatulistiwa, didapati terdapat perbezaan pada TEC yang diperolehi dari kawasan daratan dan kawasan lautan kesan daripada kewujudan stesen-stesen penerima IGS di kawasan daratan. Namun kajian di sepanjang latitud bumi mendapati faktor lain yang turut mempengaruhi bacaan TEC adalah kesan angin neutral yang bergerak menuju ke garis Khatulistiwa pada musim panas dan menuju ke kutub pada musim sejuk. Jika tiada kehadiran angin ini, bacaan TEC akan mengalami keseimbangan dan simetri dengan garis geomagnet sebagai garis rujukan.

Dengan penggunaan model-model IRI2001 dan NeQuick, terdapat ralat berlaku dalam bacaan TEC yang diberikan jika dibandingkan dengan nilai TEC dari IONEX. Di antara kedua-dua model, tidak ada yang lebih unggul. Ini adalah disebabkan nilai R_{12} yang mempengaruhi nilai bacaan TEC yang dianggarkan bagi setiap model. Dengan nilai R_{12} yang tinggi, frekuensi kritikal isyarat radio akan meningkat dengan tidak linear. Ini berlaku terutamanya dalam nilai anggaran TEC yang diberikan oleh model IRI2001 seperti yang ditunjukkan dalam kajian ini. Walaubagaimanapun, pada keseluruhannya variasi TEC menunjukkan corak maksimum dan minimum yang sama pada kedua-dua model, IRI dan NeQuick. Adalah diharapkan hasil kajian ini dapat menyumbang kepada kajian ramalan cuaca angkasa yang sedang hangat dibincangkan pada masa ini, selain dari kajian perambatan radio. Model-model sedia ada juga perlu diperbaiki dari semasa ke semasa supaya lebih fleksibel pada mana-mana lokasi secara global.

5.0 PENGHARGAAN

Penulis merakamkan penghargaan kepada pihak MOSTI dan UKM di atas pembiayaan penyelidikan (SF04-01-02-SF191 dan UKM-KK-01-FRGS0042-206) yang diberikan. ■

```
     1                                                                END OF TEC MAP
     2                                                                START OF TEC MAP
  2007    11     3     1    30     0                                  EPOCH OF CURRENT MAP
     0.0  90.0 110.0   1.0 450.0                                      LAT/LON1/LON2/DLON/H
  102  104  106  108  110  112  114  116  118  120  122  124  126  128  130  132
  135  137  139  141  144
     1.0  90.0 110.0   1.0 450.0                                      LAT/LON1/LON2/DLON/H
  105  107  110  112  114  116  118  120  122  124  126  128  131  133  135  137
  139  141  144  146  148
     2.0  90.0 110.0   1.0 450.0                                      LAT/LON1/LON2/DLON/H
  108  110  112  115  117  119  121  123  126  128  130  132  134  137  139  141
  143  145  148  150  152
     3.0  90.0 110.0   1.0 450.0                                      LAT/LON1/LON2/DLON/H
  109  112  114  116  119  121  124  126  128  130  133  135  137  139  142  144
  146  148  151  153  155
     4.0  90.0 110.0   1.0 450.0                                      LAT/LON1/LON2/DLON/H
  110  112  115  117  120  122  125  127  130  132  134  137  139  141  144  146
  148  150  153  155  157
     5.0  90.0 110.0   1.0 450.0                                      LAT/LON1/LON2/DLON/H
  109  112  114  117  120  122  125  127  130  132  135  137  140  142  144  147
  149  151  153  156  158
     6.0  90.0 110.0   1.0 450.0                                      LAT/LON1/LON2/DLON/H
  107  110  113  116  119  121  124  127  129  132  135  137  140  142  144  147
  149  151  154  156  158
     7.0  90.0 110.0   1.0 450.0                                      LAT/LON1/LON2/DLON/H
  105  108  111  114  117  120  123  126  128  131  134  136  139  141  144  146
  149  151  153  155  158
```

Contoh Data IONEX

RUJUKAN

[1] Alnutt, J. E. 1989. *Satellite to ground radiowave propagation: Theory, Practice and System impact at frequency above 1GHz.* Peter Peregrinus Limited.

[2] Iyer, K.N., Joshi, H.P., Jivrajani, R.D. dan Aravindakshan, P. 1996. Comparative study of TEC near the crest of the equatorial anomaly with IRI model for solar minimum to solar maximum. *Advances in Space Research*, 18(6): pp. 233-236

[3] Bilitza, D. 2004. 35 years of International Reference Ionosphere – Karl Rawer's legacy. *Advances in Radio Science* 2(G.2): pp. 283-287.

[4] Coisson, P., Radicella, S.M. dan Nava, B. 2002. Comparisons of experimental topside electron concentration profiles with IRI and NeQuick models. *Annals of Geophysics* 45(1): pp. 111-116

[5] Walker, C. 2006. The global ionosphere models. http://www.vlba.nrao.edu/memos/sci/gps_ion/node3.html [20 Julai 2008].

[6] Bilitza, D. 2001. International Reference Ionosphere model. http://modelweb.gsfc.nasa.gov/ionos/iri.html [6 Mei 2008]

[7] Zhang, M.L., Shi, J.K., Wang, X., Wu, S.Z. dan Zhang, S.R. 2004. Comparative study of ionospheric characteristic parameters obtained by DPS-4 digisonde with IRI2001 for low latitude station in China. *Advances in Space Research* 33(6): pp. 869-873.

[8] Ling, K.S. dan Masri, T. 2002. Satellite pointer controller. Software, Universiti Malaysia Sarawak.

[9] Trísková, L. dan Chum, J. 1996. Hysteris in dependence of foF2 on solar indices. *Advance in Space Research* 18(6): pp. 145-148.

[10] Moore, A.W. 2006. IGS site guidelines. http://igscb.jpl.nasa.gov/projects/iglos/index.html [25 April 2008].

[11] Zhao, C.Y, Shum, C.K. dan Yi, Y.C. t.th. Ionosphere corrections of radar altimeters and calibration results of GFO. http://space.cr.nctu.edu.to/altimetryworkshop/Abstracts/028.doc [25 April 2008].

[12] Aarons, J. 1982. Global Morphology of ionospheric scintillations. *Proceedings of the* IEEE 70(4): pp. 360-378.

[13] Pawel, W., Dorota, G.-B. dan Israel, K. 2003. Regional ionosphere mapping with kridging and multiquadric methods. *Journal of Global Positioning Systems* 2(1): pp. 48-55.

[14] Su, S., Chao, C., Liu, C. dan Ho, H. 1996. Meridional Wind Effect on the seasonal/longitudinal distribution of equatorial density irregularities inferred from ROCSAT-1 observation. http://www.agu.org/meetings/sm06_sessions/sm06_SAA43C.html [20 Oktober 2005].

[15] Cander, Lj.R., Bertram, A.-B., Barclay, L., Casimiro, A., Patrick, L.-D., Nava, B., Martinecz, C., Kouris, S., dan Leitinger, R. 2005. Meeting of COST296 Rapporteur Group on ITU Iono Work, IGAM, University of Graz, 4-5 Julai. http://www.cost296.rl.ac.uk/pdf/COST296_ITUR_Rapp_group_RL.pdf [25 April 2008].

[16] Rush, C.M. 1988. URSI foF2 Model Maps 1988. http://modelweb.gsfc.nasa.gov/ionos/ursi.html [25 April 2008].

[17] Franklin, C.A. dan Maclean, M.A. 1969. The design of swept-frequency topside sounders. *Proceeding of* IEEE, 57(6): pp. 897-929.

[18] Rush, C.M., Pokempner, M., Anderson, D.N., Stewart, F.G. dan Perry, J. 1983. Improving ionospheric maps using theoretically derived values of foF2. *Radio Science* 18(1): pp. 95.

[19] Rush, C.M., Pokempner, M., Anderson, D.N., Perry, J., Stewart, F.G. dan Reasoner, R. 1984. Maps of foF2 derived from observations and theoretical data. *Radio Science* 19(4): pp. 1083.

[20] Comité Consultatif International des Radiocommunications (CCIR) t.th. CCIR foF2 and M(3000)F2 Model Maps 1982. http://modelweb.gsfc.nasa.gov/ionos/ccir.html [28 April 2008].

[21] Rama Rao, P.V.S., Sri Ram, P., Jayachandran, P.T. dan Prasad, D.V.V.D. 1996. Seasonal variation in ionospheric electron content and irregularities over Waltair – a comparison with SLIM model. *Advance Space Research* 18(6): pp. 259-262.

PROFILES

IR. ASSOC. PROF. DR MARDINA ABDULLAH

Dr Mardina Abdullah received her B. Eng degree from University of the Ryukyus, Japan in Electronics and Information Engineering in 1991. She obtained her M.Sc degree from Universiti Kebangsaan Malaysia (UKM) in Electrical, Electronic and System Engineering in 1995. In 2004, she was awarded a PhD degree in Electrical Engineering from The University of Leeds, UK for a work on ionospheric effects on GPS range finding and precise positioning. She is interested in ionospheric studies, GPS satellite error mitigation and expert systems.

MS. DAYANG AZRA AWANG MAT

Dayang Azra Awang Mat received her bachelor degree in Electronic and Telecommunication from Universiti Malaysia Sarawak in 2002, and obtained her M.Sc degree from Universiti Kebangsaan Malaysia in 2006. She is currently a lecturer at Faculty of Engineering at Universiti Malaysia Sarawak (UNIMAS). Her research interests are mobile and wireless technology and ionospheric sciences.

MS. SITI SARAH NIK ZULKIFLI

Siti Sarah Nik Zulkifli received her B. Information Technology degree majoring in Software Engineering from University Malaysia Terengganu (2005). She is currently pursuing her masters' degree in the Department of Electrical, Electronic and Systems Engineering at Universiti Kebangsaan Malaysia. Her research of interests lies in the field of transionospheric propagation focusing on ionospheric effect on Global Positioning System.

A CONCEPT DEVELOPMENT AND PROPOSED DESIGN PROCEDURE FOR ROCKING PRECAST HOLLOW CORE WALL IN WAREHOUSE

(Date received: 18.2.2008)

Nor Hayati Abdul Hamid[1]
[1]Senior Lecturer, Faculty of Civil Engineering,
Universiti Teknologi MARA, 40450 Shah Alam, Selangor
E-mail: [1]abdulhamid_nrhyt@yahoo.com

ABSTRACT

Precast hollow core unit is commonly used in the construction of flooring system in precast reinforced concrete building in Malaysia. One of the technical challenges is to design and use precast hollow core unit without any transverse reinforcement bars to resist earthquake loading. One of the approachable methods is to combine the basic concept of rocking structure together with Damage Avoidance Design (DAD) philosophy. Moreover, Performance-Based Seismic Engineering Design concept is also incorporated in this study so that reinforced concrete structure can survive under Design Basic Earthquake (DBE) and Maximum Considered Earthquake (MCE). In this study, the total effective viscous damping ξ_{eff} plays an important role in designing seismic wall panel which comprises of hysteresis damping (ξ_{eq}), radiation damping (ξ_{rock}) and intrinsic damping (ξ_{inst}). Another attributes which also plays a significant role in plotting capacity-demand spectrum for any location in seismic regions is damping reduction factor (B). By combining the capacity-demand spectrum and concept of rocking structure, a proposed design procedure of warehouse buildings using PHCW is developed and proposed. The proposed design procedure consists of seven steps which are determination of seismic demand, maximum response displacement for MCE and DBE, estimation of total effective damping, calculation of base shear, design of energy dissipator and unbonded tendons, evaluation hysteresis and total damping, and finally, the assessment of seismic capacity of rocking wall. In this study, it is expected that the rocking precast hollow core wall can reduce a substantial amount of structural damage and remain functional after an earthquake.

Keywords: *Steel-armouring, Rocking Structures, Damage Avoidance Design Philosophy, Hysteresis Loops, Performance-based Seismic Engineering*

1.0 INTRODUCTION

From past earthquakes records such as the 1999 Kocaeli Earthquake, the 1999 Chi Chi Earthquake and the 1994 Northridge Earthquake which caused quite substantial damage to the industrial facilities and warehouses, high-tech computer industries, parking garages and precast concrete structures. The conventional method of designing shear wall using ductile design philosophy has failed in preventing these buildings from surviving under major earthquake and did not maintain post-earthquake serviceability. Normally in seismic regions, longitudinal and transverse reinforcement bars were used in shear wall to resist earthquake loading. Therefore, it is a motivation for civil engineers to design shear wall such precast hollow core unit without transverse reinforcement as shear wall panel which can resist ground motion without any structural damage. Thus, one of the challenging tasks is to design and modify precast hollow core units to resist vertical and seismic loading with the existence of longitudinal prestressed strand only. By adopting the concepts of Damage Avoidance Design (DAD) philosophy and rocking structures along with damage protection, the rocking toe at wall-foundation interfaces could litigate high stress zone and resist these loads efficiently. However, it is legitimated to provide transverse reinforcement bars in precast wall panels and shear wall as required by most of standard design seismic code such as Eurocode 8 [1], IBC 2000 [2], NZ 3101 [3], ATC-40 [4] and others.

Due to poor performance of industrial and warehouse buildings during these earthquakes, the conventional design philosophy needs to change to the new design philosophy which could maintain post-earthquake serviceability of the structures. Which mean that a new design concept together with a new form of construction for industrial facilities is necessary to avoid any damage entirely during earthquakes. Therefore, the main objective of this paper is to develop a rocking concept and proposed a new design procedure for precast hollow core wall system which can be used in the construction of industrial facilities. In this procedure, the discontinuous interface between wall-foundation could prevent the occurrence of plastic hinge zone and at same time could avoid any spalling and crushing of concrete at toe of the wall. The rocking concept between interfaces plays an important role in dissipating energy after the impact of earthquake excitation.

2.0 FINDING FROM PREVIOUS RESEARCH

A significant amount of research has been conducted on rocking structures under earthquake motion. The first rocking rigid body kinematic concept was developed by Housner [5] who studied the free vibration of rigid block during earthquake excitation. Then, Meek [6] investigated the aspects of structural flexibility rocking on foundation beam. The improvement of rocking concept was followed by Priestley *et. al* [7] who introduced the seismic dynamic response of rocking structures on their foundation. Aslam *et. al* [8] considered the influence of initial prestress with some resistance to the rigid structure by anchoring the concrete block to the ground floor. Further research was carried out by Yim *et. al* [9] who studied the effect of sizes, slenderness ratio and ground motion to the seismic response of rigid blocks. Subsequently, Psycharis and Jennings [10] discovered that there was a partial separation between the base of block and foundation during ground shaking. Then, they modelled two types of foundation beams as two-spring foundation and Wrinkler foundation which allowed uplifting but did not permit any slip in horizontal direction. Later on, Lin and Yim [11] examined the nonlinear rocking motions under noisy periodic excitations and overturning of rigid body under random excitations.

The concept of prestressing unbonded tendons in beam-column connection was developed by Priestley and Tao [12] and demonstrated through experimental work by Priestley and MacRae [13]. This was followed by Kurama *et al*. [14] who proposed a seismic design procedure of unbonded post-tensioned tendons walls by taking into account the horizontal slip. Subsequently, Kurama [15] recommended a simplified seismic design procedure under performance based design using unbonded post-tensioned precast wall panels with supplemental viscous damping. Even though Precast Seismic Structural System (PRESSS) adapted direct displacement based design procedure but it did not specified the steel-armoured detailing especially at wall-foundation and beam-column connections [16]. Consequently, Damage Avoidance Design (DAD) was introduced by Mander and Cheng [17] using a steel-armouring rocking interface at the rocking toe to accommodate high contact point forces and prevent any local damage. By adopting the rocking rigid body concepts on the design and construction of bridge piers, the structural damage can be avoided by using special steel-armoured details at the bottom of the bridge column. Some other researchers who used Damage Avoidance Design philosophy in designing and constructing precast reinforced concrete wall panels are Holden *et al*. [18], Surdano [19], Ajrab *et al*. [20], Liyanage [21] and Hamid [22] had proven that no structural damage occurred at wall-foundation interfaces. Contradictorily, Hamid and Surdano [23] had designed precast slender/thin wall using conventional method, constructed and tested under dynamic loading. The visual observation during experimental work showed that a lot of damage occurred at bottom of wall such spalling of concrete, fractured of longitudinal bars and lateral torsional buckling. A substantial damage was also observed on monolithic based connection of slender/thin wall which designed using ductile design approach when tested under biaxial loading [24]. Further improvement was made on thin/slender wall panel by designing rocking base connection and tested under biaxial quasi-static loading. The experimental results showed that less damage was occurred but the outermost longitudinal reinforcement bars were fractured after applying the lateral loading [25]. Therefore, the intentions of this paper are to develop the basic concept of rocking wall panel using precast hollow core units, derive the effective viscous damping and proposed a new procedure for construction rocking structures.

3.0 DAMAGE AVOIDANCE CONCEPT (DAD) IN WAREHOUSES

Figure 1 shows the prototype model of warehouse building constructed using precast hollow core walls and designed under Damage Avoidance Design philosophy. The multi-panel walls consist of seismic and non-seismic walls which are designed to resist gravity, longitudinal and transverse loads (wind and seismic load). The rafter of portal frames is sitting on seismic wall which carrying the roof loads and resist the transverse loads. Figure 1(a) shows the horizontal bracing elements along the top edges of the roof which are designed to resist longitudinal loads and the portal frame with seismic wall as a vertical element to resist transverse loads. The longitudinal and transverse loads represent the loads which coming from earthquakes.

Figure 1(b) shows the plan view of a warehouse with their seismic and non-seismic walls, wind trusses and rafter with portal frame. The numbers of non-seismic walls are depending on the spacing of rafter sitting on seismic walls. The portal frames are bolted to a steel channel web using unbonded tendons located in the center of the void sections of seismic walls and it also activated as a load bearing wall without constructing external columns.

Figure 1(c) shows the cross-section *x-x* of the portal frame together seismic wall panel. The detail connection 'A' shows the connection between top of the walls and edges of portal frames and connection 'B' depicted detail joint between wall-foundation interfaces. The seismic walls are attached to the foundation beam using couplers (RB25C). They allow to rock freely on foundation beam and at the same time acting as external column. The detailing of drawing can are shown in Hamid [22].

Figure 2 shows the overall behaviour of a seismic wall comprising a pair of unbonded tendons and energy dissipators. By using the concept of rocking structures and Damage Avoidance Design (DAD) are adopted in designing this type of warehouse building. The rocking seismic wall is modelled as Single Degree of Freedom (SDOF) where the combination behaviour of unbonded tendons and gravity load behaved as Bi-Linear Elastic as shown in Figure 2(a). The radiation damping, ξ_{rock} from unbonded tendons is produced during uplifting and yielding of unbonded tendons. Figure 2(b) represents the behaviour of fuse bars/tapered energy dissipator as Ramberg-Osgood hysteresis loop and the hysteretic damping, ξ_{hyst} creates after yielding energy dissipators. Figure 2(c) produce the total effective damping, ξ_{eff} which behaved like a "flag-shape". The initial prestressing, locations and cross-sectional area of unbonded tendons and energy dissipators are the important attributes in determining the amount of base shear capacity, yielding drift, and the behaviour of a rocking wall system.

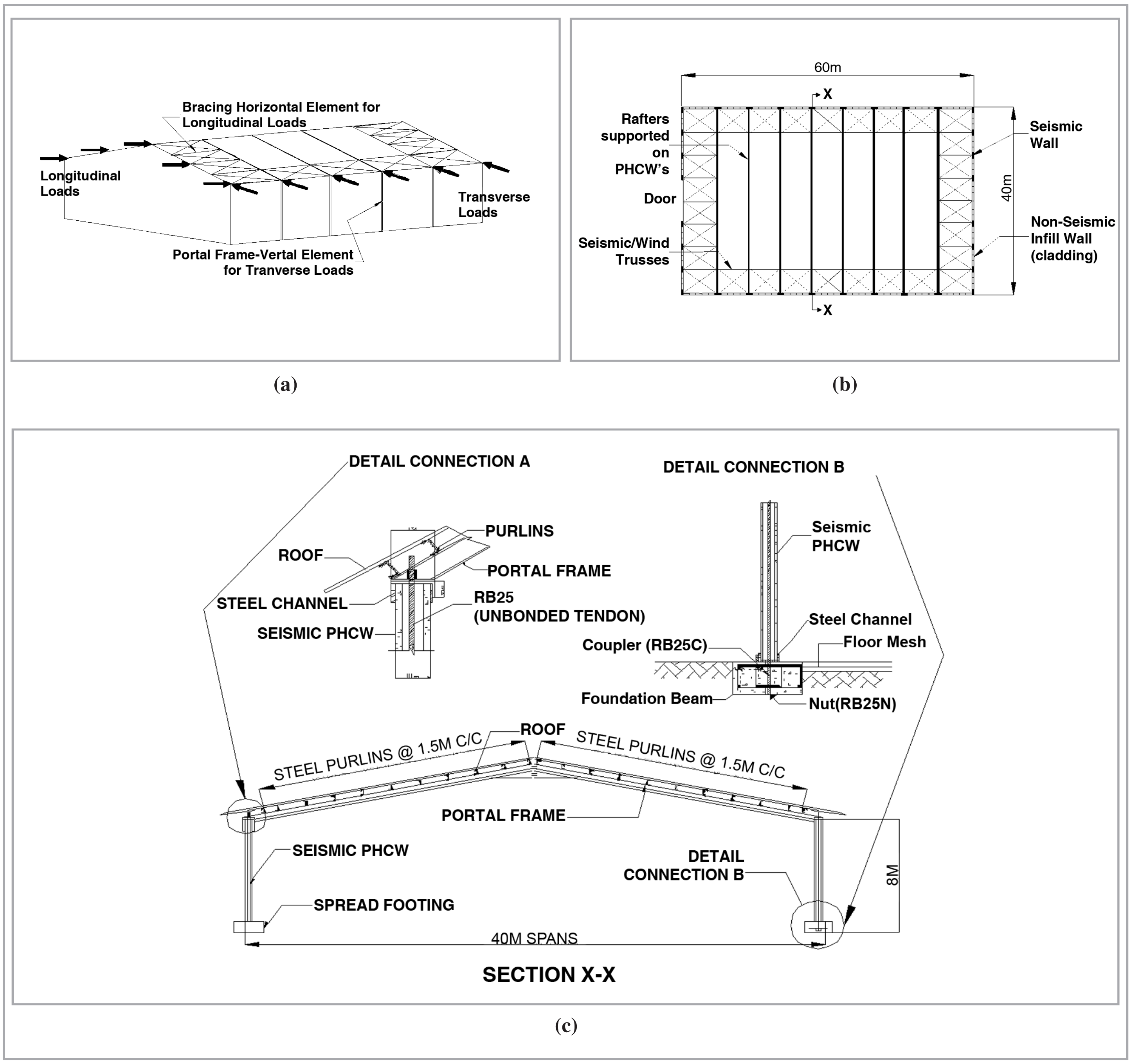

Figure 1: Concept overview of warehouse building; (a) distribution of transverse and longitudinal loading arising from either wind or earthquake effects; (b) plan view of warehouse showing lines of portal frames seated on PHCW; (c) steel portal frame setting on PHCW together with detailing connection at top and bottom of the wall

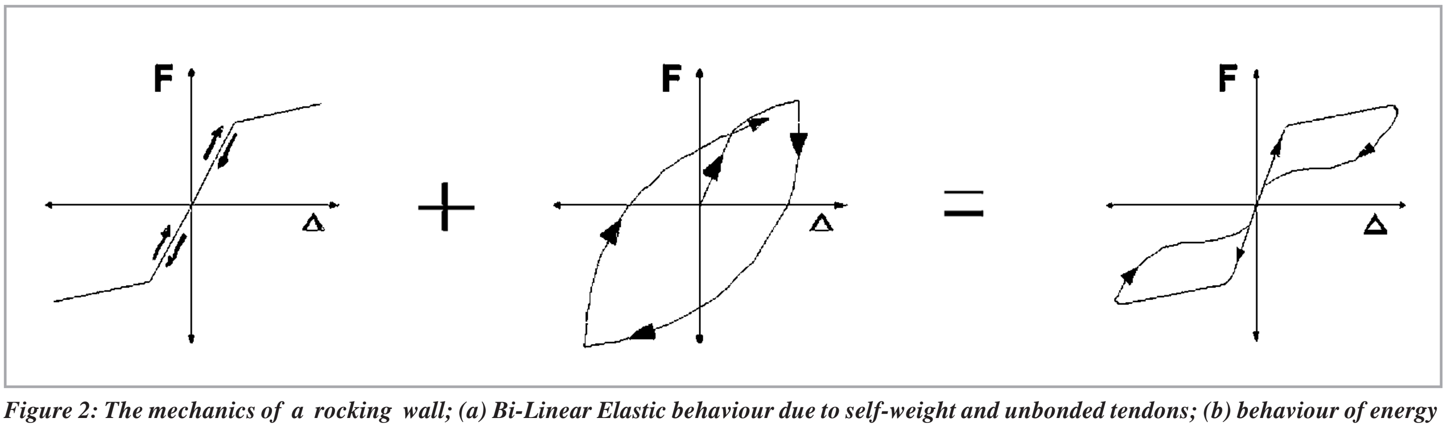

Figure 2: The mechanics of a rocking wall; (a) Bi-Linear Elastic behaviour due to self-weight and unbonded tendons; (b) behaviour of energy dissipators; (c) hysteresis of flag-shape

4.0 DAMPING IN ROCKING STRUCTURES WITH ADDED HYSTERETIC ENERGY DISSIPATION

4.1 Effective Viscous Damping

In the rocking system and Damage Avoidance Design (DAD), the total effective viscous damping, ξ_{eff} comes from hysteretic loops, intrinsic structures damping and radiation damping which can be expressed:

$$\xi_{eff} = \xi_{rock} + \xi_{hyst} + \xi_{inst} \tag{1}$$

where ξ_{hyst} is the additional damping from the energy dissipator devices, ξ_{rock} is the radiation or dissipated energy from each rocking cycle including tendons, ξ_{inst} is the intrinsic damping due to the internal structures of the system. The typical values of intrinsic damping used by the structural engineers are 2% for steel and 5% for reinforced concrete building [26].

It is also can be written as follows [24]:

$$\xi_{eff} = \xi_{inst} + \xi_{rock} + \frac{2\eta}{\pi}\left[\frac{1}{1-r(\mu-1)} - \frac{1}{\mu}\right] \tag{2}$$

In Equation 2, the term ξ_{hyst} is replaced by energy absorption efficiency factor (η) ; while r = the post-elastic to initial stiffness ratio and μ = the structural displacement ductility.

4.2 Radiation Damping in Rocking Structures

The radiation damping can be assessed by considering two conditions as pre-rock damping when unbonded tendons is not yielding and post-rock damping after unbonded tendons yielded. The radiation damping for one impact per half-cycle of the rocking system is given by

$$\xi_{rock} + \frac{E_p(1-r)}{\pi F\Delta} \tag{3}$$

where r is ratio of rotation kinetic energy after to before impact; F is the uplift force and Δ is the displacement amplitude. The amount of potential energy, E_p when the tendons did not yield is given by the following equation:

$$E_p = \frac{B\sin\theta}{2}\left[W + \frac{1}{2}\left[K_p\theta + \frac{2K_pL_T\varepsilon_o}{B} + \varepsilon_o\right]\right] \tag{4}$$

By substituting $rs = \dfrac{K_pL_T}{WB}$ into Equation 4, and the equation becomes:

$$E_p = \frac{B\,\theta W}{2}\left[1 + \frac{r_sB\theta}{2L_T} + r_s\varepsilon_o\right] \tag{5}$$

The amount of potential energy when the tendons are yielding is given by:

$$E_p = \frac{WB\theta}{2}\,[1 + r_s\,(2\varepsilon_{max} - \varepsilon_y - \varepsilon_o)] \tag{6}$$

where B is the width of wall, W is total weight of wall, K_p is the initial stiffness of unbonded tendons, L_T is the total length of unbonded tendons, θ is the drift level, ε_{max} is the maximum strain, ε_y is the yield strain and ε_o is the initial strain of unbonded tendons.

The base shear capacity of the seismic wall at pre-rock is given by :

$$C_c = \frac{F}{W} = C_{c\,(pre-rock)} = \frac{B}{H_w}\left[1 + \frac{r_sB\Delta}{L_TH_w} + r_s\varepsilon_o - \frac{\Delta}{B}\right] \tag{7}$$

The base shear capacity of the seismic wall at post-rock is given by:

$$C_{c(rock)} = \frac{B}{H_w}\left[1 + \frac{r_sWH_w\varepsilon_y}{L_T} - \frac{\Delta}{B}\right] \tag{8}$$

Thus, radiation damping of the rocking wall under pre-rocking conditions is derived by substituting Equations 5 and 7 into Equation 3 and becomes:

$$\xi_{r(pre-rock)} = \frac{(1-r)\left[1 + \dfrac{r_sB\theta}{2L_T} + r_s\varepsilon_o\right]}{\pi\left[1 + \dfrac{r_sB\Delta}{L_TH_w} + r_s\varepsilon_o - \dfrac{\Delta}{B}\right]} \tag{9}$$

The radiation damping under post-rock conditions when the tendons are yielding is derived by substituting Equations 6 and 8 into Equation 3 and the equation becomes:

$$\xi_{r(post-rock)} = \frac{(1-r)\,\{1 + r_s\,(2\varepsilon_{max} - \varepsilon_y - \varepsilon_o)\}}{\pi(1 + \dfrac{r_sWH_w\varepsilon_y}{L_T} - \dfrac{\theta H_w}{B}} \tag{10}$$

4.3 Hysteretic Energy Dissipation and Equivalent Viscous Damping

The equivalent viscous damping by considering the energy absorption efficiency factor of energy dissipator is given by:

$$\xi_{eq} = \frac{2\eta(1-r)\left[1 - \dfrac{1}{\mu}\right]}{\pi(1 - r + \mu r)} \tag{11}$$

where r is the post-elastic to initial stiffness ratio, μ is the structural ductility and η is energy absorption factor. Energy absorption efficiency factor (η) is defined as the ratio of area enclosed by the energy dissipater hysteretic loops over the Elasto-Perfectly-Plastic (E_{EPP}) which represented by area of trapezoid loops as given by the following equation.

$$\eta = \frac{Eh}{E_{EPP}} \tag{12}$$

where Eh is absorbed hysteretic energy observed during a characterisation and E_{EPP} is the total energy dissipated by a theoretical elasto-perfectly plastic system.

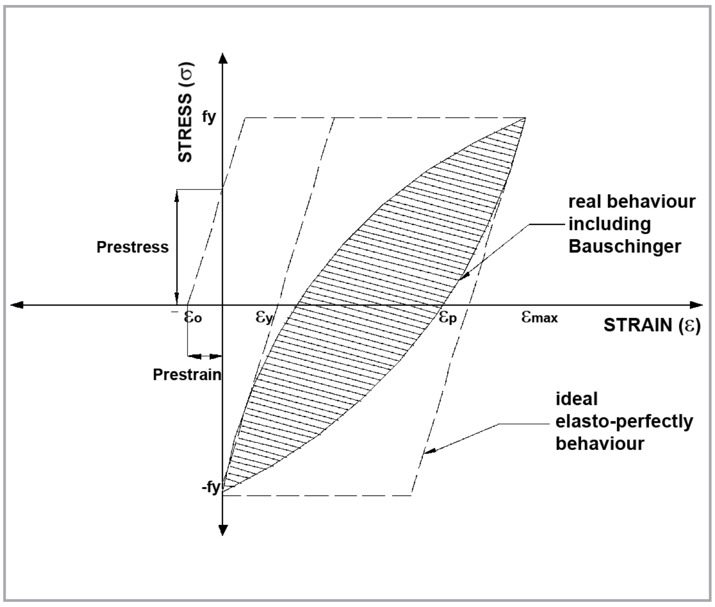

Figure 3: The Bauschinger effects on the hysteretic energy absorption efficiency of fuse-bars/energy dissipators

Figure 3 shows the Bauschinger effect on the energy absorption efficiency of fuse/energy dissipator. The trapezoidal area of ideal elasto-perfectly plastic area is given by the following equation:

$$A_{trapezoid} = 2F_y \times (\Delta_u - 2\Delta_y) \tag{13}$$

where $A_t = \frac{1}{4} A_{trapezoid}$, F_y is the maximum yield strength of energy dissipators, Δ_u is the ultimate displacement and Δ_y is the yield displacement.

5.0 REDUCTION DAMPING FACTORS

In the IBC-2000, the reduction damping factor B are independent of the soil types where the structures located. Lin and Chang [27] pointed out that the reduction damping factors, B had a great effects on the site soil characteristics. Figure 4 shows the proposed spectrum demand capacity based on reduction damping factors. Figure 4(a) proposed reduction damping factor based on acceleration response spectrum, B_a is given by Equation 14 and reduction damping factor based on displacement response spectrum, B_d is given by Equation 15. The linear interpolation in Equation 16 denote as B_v which derived between plateau B_a and plateau B_d based on site classes, period and damping ratio.

For $S_d < S_{da} = 0.079m$,

$$\text{then} \quad B_a(\xi_{eff}) = \sqrt{\frac{2 + \xi_{eff}}{7}} \tag{14}$$

For $S_d < S_{da} = 0.469m$,

$$\text{then} \quad B_d(\xi_{eff}) = \sqrt{\frac{8 + \xi_{eff}}{13}} \tag{15}$$

For $S_d = S_{dv}$ and $S_d < S_{da} < S_{dd}$, then

$$B_v(\xi_{eff}) = \frac{B_d(S_{dv} - S_{da}) - B_a(S_{dv} - S_{dd})}{S_{dd} - S_{da}} \tag{16}$$

Figure 4(b) represents the mean reduction damping factors corresponding to site classes AB, C and D for damping ratios of 10, 20, 30 and 50%. Figure 4(c) shows the spectral response acceleration at different damping factor by incorporating the reduction damping factors for period up to 2 seconds. Figure 4(d) represents the overall design capacity-demand spectrum at various effective damping of 5%, 10%, 20% and 30% by incorporating the reduction damping factors. In this study, the effective viscous damping of 10% is adopted for warehouse buildings.

6.0 CAPACITY SPECTRUM DESIGN METHODOLOGY

The capacity-demand spectrum becomes popular in seismic prone regions where a realistic evaluation of the earthquake hazard is analysed in assessing the structural response. The seismic demand spectrum of the hazard exposure can be predicted based on the statistical analysis of the past earthquake records. The equations that control a smooth model for 5% damped elastic response spectrum are according to equation derived by Martinez [28]. The evaluation of the seismic demand spectrum on various effective damping is depending on the portion of the spectrum that governs duration of structural response. The reduction damping factor can be categorised as short period and long period. The seismic demand spectrum of short period is in Equation 17 and long period is in Equation 18.

$$\text{Cd} = \frac{F_a S_s}{B_a} \tag{17}$$

$$\text{Cd} = \frac{F_v S_1}{T B_v} \tag{18}$$

whereby F_a and F_v are adjustments on spectral acceleration for short, intermediate and long periods for different site classes, S_s and S_1 are spectral acceleration at short periods and one second periods, B_a, B_v and B_d are the seismic displacement reduction damping factors for short, intermediate and long term period of the structures. For intermediate period of vibration, the capacity demand spectrum can be expressed as a function of spectral displacement. The demand of the natural period of vibration is given by the well-known Equation 19.

$$\text{T} = 2\pi \sqrt{\frac{\Delta}{C_c g}} \tag{19}$$

By replacing $\Delta = S_d$ and substituting Equation 19 into Equation 17, then it becomes:

$$C_d = \left[\frac{F_v S_1}{2\pi B_v}\right]^2 \frac{g}{S_d} \tag{20}$$

By equating capacity demand spectrum, C_d with capacity base shear of the structures, C_c then spectral accelerations can be defined as:

$$F_vS_1 = 2\pi B_v\sqrt{\frac{S_dC_c}{g}} \qquad (21)$$

To survive under DBE and MCE, the spectral acceleration generated by base shear capacity of rocking wall should be bigger than or equal to the capacity demand of the spectrum, as defined in Equation 22 must be satisfied:

$$\Phi\,(F_vS1)c \geq (F_vS1)d \qquad (22)$$

where Φ = under capacity factor that relates global uncertainty of seismic performance = 0.65.

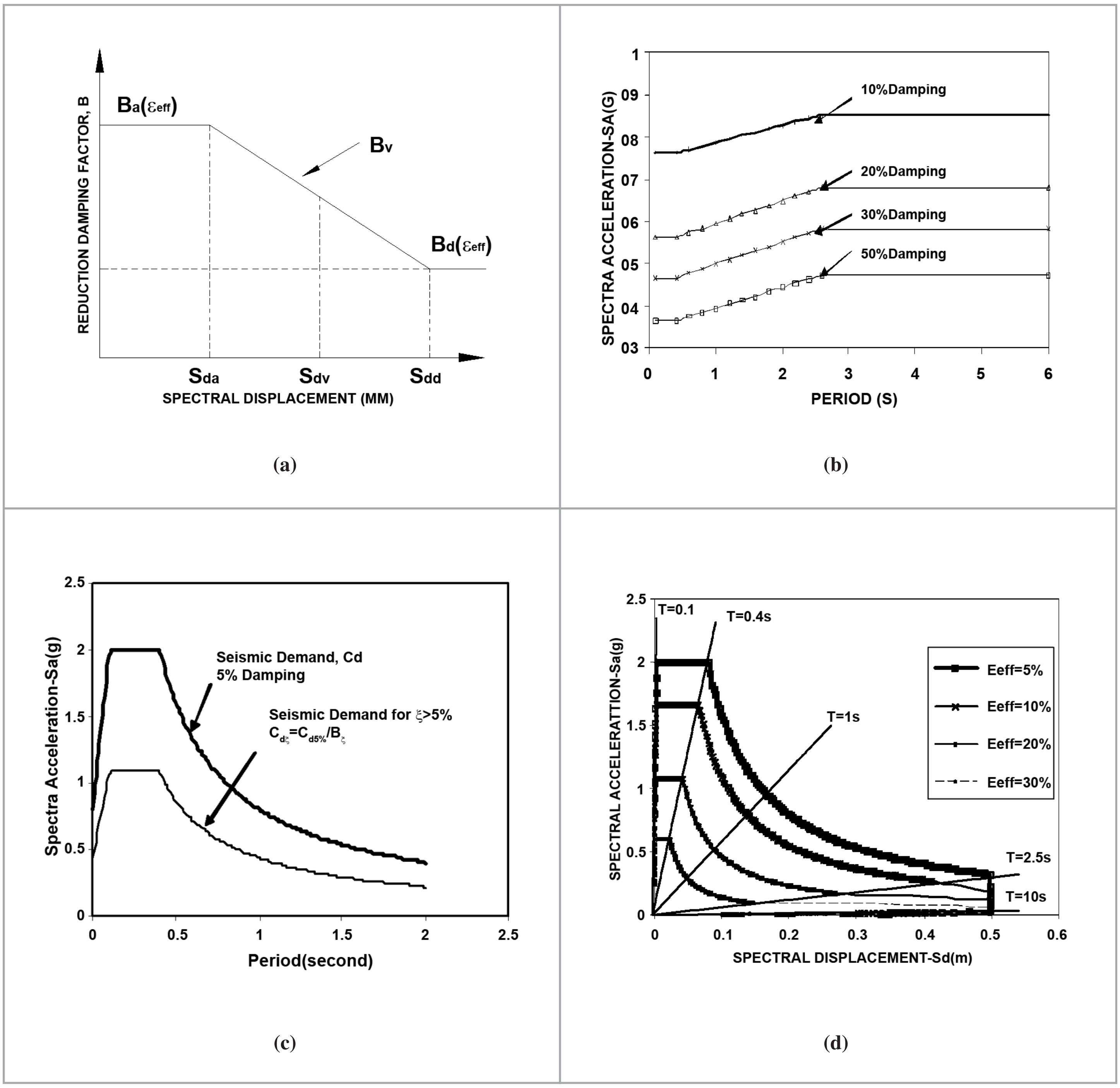

Figure 4 : The proposed reduction damping factor and spectrum demand capacity for precast hollow core wall ; (a) reduction damping reduction factor, B based on spectral amplitude; (b) mean damping reduction factors based on displacement response; (c) spectral acceleration vs period; and (d) the design spectra based on the reduction damping factor

7.0 PROPOSED DESIGN PROCEDURE FOR ROCKING WALL PANEL

After developing the theoretical parts of rocking wall, the next step is to proposed design procedure for this type of wall. There are seven steps involve in the proposed design as listed below:

STEP 1: Determine Seismic Demand of DBE and MCE based on the Hazard Exposure

First of all, select at least a set of 30 ground motion records based on different locations of past earthquake. Then, 5% damped response acceleration must be parameterised to the scale of 1g for 1 *sec* period curves. Table 3 shows the proposed 5% damped response spectrum curve.

STEP 2: Determine the Maximum Response Displacement, Δ^{DBE}_{max} and Δ^{MCE}_{max}

By substituting $Sd = \theta_{max} = Heff$ as maximum response displacement into Equation 21, then the equation becomes:

$$Sd = \Delta^{DBE}_{max} = \Delta^{DBE}_{max} = \frac{(FvS1)^2{}_d g}{4\pi^2 BvCc} \tag{23}$$

Table 3: Proposed 5% damped elastic seismic demand spectrum

Duration (second)	*Spectral Accelerations (g)*	*Spectral Displacement (m)*
$0 < Ti < 0.10$	$Sa = Sg\left[1 + 1.50\left[\frac{Ti}{0.10}\right]\right]$	$Sd = \frac{SaT_i^2 g}{4\pi^2}$
$0.1 < Ti < 0.40$	$Sa = 2.50Sg$	
$0.40 < Ti < 2.50$	$Sa = \frac{SgT1}{Ti}$	
$2.50 < Ti < 10$	$Sa = \frac{SgT1T2.5}{T_i^2}$	$Sd = \frac{SaT1T2.5g}{4\pi^2} = const$
$Ti > 10.00$	$Sa = \frac{4\pi^2 PGD}{g\ Fri}$	$Sd = \frac{SaT_i^2 g}{4\pi^2}$

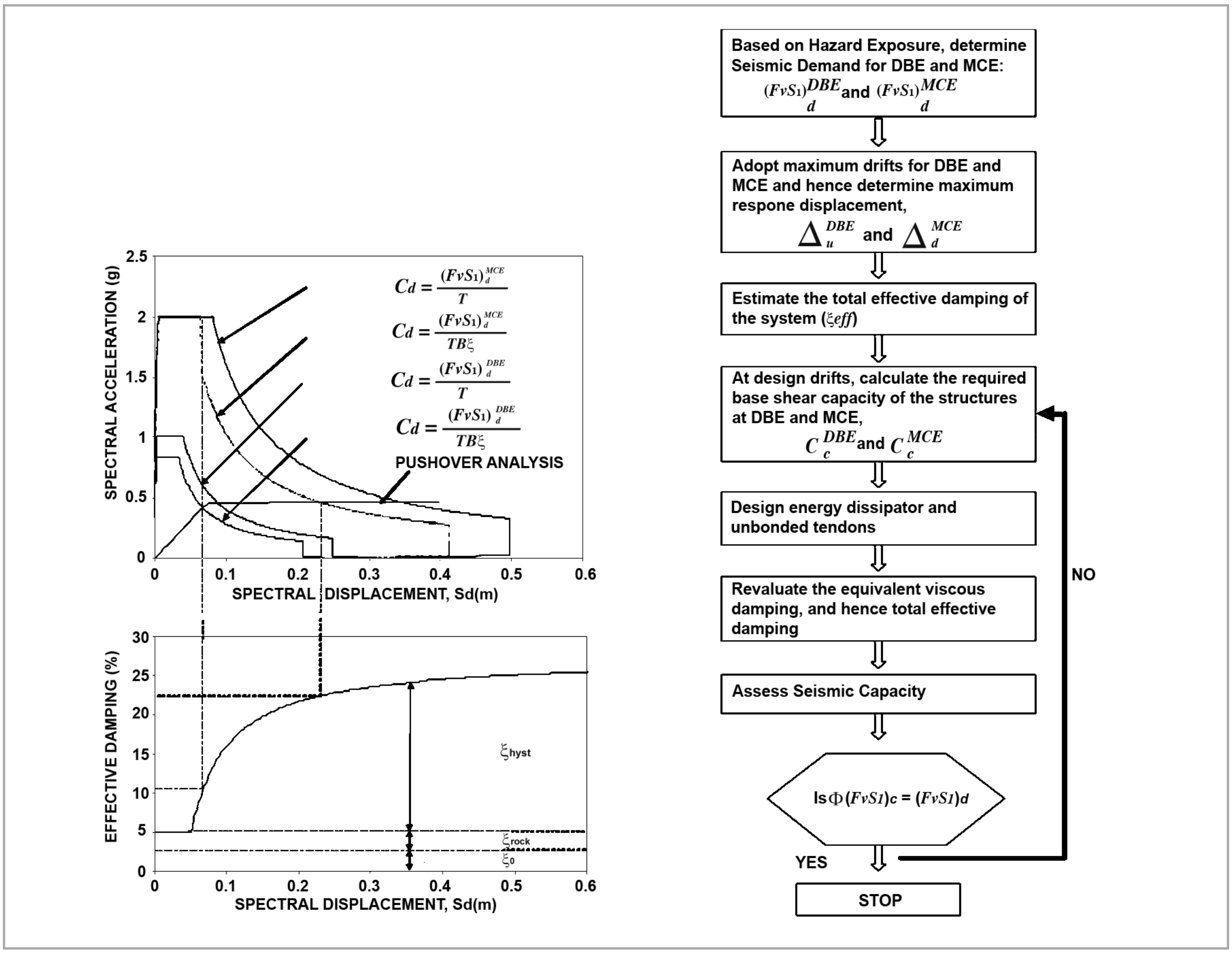

Figure 5: Flow chart showing the proposed design procedure for rocking precast hollow core walls using Damage Avoidance Design (DAD) philosophy

STEP 3 : Estimate Total Effective Damping of the System (ξeff)

Total estimate effective damping of the system can be found by projecting the vertical line from a point where the structural bilinear capacity curve meets the demand capacity spectra of DBE and MCE to the curve of effective viscous damping based on Equation 23.

STEP 4: Calculate Base Shear Capacity of the Structures, C_c^{DBE} and C_c^{MCE}

The base shear capacity of the structure can be determined using base shear demand of Equation 24. The hysteretic cyclic behaviour of rocking walls depends on the percentage of moment contribution coming from each of the tendons and energy dissipators.

STEP 5: Design Energy Dissipator and Unbonded Tendons

Once the percentage of energy dissipators and tendons are determined, the yield forces of energy dissipators and unbonded tendons can be calculated, where is the cross-sectional area of the energy dissipators and tendons, respectively and is the characteristic strength of energy dissipators and tendons, respectively.

STEP 6: Evaluation of Hystresis Damping and Total Effective Damping of the System

The pre-rock damping, $\xi_{pre-rock}$ and rock damping, ξ_{rock} of the wall system can be calculated using Equations 9 and 10, respectively. The actual hysteretic damping of energy dissipators can be calculated using Equation 11. Hence, the total amount of effective damping of the system is evaluate using Equation 2.

STEP 7: Assessment of Seismic Capacity

The seismic capacity of precast hollow core wall system can be assessed by checking that the base shear capacity of the system is bigger than the base shear demand at two levels of earthquakes using Equation 22. If these values do not converge, Steps 4 to 6 is repeated until they are converged and the design is accepted.

Figure 5 show flow chart representing the proposed design procedure using rocking precast hollow core walls by applying Damage Avoidance Design (DAD) philosophy. An example of a typical single storey warehouse building using precast hollow core wall which designed to resist earthquake loading with intensity VII is demonstrated in Hamid [22].

8.0 CONCLUSIONS AND RECOMMENDATIONS

The conclusions and recommendations which drawn from this paper are as follows:

1. The basic concept of rocking wall panel can be used for designing and construction of industrial/warehouses buildings, residential houses and commercial buildings in high and medium seismic regions.
2. The effective damping coming from unbonded tendons and energy dissipators can be determined by adjusting the level of prestressing and cross-sectional area of unbonded tendons and external energy dissipators. It is proposed that about 14% of total effective damping to be used in this design.
3. The proposed design procedure using Damage Avoidance Design (DAD) philosophy for the construction of warehouse buildings can be implemented in high seismic regions such Sumatra, Java Islands, New Zealand and others countries.
4. It is recommended that Damage Avoidance Design (DAD) philosophy together with rocking concept of structures can be extended to other structures components such as beam-column connection, slab-beam connection, bridge-piers and Industrialized Building System (IBS). ■

REFERENCES

[1] Eurocode 8 (2004): Design of Structures for Earthquake Resistance: Part 1: General Rules, Seismic Actions and Rules for Buildings, BS EN 1998-1:2004, Thomas Telford.

[2] IBC 2000 (2000): International Building Code, United States of America.

[3] NZS 3101: 1995: Concrete Structures Standard, Part 1: “The Design of Concrete Structures”, Standards Association of New Zealand Wellington, 1995.

[4] ATC-40 (1995) : Applied Technology Council. “ Guidelines and commentary for the Seismic rehabilitation of buildings.” ATC-40, Redwood City, California.

[5] Housner, G. W. (1963). "The Behaviour of Inverted Pendulum Structures during Earthquake. "*Bulletin of the Seismological Society of America*, Vol. 53, No. 2 (February, 1963), pp 403-417.

[6] Meek, J.W.(1975)."Effects of Foundation Tipping on Dynamic Response." *Journal Structural Division*, ASCE, 101(7), pp 1297-1311.

[7] Priestley, M.J.N., Evison, R.J., and Carr, A.J. (1978). "Seismic Response of Structures Free to Rock on their Foundation, "Bulletin of the New Zealand National Society for Earthquake Engineering, Vol. 20, No. 3, September 1987, pp 141-150.

[8] Aslam, M. Goddon, W.G., and Scalise, D.T., (1980). "Earthquake Rocking Response of Rigid Bodies." *Journal of Structural Engineering*, ASCE, Vol. 106, No.2, February 180, pp 377-392.

[9] Yim,C-S., Chopra, A.K., and Penzien, J. (1980). "Rocking Response of Rigid Blocks to Earthquake," *Earthquake Engineering and Structural Dynamics*, Vol. 8, pp 565-587.

[10] Psycharis, I.N. and Jennings, P.C. (1983). "Rocking of Slender Rigid Bodies Allowed to Uplift," *Earthquake Engineering and Structural Dynamics*, Vol.11, pp 57-76.

[11] Lin, H., and Yim, S.C.S. (1996a). "Nonlinear Rocking Motions. I: Chaos under Noisy Period Excitations, "*Journal of Mechanical Engineering*, ASCE, Vol. 122, No.8, August 1996, pp 719-727.

[12] Priestley, M.J.N, and Tao, J.(1993)."Seismic Response of Precast Prestressed Concrete Frames with Partially Debonded Tendons, PCI *Journal*, Vol. 38, No.1, January-February 1993, pp 58-69.

[13] Priestley, M.J.N, and MacRae, G.A. (1996) "Seismic Testing of Precast Beam-to-Column Joint Assemblage with Unbonded Tendons," PCI *Journal*, Vol. 41, No.1, pp 64-80.

[14] Kurama, Y., Dessiki, S., Sause, R., and Lu, L.-W. (1998). "Seismic Behaviour and Design of Unbonded Post-tensioned Precast Concrete Walls." PCI *Journal*, Vol.38, No. 3 (pp 72-73).

[15] Kurama, Y., (2001), "Simplified Seismic Design Approach for Friction-Damped Unbonded Post-Tensioned Precast Concrete Walls", Technical Paper, ACI *Structural Journal*. Vol. 98, No. 5, September-October 2001, pp 705-715.

[16] Priestley, M.J.N., Sritharan, S., Conley, J.R and Pampanin, S., (1999) "Preliminary Results and Conclusions From the PRESSS Five-Story Precast Concrete Test Building", PCI *Journal*, 44(6), 1999, pp 42-67.

[17] Mander, J. B., and Cheng, C.-T. (1997). "Seismic Resistance of Bridge Piers Based on Damage Avoidance Design", Technical Report NCEER-97-0014, Department of Civil, Structural and Environmental Engineering, State University of New York at Buffalo, New York.

[18] Holden, T. J., Restrepo, J., and Mander, J. B. (2003). "Seismic Performance of Precast Reinforced and Prestressed Concrete Walls." *Journal of Structural Engineering*, ASCE (March 2003), pp 286-296.

[19] Surdano, I. (2003). "Performance of Thin Precast Concrete Wall panels Under Dynamic Loading," Master Thesis, University of Canterbury, Christchurch, New Zealand.

[20] Ajrab, J. J., Pekcan, G. M., and Mander, J. B. (2004). "Rocking Wall - Frame Structures with Supplemental Tendon Systems." ACI Structural Journal, Vol.130, No.6 (June, 2004), pp 895-903.

[21] Liyanage, L.U. (2004). "Biaxial Lateral Loading Behaviour of Thin Concrete Walls," Master Thesis, Department of Civil Engineering, University of Canterbury, Christchurch, New Zealand.

[22] Hamid, N.H, (2006). "Seismic Damage Avoidance Design of Warehouse Buildings Constructed Using Precast Hollow Core Panels", PhD thesis submitted in partial fulfilment of the requirements for Department of Civil Engineering, University of Canterbury, Christchurch, New Zealand.

[23] Hamid, N.H., Mander, J.B., and Surdano, I., (2006), "Dynamic Overturning Capacity of rocking precast thin wall structures, ISSN 0126-513X, KDN PP5476/03/2006 (010726), IEM Journal, Vol. 67, No.3, September 2006.

[24] Hamid, N.H. and Linayage, L., and Mander, J.B., (2007), "Biaxial Behaviour of Thin Concrete Walls with monolithic emulation base connection", ISSN 0126-513X, KDN PP5476/03/2008 (010726), IEM Journal, Vol. 68, No.3, September 2007.

[25] Hamid, N.H. and Linayage, L. (2007), "Biaxial Behaviour of Thin Concrete Walls with Rocking Base Connections", ISSN 0126-513X, KDN PP5476/03/2008 (010726), IEM Journal, Vol. 68, No.4, December 2007, pp 7-16.

[26] Pekcan, G., Mander, J.B., and Chen, S. (1999) "Fundamental Considerations for the Design of Non-Linear Viscous Dampers", Earthquake Engineering and Structural Dynamics, N28, pp 1405-1425.

[27] Lin,Y.Y., and Chang, K.C.(2004). "Effects of site Classes on damping Reduction Factors", *Journal of Structural Engineering*, ASCE, Vol. 133, No.9, November 2004, pp 1667-1675.

[28] Martinez, M.Edgardo, (2002), "Performance-based Seismic Design and Probabilistic Assessment of Reinforced Concrete Moment Resisting Frame Structures", Master Thesis, Civil Engineering Department, University of Canterbury, Christchurch, New Zealand.

PROFILE

ENGR DR NOR HAYATI BINTI ABDUL HAMID
Dr Nor Hayati Abdul Hamid has been working as a lecturer at University Teknologi MARA, Shah Alam, Selangor for 16 years. She completed her PhD (Earthquake Engineering) from University of Canterbury, Christchurch, New Zealand in 2006. She received her Master of Science in Construction Management and Structural Engineering from University of NewCastle Upon Tyne, United Kingdom in 1993 and obtained her BSc (Civil Engineering) from University of Pittsburgh, United States of America in 1989. Her research interests are seismic performance of precast buildings under earthquake excitation, dynamic response of thin/slender wall, design of rocking precast hollow core walls under earthquake, cyclic behaviour of precast hollow core slabs, the interaction of beam-column joints under ground shaking, fragility curves and Incremental Dynamic Analysis.

KEUTUHAN PERMUKAAN AISI H13 KELULI TERKERAS DALAM PROSES PEMESINAN NYAHCAS ELEKTRIK (EDM)

(Date received: 19.2.2008)

Jaharah A. Ghani[1], Goh Geok Yong[2], Che Hassan Che Haron[3], Ahmad Rasdan Ismail[4], dan Baba Md. Deros[5]
Jabatan Kejuruteraan Mekanik and Bahan
Fakulti Kejuruteraan, Universiti Kebangsaan Malaysia, 43600 Bangi, Selangor.
Email: [1]jaharah@eng.ukm.my

ABSTRAK

Pemesinan nyahcas elektrik (EDM) ialah proses terma senyap yang menghasilkan beribu-ribu nyahcas elektrik dalam satu saat bagi menghakis keluar isipadu tertentu sesuatu logam. Proses ini digunakan secara meluas dalam situasi untuk memesin bentuk kompleks dan rumit bagi bahan yang sangat keras seperti keluli terkeras. Tetapi, proses ini menghasilkan sifat permukaan yang kurang memuaskan seperti tegangan tegasan baki yang tinggi, kekasaran permukaan yang tinggi, kewujudan retakan dan retakan mikro. Tujuan kajian ini dilakukan adalah untuk mengkaji kesan proses EDM ke atas keutuhan permukaan bagi keluli terkeras AISI H13 dengan menggunakan elektrod grafit dan kuprum. Kesan pelbagai parameter EDM ke atas keutuhan permukaan telah dikaji. Parameter EDM yand diambil kira ialah arus puncak (1, 2 dan 4 A), selang masa ON (3, 6 dan 12 µs), selang masa OFF (1, 2 dan 4 µs) dan jenis elektrod (grafit dan kuprum). Daripada topografi permukaan yang diperoleh, selang masa-ON, selang masa-OFF dan arus puncak yang semakin meningkat menyebabkan permukaan EDM menjadi semakin kasar iaitu lebih banyak puncak atau bucu yang terbentuk di permukaan EDM. Juga didapati proses EDM telah menyebabkan pembentukan tiga lapisan iaitu lapisan putih, lapisan sepuhlindap martensit dan lapisan bahan pukal. Keputusan ujian kekerasan mikro bagi elektrod grafit dan kuprum, mendapati kekerasan paling tinggi di lapisan putih iaitu 1130 Hv. Kekerasan bagi lapisan sepuhlindap adalah 543 Hv iaitu lebih rendah daripada lapisan pukal iaitu 550 Hv.

Kata Kunci: *AISI H13, Keutuhan Permukaan, Lapisan Putih, Pemesinan Nyahcas Elektrik (EDM)*

ABSTRACT

Electrical discharge machining (EDM) is a quite thermal process and produces thousands of electrical discharge in one second to remove certain volume of specific metal. This process is widely used in machining complex and intricate shapes for very hard metal such as harden steel. But this process will produce unsatisfactory finishing such as high tensile residual stress, coarser surface roughness, existence of crack and micro crack. The aim of this study is to investigate the effect of EDM process on the surface integrity of AISI H13 using graphite and copper electrodes. The effect of various EDM parameters on the surface integrity was studied. These parameters were peak current (1, 2 and 4 A), pulse-ON time (3, 6 and 12 µs), pulse-OFF time (1, 2 and 4 µs) and types of electrode (graphite and copper). It was found that the EDM process caused the formation of three layers namely white layer, quenched martensite layer, and bulk material layer. A maximum of 1130 HV was measured directly underneath the generated surface of white layer. The microhardness on the queched martensite was 543 HV, i.e. lower than the bulk material of 550 HV.

Keywords: *AISI H13, Electrical Discharge Machining, Surface Integrity, White Layer*

1.0 PENGENALAN

Secara umumnya, applikasi EDM tidak dipengaruhi oleh kekerasan dan kekuatan bahan. Dengan kata lain, proses EDM digunakan oleh semua bahan yang boleh mengkonduksikan elektrik. Satu daripada kebaikan proses EDM ialah proses ini tidak memerlukan persentuhan antara mata alat dan bahan kerja semasa pemesinan. Oleh itu, tiada deformasi berlaku walaupun bahan kerja adalah nipis. Disebabkan oleh proses ini melibatkan pemanasan dan penyejukkan yang sangat cepat, maka akan terbentuk satu lapisan kesan terma di atas permukaan bahan kerja. Struktur bagi lapisan ini agak berlainan daripada bahan asal. Walaupun ia sangat berguna dalam aspek meningkatkan rintangan terhadap kehausan dan kakisan, tetapi kewujudan seperti retakan mikro, lekukan serta tegasan baki boleh memburukkan lagi sifat mekanik bahan tersebut [1,2]. Kajian tentang keutuhan permukaan melibatkan perubahan yang berlaku bagi semua lapisan permukaan selepas proses pembuatan dan kesannya kepada sifat bahan tersebut serta kelakuannya apabila digunakan.

Kekasaran permukaan dipengaruhi oleh taburan lekukan yang wujud di permukaan yang disebabkan oleh percikan elektrik pada frekuensi tinggi [3]. Lapisan putih pula merujuk kepada lapisan yang sukar dipunar dan kelihatan putih di bawah mikroskop optik. Lapisan ini disebabkan oleh pemejalan semula bahan kerja ketika nyahcas dilakukan [2]. Sejurus selepas lapisan putih, terbentuk pula lapisan perantara, iaitu zon kesan haba iaitu haba yang tidak mencukupi untuk mencairkan logam tetapi cukup tinggi untuk mengubah struktur mikro bahan tersebut. Kawasan penyepuhlindapan yang memanas dan menyejuk lebih perlahan berbanding lapisan putih ini lebih lembut daripada bahan pukal. Seterusnya, lapisan bahan pukal iaitu struktur asal bahan keluli. Di lapisan ini, struktur dan sifat asal bahan kerja tidak berubah dan tidak dipengaruhi oleh proses EDM [4].

Kini, terdapat penyelidik-penyelidik yang cuba untuk mereka bentuk gabungan proses EDM dengan proses lain bagi meningkatkan produktiviti di samping dapat memperolehi keutuhan permukaan yang optimum. Contohnya Masuzawa *et al*. [5] mengabungkan operasi EDM dan pemesinan kimia elektrik (ECM) yang berusaha untuk memperbaiki kemasan permukaan dan mengurangkan kesan yang tidak diingini (*detrimental effect*) dalam proses EDM. Penyelidik lain pula, menjalankan pemesinan ultrasonik dan diikuti proses EDM. Objektif mereka hanya untuk membuangkan atau mengelakkan daripada lapisan putih terbentuk seterusnya dapat mengekalkan sifat asas bahan kerja yang diingini [5].

Keluli Terkeras AISI H13 merupakan aloi yang dikerja panas dan mempunyai rintangan terhadap haba tanpa perubahan sifat mekanik terutamanya pada suhu tinggi [6]. Gabungan pelbagai proses rawatan haba yang telah dijalankan menyebabkan keluli ini mempunyai ketegangan dan kekerasan yang tinggi, rintangan kehausan serta kelasakan terhadap daya impak dan sesuai untuk acuan dalam proses tempaan panas. Elektrod grafit digunakan kerana ia merupakan elektrod yang mempuyai rintangan kehausan yang paling tinggi dengan suhu leburnya mencecah sehingga 3000°C [12-13]. Manakala kuprum merupakan konduksi elektrik yang paling baik dan bahan yang stabil pada keadaan percikan. Jika dibandingkan dengan elektrod lain, elektrod kuprum mampu menghasilkan permukaan yang lebih halus [12-13].

Tujuan kajian ini dilakukan adalah untuk mengenalpasti lapisan-lapisan permukaan yang wujud pada bahan kerja Keluli Terkeras AISI H13 yang telah menjalani proses EDM dengan elektrod grafit dan kuprum.

2.0 KAEDAH EKSPERIMEN

Bahan kerja untuk ujikaji ini adalah keluli terkeras AISI H13(±53 HRC) yang telah menjalani proses EDM menggunakan mesin EDM Mitsubishi model M35J. Elektolit yang digunakan ialah parafin. Jadual 1 yang ditunjukkan di bawah merupakan sampel yang dipilih dengan parameter pemesinannya. Manakala Jadual 2 menunjukkan komposisi keluli terkeras AISI H13.

Jadual 1: Senarai sampel ujian dengan parameter pemesinan yang berlainan akan dikaji keutuhan permukaannya.

Bilangan Sampel	Arus Puncak I_p (A)	Selang Masa-ON T_i (μs)	Selang Masa-OFF T_o (μs)	Bahan Elektrod
1	1.0	3.0	1.0	Cu
2	1.0	6.0	2.0	C
3	1.0	12.0	4.0	Cu
4	2.0	3.0	2.0	Cu
5	2.0	6.0	4.0	Cu
6	2.0	12.0	1.0	C
7	3.0	3.0	4.0	C
8	3.0	6.0	1.0	Cu
9	3.0	12.0	2.0	Cu

Jadual 2: Komposisi Keluli Terkeras AISI H13

Elemen	Peratus (%)
Karbon	0.32 – 0.40
Silicon	1.00
Mangan	0.40
Kromium	5.13 – 5.24
Vanadium	1.00
Molibdenum	1.33 – 1.40

Bahan kerja keluli terkeras AISI H13 yang telah menjalani proses EDM diperhatikan topografi permukaan atasnya di bawah mikroskop konfocal Leica dalam bentuk 3-dimensi. Selepas itu, sampel dikerat secara melintang iaitu berserenjang dengan permukaan EDM dengan menggunakan mesin pemotong kepersisan Automatik Siri Minitom. Sampel metalografi disediakan dengan kaedah piawaian iaitu dari proses pencanaian, penggilapan dan akhirnya proses punar. Setelah selesai, sampel akan jelas kelihatan mikrostrukturnya di bawah pembesaran sehingga 100*x* oleh mikroskop optik. Sampel dicanai menggunakan kertas pasir bermula daripada saiz grid yang kasar sehingga saiz grid halus iaitu P320, P400, P600, P800, P1000 dan P1200. Penyejuk atau pelincir yang digunakan adalah air. Akhirnya, sampel akan dikaji kekerasannya dengan pengukur kekerasan Vickers model HMV-2000 merentasi kedalaman permukaan EDM. Kekerasan mikro diambil selang 3μ*m* daripada permukaan luar benda kerja sehingga 30μ*m* kedalamannya.

3.0 KEPUTUSAN DAN PERBINCANGAN

Topografi Permukaan

Keputusan ujikaji keutuhan permukaan keluli terkeras H13 dilihat dari segi topografi permukaan, mikrostuktur dan kekerasan mikro merentasi benda kerja yang telah menjalani proses EDM dengan parameter pemesinan yang berbeza-beza dari segi elektrod, arus puncak (*Ip*), selang masa-ON (*Ti*) dan selang masa-OFF (*To*).

Rajah 1-3 menunjukkan contoh morfologi bagi permukaan yang telah menjalani proses nyahcas elektrik (EDM). Semasa proses EDM, terdapat banyak haba yang dijanakan, menyebabkan permukaan benda kerja mula cair dan mengewap. Dielektrik seterusnya akan mengalir keluar serpihan cecair ini dan pada masa yang sama permukaan benda kerja disejukkan dengan cepat. Kadar pemanasan dan penyejukkan yang tinggi ini menyebabkan kesan EDM terhadap struktur bahan kerja seperti kewujudan lekukan, kelompok logam, retakan, serpihan logam yang memejal semula dan juga mempunyai lompang [1, 6].

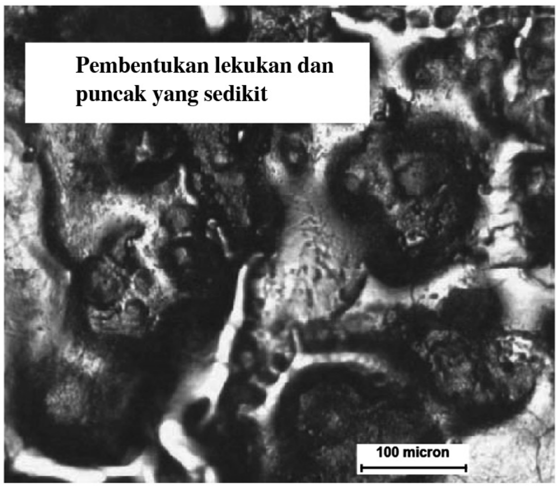

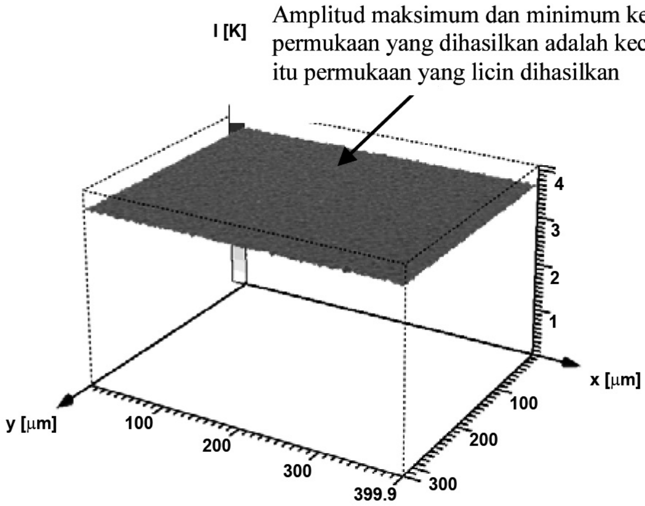

Rajah 1 : Tekstur permukaan keluli terkeras H13 bagi proses EDM yang menggunakan elektrod kuprum dan keadaan pemotongan, Ip = 1A, T_i = 3μs, T_o = 1μs

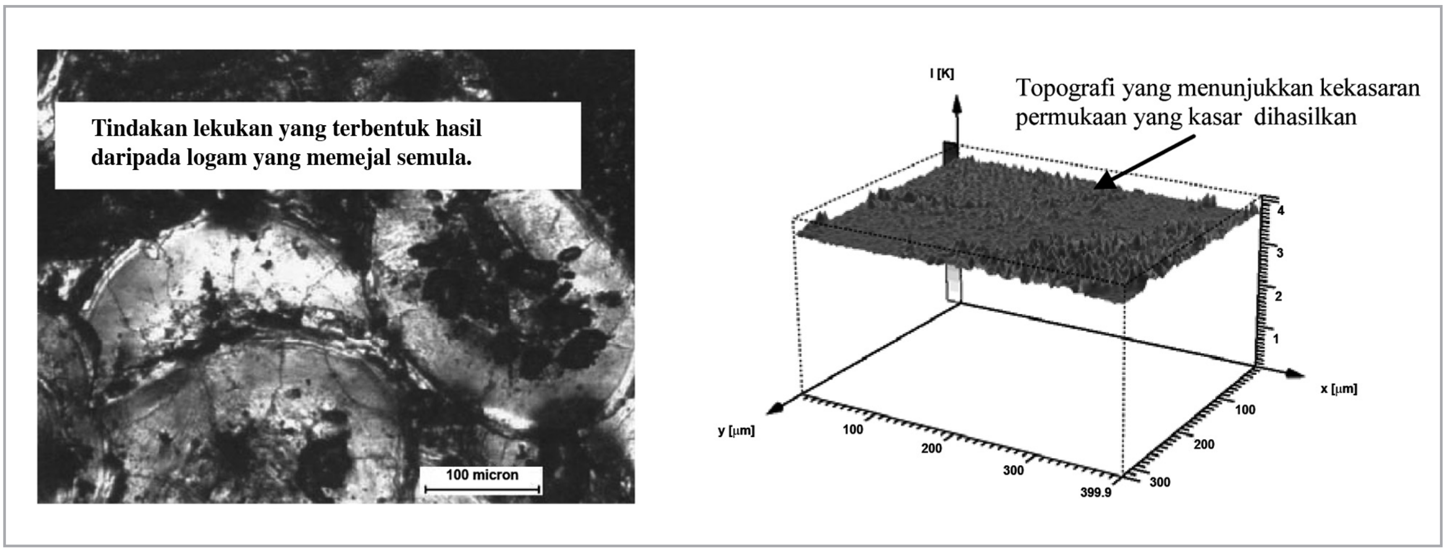

Rajah 2 Topografi permukaan keluli terkeras H13 bagi proses EDM yang menggunakan elektrod grafit dan keadaan pemotongan, Ip = 1A, T_i = 6µs, T_o = 2µs

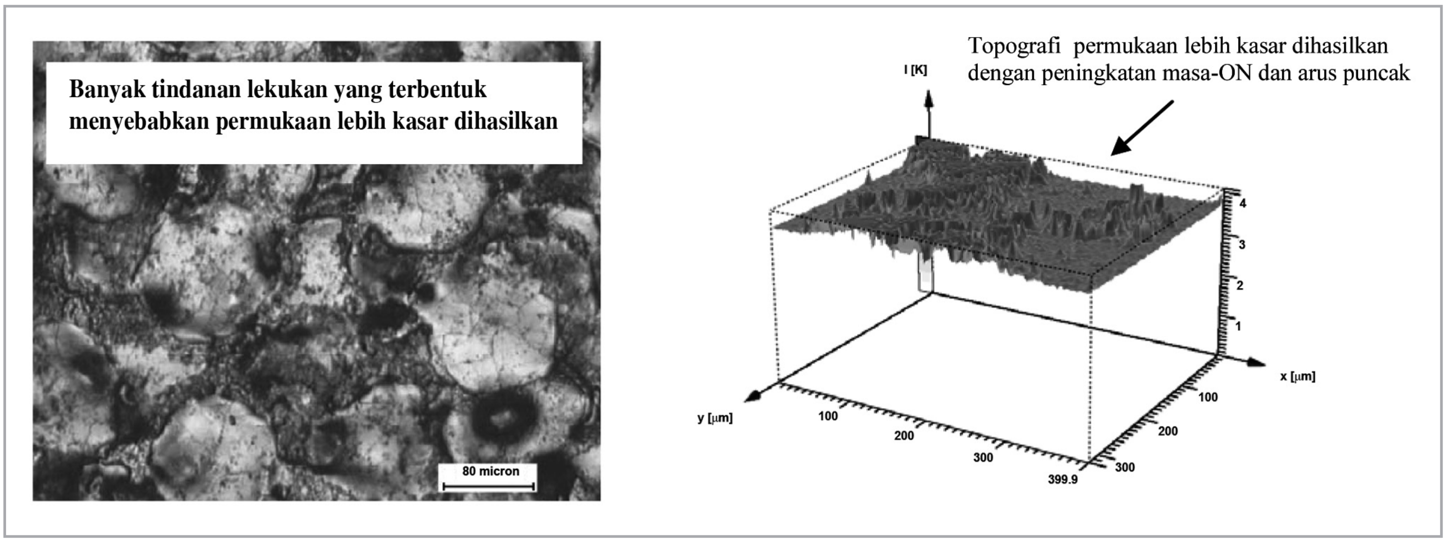

Rajah 3 : Topografi permukaan keluli terkeras H13 bagi proses EDM yang menggunakan elektrod grafit dan keadaan pemotongan, Ip = 2A, T_i = 12µs, T_o = 1µs

Topografi permukaan menunjukkan tekstur permukaan yang terdiri daripada di atas permukaan kerja. Topografi bagi setiap sampel yang telah menjalani proses *EDM* dengan menggunakan mikroskop konfokal bertujuan untuk melihat kesan parameter pemesinan iaitu arus puncak, selang masa-ON, selang masa-OFF dan bahan elektrod, terhadap permukaan keluli terkeras H13 yang terbentuk.

Topografi Rajah 1-3 menunjukkan topografi apabila arus puncak ditetapkan pada 1*A* dan 2*A*, selang masa-ON yang semakin meningkat iaitu daripada 3µ*s*, 6µ*s* dan 12µ*s* serta selang masa-OFF yang semakin meningkat iaitu 1µ*s*, dan 2µ*s*. Permukaan bahan kerja yang diperolehi semakin merosot iaitu kewujudan lekukan dan puncak yang semakin banyak.

Seterusnya kekasaran permukaan bahan kerja menjadi semakin kasar. Ini disebabkan oleh pertambahan selang masa-ON akan menyebabkan lebih banyak bahan kerja dileburkan dan juga peningkatan arus puncak seperti dalam Rajah 3. Sekiranya bahan kerja yang dileburkan ini tidak dialir keluar oleh dielektrik, maka ia akan memejal semula dan membentuk lapisan putih di atas permukaan benda kerja. Kesan lapisan putih meningkatkan kekasaran permukaan benda kerja. Kajian yang dijalankan oleh Puertas *et al* [7] menunjukkan arus puncak ialah faktor ketara yang mengawal nilai kekasaran permukaan. Kerja –kerja yang dilakukan oleh Guu *et al* [8] dan, Lee dan Tai [1] juga menunjukkan keputusan yang sama. Mereka mendapati dengan menaikkan arus puncak dan selang masa-ON akan menyebabkan kemerosotan kekemasan permukaan. Tambahan pula selang masa-ON yang panjang akan membenarkan lebih haba dikeluarkan daripada permukaan elektrod [9].

Secara keseluruhan, untuk memperoleh permukaan yang kemas. Gabungan arus puncak yang rendah, selang masa-ON yang pendek, dan selang masa-OFF yang pendek digunakan. Arus puncak yang rendah memberikan jumlah tenaga yang dibebaskan adalah rendah. Selang masa-ON yang pendek pula dapat mengurangkan pembentukkan lekukan dan kawah yang terbentuk dengan kadar pembuangan yang rendah. Akhirnya, selang masa-

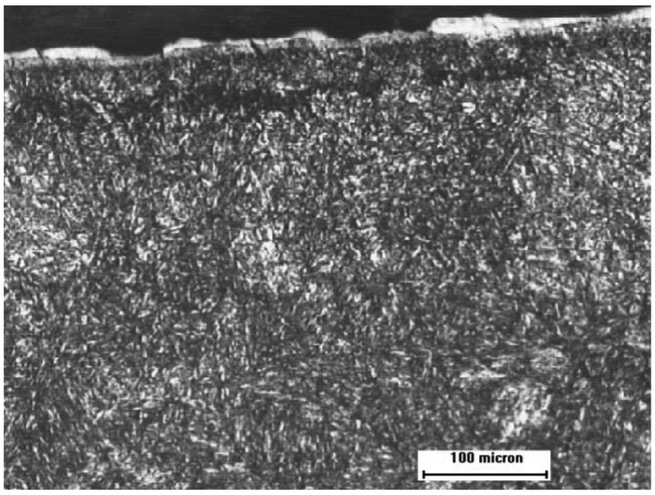

Rajah 5: Mikrostruktur permukaan keluli terkeras H13 bagi proses EDM yang menggunakan elektrod kuprum dan keadaan pemotongan, $I_p = 1A$, $T_i = 6\mu s$, $To = 2\mu s$

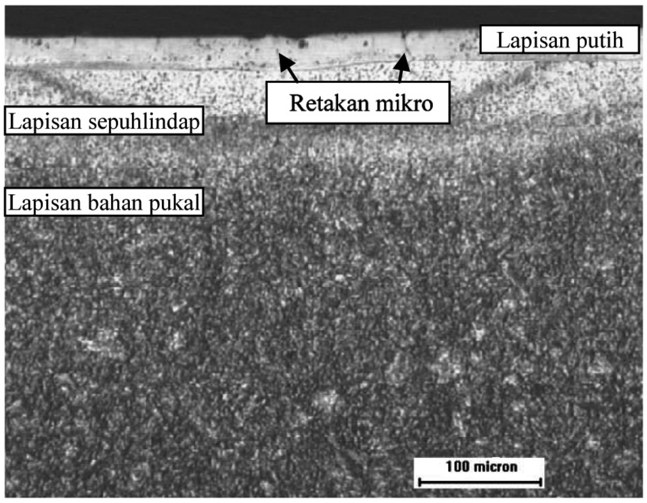

Rajah 6: Mikrostruktur permukaan keluli terkeras H13 bagi proses EDM yang menggunakan elektrod grafit dan keadaan pemotongan, $I_p = 1A$, $T_i = 6\mu s$, $T_o = 2\mu s$

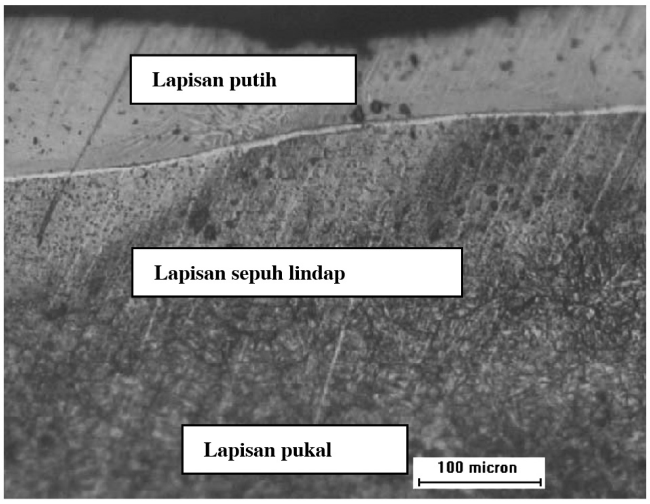

Rajah 7: Mikrostruktur permukaan keluli terkeras H13 bagi proses EDM yang menggunakan elektrod kuprum dan keadaan pemotongan, $I_p = 4A$, $T_i = 12\mu s$, $To = 2\mu s$

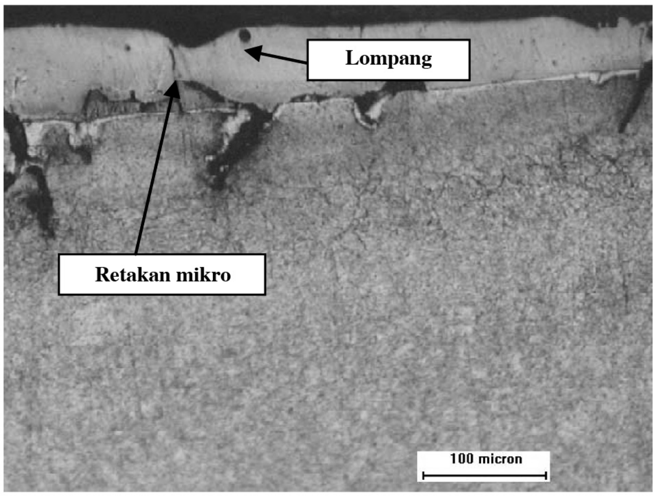

Rajah 8: Kewujudan retakan mikro dan lompang di lapisan keluli terkeras H13 bagi proses EDM yang menggunakan elektrod kuprum dan keadaan pemotongan, $I_p = 4A$, $T_i = 12\mu s$, $To = 2\mu s$

OFF yang pendek digunakan tetapi perlu mengelakkan daripada menggunakan masa-OFF yang terlalu singkat. Selang masa-OFF semakin pendek, semakin cepat proses pembuangan logam.

Perubahan Mikrostruktur di Bawah Permukaan yang di Mesin

Semua sampel yang dimesin dengan proses *EDM* mempunyai lapisan putih di atas permukaannya. Terdapat tiga lapisan yang terbentuk di bawah permukaan *EDM* iaitu lapisan putih, lapisan sepuhlindap dan lapisan bahan pukal. Rajah 5-6 menunjukkan mikrostruktur bagi sampel metalografi keluli terkeras H13 yang diperhatikan di bawah mikroskop optik. Terdapat lapisan putih yang wujud di atas permukaan setiap sampel tersebut. Ketebalan bagi lapisan ini adalah berbeza-beza bagi parameter proses *EDM* yang berlainan. Lapisan putih, dalam fasa dendrit berada pada permukaan benda kerja. Pembentukan lapisan putih disebabkan oleh pemejalan semula leburan logam yang tidak dialir keluar oleh dielektrik ketika penyejukkan. Lapisan ini terdiri daripada martensit dan austenit yang dikekalkan serta mengandungi karbon yang diresap ketika nyahcas elektrik [1]. Disebabkan oleh resapan karbon dan struktur yang berlainan daripada bahan pukal, kekerasan lapisan ini adalah jauh lebih tinggi daripada bahan pukal.

Secara keseluruhan, semakin tinggi selang masa-ON, semakin tebal lapisan putih yang terbentuk [1]. Seperti yang ditunjukkan dalam Rajah 5 dan 6, di mana arus puncak dikekalkan pada 1*A*, selang masa-ON dinaikan daripada 3μs, kepada 6μs. Selang masa-ON yang semakin meningkat, menyebabkan masa untuk meleburkan logam semakin bertambah walaupun menggunakan elektrod yang berbeza. Dengan kadar pengaliran dielektrik yang malar, lebih banyak logam tidak dapat disingkirkan. Maka ia akan disejukkan oleh dielektrik dan memejal semula di atas permukaan benda kerja. Terdapat banyak retakan mikro yang wujud di lapisan putih seperti yang ditunjukkan dalam Rajah 6.

Ini sejajar dengan kajian yang dilakukan oleh Lee and Tai [1]. Mereka mengatakan bahawa retakan yang wujud di lapisan putih jarang merentasi lapisan sepuhlindap kecuali tenaga puncak (*pulse energy*) yang cukup tinggi. Kandungan karbon yang tinggi dalam bahan kerja juga memberi kesan kepada pembentukkan retakan mikro [6]. Lapisan ini terdiri daripada martensit dan austenit yang dikekalkan serta mengandungi karbon yang diresap ketika nyahcas elektrik [1]. Disebabkan oleh resapan karbon dan struktur yang berlainan daripada bahan pukal, kekerasan lapisan ini adalah jauh lebih tinggi daripada bahan pukal.

Menurut Ghanem et al [10], lapisan sepuhlindap dipengaruhi oleh jenis, tahap pengerasan keluli serta parameter pemesinan. Secara umumnya, ketebalan lapisan sepuhlindap semakin meningkat apabila nyahcas elektrik semakin meningkat iaitu semakin banyak haba dikenakan pada zarah di bawah permukaan benda kerja.

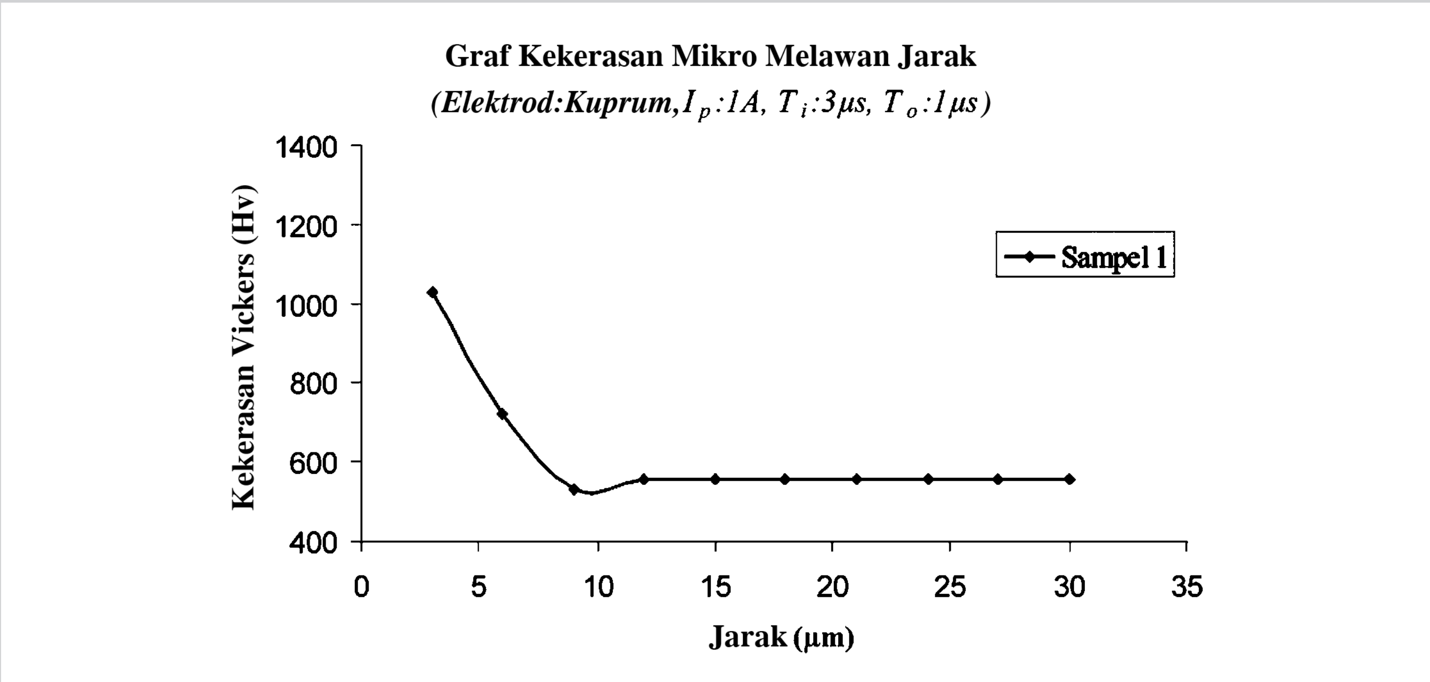

Rajah 9: Graf kekerasan mikro melawan jarak, keluli terkeras H13 bagi proses EDM yang menggunakan elektrod kuprum dan keadaan pemotongan, I_p = 1A, T_i = 6μs, T_o = 2μs

Akhirnya, kehadiran lapisan putih dan sepuhlindap mempengaruhi sifat mekanikal benda kerja. Sebagai contoh, retakan pada permukaan boleh menyebabkan bahan tersebut gagal sebelum takat alahnya.

Ujian Kekerasan Mikro Vikers

Kekerasan mikro untuk setiap sampel keluli terkeras H13 diuji dengan menggunakan alat pengukur kekerasan Vickers. Beban sebanyak 200*g* dikenakan pada permukaan sampel selama 10saat bermula dari jarak di atas permukaan luar lapisan putih sehingga ke bahan pukal iaitu lebih kurang daripada permukaan yang dimesin. Rajah 9 menunjukkan contoh graf kekerasan mikro melawan jarak daripada permukaan yang dimesin.

Daripada graf yang diperolehi, didapati bahawa lapisan luar untuk setiap sampel adalah lebih keras berbanding bahan pukal. Kekerasan yang tinggi ini disebabkan oleh kewujudan lapisan putih di permukaan benda kerja. Ketebalan lapisan putih bergantung kepada parameter pemesinan yang digunakan. Semakin tinggi selang masa-ON, semakin tebal lapisan putih yang terbentuk. Begitu juga dengan kenaikan arus puncak yang menambahkan ketebalan lapisan putih.

Sejurus selepas lapisan putih, terdapat kekerasan yang lebih rendah daripada bahan pukal. Ini disebabkan oleh lapisan sepuhlindap terbentuk yang mana mikrostruktur benda kerja dikenakan haba di bawah takat lebur semasa nyahcas elektrik terbentuk. Tambahan pula lapisan ini disejukkan dengan perlahan oleh dielektrik proses *EDM*. Maka kekerasan di lapisan ini adalah lebih rendah berbanding bahan pukal. Keputusan yang sama juga diperoleh oleh penyelidik Ahmet and Ulas [6] iaitu kekerasan yang paling tinggi di lapisan putih diikuti kekerasan yang lebih rendah daripada bahan pukal di lapisan sepuhlindap dan seterusnya lapisan bahan pukal.

Secara keseluruhan, kekerasan keluli terkeras H13 yang dijalani proses *EDM* mempunyai kekerasan yang paling tinggi di permukaan luar benda kerja iaitu sebanyak 1130 Hv, diikuti dengan penurunan kekerasan mikro pada lapisan pertengahan iaitu 543 Hv dan seterusnya kekerasan bahan pukal di sekitar 550 Hv. Keputusan yang diperolehi adalah untuk kedua-dua jenis elektrod yang digunakan. Penyelidik lain juga mendapati kekerasan benda kerja berubah merentasi kedalaman benda kerja. Lapisan putih menunjukkan kekerasan dua kali ganda jauh lebih besar daripada bahan pukal, manakala lapisan sepuhlindap mempunyai kekerasan yang lebih rendah daripada bahan pukal [1].

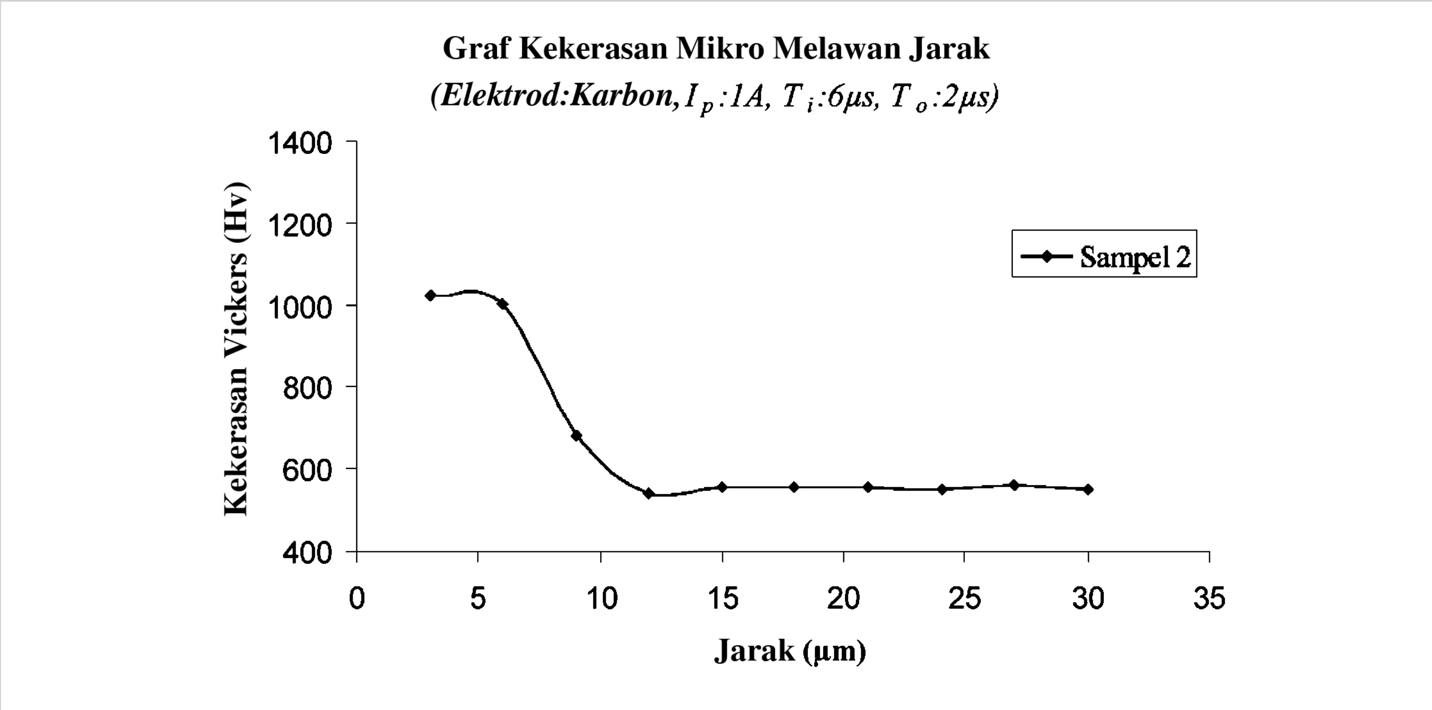

Rajah 10 : Graf kekerasan mikro melawan jarak, keluli terkeras H13 bagi proses EDM yang menggunakan elektrod grafit dan keadaan pemotongan, I_p = 1A, T_i = 6µs, T_o = 2µs

4.0 KESIMPULAN

Kesimpulan yang boleh dibuat berdasarkan ujikaji yang dijalankan adalah seperti berikut:

1. Daripada topografi permukaan yang diperoleh, selang masa-ON, selang masa-OFF dan arus puncak yang semakin meningkat boleh menyebabkan permukaan *EDM* menjadi semakin kasar iaitu lebih banyak puncak atau bucu yang terbentuk di permukaan *EDM*.

2. Ketebalan lapisan putih bergantung kepada parameter pemesinan. Semakin tinggi selang masa-ON dan arus puncak, semakin tebal lapisan putih yang terbentuk. Tetapi pengaruh arus puncak terhadap ketebalan lapisan putih yang terbentuk adalah tidak ketara kerana arus puncak yang kecil digunakan.

3. Kekerasan keluli terkeras H13 yang dijalani proses *EDM* mempunyai kekerasan yang paling tinggi di permukaan luar benda kerja atau lapisan putih iaitu sekitar 1130 Hv, diikuti dengan penurunan kekerasan mikro pada lapisan pertengahan atau lapisan sepuhlindap iaitu 543 Hv dan seterusnya kekerasan lapisan bahan pukal di sekitar 550 Hv. ■

RUJUKAN

[1] Lee, H.T., Tai, T.Y. 2003. Relationship between EDM parameter and surface crack formation. *Journal of Materials Processing Technology* 142: pp. 676-683.

[2] Lee, Hwa-Teng, Hsu, Fu-Chuan, Tai, Tzu-Yao. 2004. Study of surface integrity using the small area EDM process with a copper-tungsten electrode. *Materials Science and Engineering* A364: pp. 346-356.

[3] Yusuf Keskin, Selcuk Halkaci, H.,Mevlut Kizil. 2006. An experimental study for determination of the effects of machining parameters on surface roughness in electrical discharge machining (EDM). *Journal of Materials Processing Technology* 28: pp. 1118-1121.

[4] Masuzawa T. Sakai S., and Ito S., ECM finishing of surface products by EDM. Proceedings of ISEM9, 1989, pp. 155–158.

[5] Ramasawmy, H. and Blunt, L. 2004. Effect of EDM process parameters on 3D surface topography. *Journal of Materials Processing Technology* 148: pp. 155-164.

[6] Ahmet Hascalyk and Ulas Caydas. 2004. Experiment study of wire electrical discharge machining of AISI D5 tool steel. *Journal of Materials Processing Technology* 148: pp. 362-367.

[7] Puertas, I., Luis, C.J. and Alvarez, L. 2004, Analysis of the Influence of EDM parameters on Surface Quality, MRR and ER of WC-Co. *Journal of Material Processing Technology* 153-154: pp. 1026-1032

[8] Guu, Y.H., Hocheng, H., Chou, C.Y., Deng, S.C., 2003. Effect of EDM on Surface Characteristics and Machining Damage of AISI D2 Tool Steel. Material Science and Engineering A358: pp. 37-43.

[9] Wong. C.C., Yan. B. H. 2000. Blind hole drilling of / 6061 Al composites using rotary EDM. *Journal of Materials Processing Technology* 90-102.

[10] Ghanem, F., Braham, C., Sidhom, H. 2003. Influence of steel type on electrical discharge machined surface integrity. *Journal of Materials Processing Technology* 142: pp. 163-173.

[11] Tanpa pengarang. H13 tool steel material information (atas talian). http://www.windsorsteel.com/grades/h-13.htm (22 September 2006).

[12] Kalpakjian, S. and Schmid, S. R. 2001. Manufacturing Engineering and Technology. Ed ke-4. United States of America: Prentice Hall International.

[13] McGeough, J. A. 1988. Advanced Methods of Machining. Ed. Ke-2. Prentice Hall International, Inc.

PROFILES

JAHARAH A. GHANI
A.G. Jaharah is a BEng and an MSc in Manufacturing Engineering from Leeds Metro University and Warwick University, UK, respectively. She received a PhD in Manufacturing Engineering from Universiti Malaya, Malaysia. Her current research interests are machining technology of tool steels, cast iron and aerospace materials.

ENGR. AHMAD RASDAN ISMAIL
Engr. Ahmad Rasdan Ismail is a professional engineer registered with the Board of Engineers Malaysia BEM, and holds a BEng. (Hons) (UKM), as well as a Masters of Science in Manufacturing Systems Engineering (UPM). He has been working in the engineering field including as a design engineer at R&D PROTON and also as a consultant for many projects under UKM. Ahmad Rasdan is currently a lecturer in manufacturing engineering at the UKM.

ENGR. HAJI BABA MD DEROS
Engr. Haji Baba Md Deros is a graduate member of IEM and holds BSc (Hons) in Mechanical Engineering from University of Glamorgan, United Kingdom, Master of Science in Manufacturing Systems Engineering from University of Warwick, United Kingdom and PhD in Manufacturing Management. He has been working as a lecturer in several Polytechnics and currently as an Associate Professor in the Department of Mechanical and Materials Engineering, Faculty of Engineering, UKM.

EFFECT OF INTERPHASE FORCES ON TWO-PHASE LIQUID: LIQUID FLOW IN HORIZONTAL PIPE

(Date received: 19.7.2007)

Rashimi, W., Choong, T. S. Y*., Chuah, T. G., Hussain, S. A. and Khalid, M.
Department of Chemical and Environmental Engineering Faculty of Engineering,
Universiti Putra Malaysia 43400 UPM Serdang Selangor
*E-mail: *tsyc2@yahoo.com.uk*

ABSTRACT

A two-fluid model (Eulerian-Elurian model) is used to simulate dispersed two-phase immiscible liquids (oil-water) in a horizontal pipe. Effect of interphase forces (drag, lift and turbulent dispersion) is discussed. In the present study water is considered as dispersed and oil as continuous phase. The exchange between the phases is represented using source terms in conservation equations. Standard k-e turbulence model is used to induce turbulence in continuous phase. Comparison between mathematical simulation using CFD code FLUENT 6.2 and experimental data indicates that the interphase forces are important and has a strong effect on flow behaviour. Different drag, lift and turbulent dispersion expressions are evaluated. The CFD simulations are in good agreement with published experimental data.

Keywords: *CFD, Dispersed Flow, Horizontal Pipe, Interphase Forces, Oil-water System, Two-phase Flow*

1.0 INTRODUCTION

Liquid-liquid dispersions comprising of drops of one fluid dispersed into other are extensively encountered in many of the chemical and process industries. An oil-water mixture flow patterns are unique and also complex due to its complicated rheological behaviour.

A quantitative and qualitative understanding of the flow hydrodynamics, turbulence and dispersion phenomena is necessary for optimal design and efficient operations of equipment in handling such liquid dispersions. Heat and mass transfer rates are also affected by dispersed entities

that feature varying shapes and size. Mass transfer rates are greatly enhanced if the interfacial contact area of the dispersed phase is increased.

Extensive numerical modelling of gas-liquid flow have been carried out and reported such as turbulence phenomena, fluid flow, mixing phenomena for flow in vertical pipe. However, the knowledge of gas-liquid flows cannot be readily applied for liquid-liquid flows due to large density difference in the gas-liquid flows. Further, for liquid-liquid flow in horizontal pipe, there is a difference in flow regime due to gravity.

It is well known that the interfacial forces existing at the interphase of liquid-liquid phases are responsible for mass and momentum exchange between the two phases. There are many drag expressions proposed to account for the effect of drag on fluid flow such as drag on rigid sphere [1], drag on single drop [2] and drag in the presence of adjacent drops [3]. To study the effect of lift force simulations have been carried out using several constant values for lift coefficient. Turbulent dispersion force is studied by varying the value of dispersion Prandtl number (DPN) in the simulation.

In the present paper, based on the two-fluid model (E-E), the three-dimensional fluid flow of oil-water system is simulated and the effect of interphase forces on the fluid flow in specially discussed. The simulations are carried out in a cylindrical horizontal pipe of 1.0 inch ID (internal diameter) for mixture velocity of 2.12 m/s and 46% input water. The experimental results of Soleimani [4] are used to make a comparison with the simulation.

2.0 MATHEMATICAL FORMULATION

The E-E model is based on interpenetrating continuum assumption. Here, all phases share the domain and interpenetrate as they move through it. Each phase is characterised by distinct fields of velocity and volume fraction. The governing equations are solved for each phase, considering the time averaged values. The governing equations proposed by Ishii [5] are more commonly used in fluid-fluid flows. The exchange between the phases is represented by source terms in conservation equations. The phases are assumed to share space in proportion to their volume fractions so as to satisfy the total continuity relation, *i.e*.

$$\alpha_d + \alpha_c = 1.0 \tag{1}$$

Turbulence is assumed to be a property of continuous liquid phase. The dispersion of the phases due to turbulence is represented by introducing a diffusion term in the mass conservation equation.

In the present study dispersed phase drops are assumed to be of uniform size throughout. The sauter mean diameter (SMD) of the dispersed drops is calculated using correlation proposed by Angeli [6] Drop break-up and coalescence is not taken into account, *i.e*. drop-drop interactions are assumed to be negligible.

turbulence model is applied to describe the behaviour of the liquid phase. There is no thermal interaction and the flow is essentially Newtonian, incompressible and unsteady.

2.1 Governing Equations

Within the framework of the above assumptions, the governing equations may be written in the following forms:

2.1.1 *Continuity Equation (mass conservation equation)*

For any phase q, the mass conservation equation can be written as:

$$\nabla.(\alpha_q \rho_q U_q - D\nabla\alpha_q) = 0 \tag{2}$$

where the second term represents the phases diffusion term which accounts for the dispersion of the dispersed drops in continuous phase. The diffusion or dispersion coefficient is associated with the random motion associated with the phases.

2.1.2 *Conservation of Momentum*

The momentum conservation equation can be written as:

$$\nabla.\left[\underbrace{\alpha_q \rho_q U_q U_q}_{convection} - \underbrace{\alpha_q \Gamma_q U_q}_{diffusion}\right] = \underbrace{S_q + S^*_q}_{Source} \tag{3}$$

where is an exchange coefficient representing the effects of turbulent diffusion within the phases. The effective viscosity is given as:

$$\mu_{eff} = \mu_t + \mu_c \tag{4}$$

where the turbulent viscosity is given by

$$\mu_t = C\mu\rho_c k^2/\varepsilon \tag{5}$$

Turbulence in continuous phase is modeled in the same way as that of single phase flow using Equation (6) with transport equations for k and ε:

$$\frac{\partial}{\partial t}(\alpha_q \rho_q \varphi_q) + \nabla.(\alpha_q \rho_q \bar{U}_q \varphi_q) = \nabla.\left[\alpha_q \frac{\mu_{t,q}}{\partial_{pr_\varphi}} \nabla\varphi_q\right] + S_{\varphi q} \tag{6}$$

The term in Equation (6) is further expanded as follows:

$$S_{kq} = \alpha_q G_{k,q} - \alpha_q \rho_q \varepsilon_q + \alpha_q \rho_q \prod k_q \tag{7}$$

$$S_{\varepsilon q} = \alpha_q \frac{\varepsilon_q}{k_q}[C_{1\varepsilon} G_{k,q} - C_{2\varepsilon}\rho_q \varepsilon_q] + \alpha_q \rho_q \prod k_q \tag{8}$$

where $G_{k,q}$ is the generation of turbulent kinetic energy due to mean velocity gradient in phase $_q$, which is again calculated as:

$$G_k = \mu_{eff} \frac{\partial U_i}{\partial x_i}\left[\frac{\partial U_i}{\partial x_j} + \frac{\partial U_j}{\partial x_i}\right] \tag{9}$$

2.2 Interfacial Forces F_i

The drag expression for single rigid sphere is generally expressed by the correlation proposed by Schiller and Naumann [1]:

$$C_{D0} = \begin{cases} 24(1 + 0.15\mathrm{Re}^{0.687})/\mathrm{Re} & \mathrm{Re} \leq 1000 \\ 0.44 & \mathrm{Re} \leq 1000 \end{cases} \tag{10}$$

However, a liquid drop in another liquid medium does not behave like a rigid sphere [7]. Expressions to account for drag on a single drop have been proposed by many researchers [2, 8-10]. The general expression for drag on a single drop is given by Equation (11).

$$F_D = \frac{1}{8}\pi d^2 C_{D0} \rho_c V_s^2 \tag{11}$$

However, drops moving in the presence of adjacent drops experiences more drag because its motion is now impeded by other drops. The drag on drops moving with adjacent drops is given by Equation (12):

$$F_D = \frac{3}{4}\frac{C_{DM}\alpha_d \rho_c V_s^2}{d} \tag{12}$$

The new drag coefficient C_{DM} in Equation (12) accounts for reduced buoyancy and increased drag due to the presence of other drops. The expressions proposed for drag force which takes into account the presence of adjacent drops [2, 3, 11] are listed in Table 1.

Table 1: Drag expressions on drops which take into account the presence of adjacent drops [7]

Investigator (s)	*Proposed expression for drag coefficient (C_{DM}) in the presence of adjacent drops*
Hu and Kinter [8]	$\mu_m = \mu_c(1-\alpha_d)^{-2.5(\mu_d+0.4\mu_c)/(\mu_d+\mu_c)}$ and $Re_m = \frac{d_e V_s \rho_c}{\mu_m}$ $C_{DM} = \frac{24}{Re_m}$ } *Stokes regime* $C_{DM} = \frac{24}{Re_m}(1+0.1Re_m^{0.75})$ } *Undistorted particle regime* $f(\alpha_d) = \sqrt{1-\alpha_d}\,(\frac{\mu_c}{\mu_m})$ and $E(\alpha) = \left\{\frac{1+17.67[f(\alpha_d)]^{6/7}}{18.67 f(\alpha_d)}\right\}^2$ $C_{DM} = 0.45\,E(\alpha)$ } *Newton's regime* $C_{DM} = \frac{2}{3}\,Eo\,(E(\alpha))$ } *Distorted particle regime* $C_{DM} = \frac{8}{3}(1-\alpha_d)^2$ } *Chun turbulent flow regime*
Kumar and Hartland [3]	$C_{DM} = \left[0.53 + \frac{24}{Re}\right](1+4.56\alpha_d^{0.73})$
Rusche and Issa [11]	$C_{DM} = C_{D0} f(\alpha)$ *where* $f(\alpha) = exp(2.10\alpha_d) + \alpha_d^{0.249}$

The expression for slip (relative) velocity is given by:

$$V_S = \frac{4gd_e\Delta\rho(1-\alpha_d)}{3\rho_c C_{DM}} \tag{13}$$

Lift force in two-phase flows is primarily responsible for non-uniform radial distribution of the dispersed phase hold-up particularly in turbulent flows. Wall peaking, near wall peaking and coring profiles were experimentally observed in the experimental studies [4, 12]. The lift force used in CFD model assumes the following form, where the volume of the sphere is replaced by volume of the dispersed phase (α_d) since, the size and shape of the drops is assumed to be constant and non deformable.

$$\bar{F}_{lift} = -C_L\rho_q\alpha_d(\bar{v}_q - \bar{v}_p) \times (\nabla \times \bar{v}_q) \tag{14}$$

where C_L is referred to as lift coefficient in Equation (14). Lift coefficient is a single value which can be either positive or negative. It does not change with the local hydrodynamic condition or flow properties. There are no values of lift coefficients reported for dispersed liquid-liquid flows. Thus, in the present study simulations have been carried out using both positive and negative values (*i.e.* 0, -0.05, 0.5 and 1.0) based on the studies of Madhavan [7].

In turbulent flows, the dispersed entities are transported by turbulent eddies from region of high concentration to low concentration in the continuous phase which is termed as turbulent dispersion. It is strongly influenced by the fluctuating velocity field of the continuous phase which counteracts the lift force and homogenizes the flow in the domain. At high mixture velocity it was observed that the oil drops tend to move towards the core of the pipe due to the combined effect of inviscid lift and turbulent dispersion forces [4,12]. The drops tended to move to the core of the pipe in the region of low turbulence as turbulent dispersion is stronger near the wall. It was also reported that drops near the core region had the same diffusivity as of continuous phase. In the present study Simonin and Viollet [13,14] model is adopted, which uses the DPN to signify the turbulence dispersion.

2.3 Boundary Conditions

Figure 1 shows the computational domain used in this present study. It shows the hexahedral mesh with approximately 160,000 cells and the boundary conditions defined.

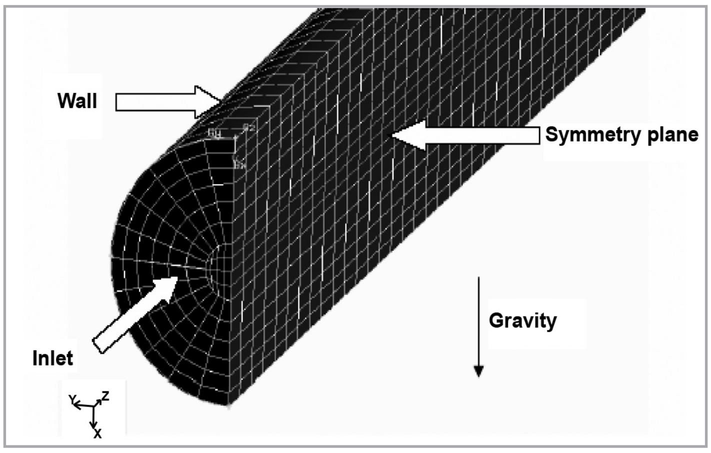

Figure 1: Computational domain showing boundary conditions

2.3.1 Inlet Conditions

Uniform inlet velocity is considered at the pipe inlet. Velocity of both the phases and volume fraction of the dispersed phase is given at the inlet.

$$U_x = 0 \qquad U_y = 0 \qquad U_z = 1 \tag{15}$$

Turbulence intensity (I) is calculated as:

$$I = 0.16(R_e)^{-1/8} \tag{16}$$

The turbulence parameters at the inlet are calculated as:

$$k = \frac{3}{2}\left[\frac{U_c}{\alpha_c} I\right] \text{ and } \varepsilon = C_\mu^{3/4}\frac{k^{3/2}}{l} \tag{17}$$

where l is the turbulent length scale. For fully developed flows $l = 0.07D$, where D is the pipe diameter.

2.3.2 Outlet Conditions

At the outlet of the pipe pressure outlet boundary condition is implemented. Atmospheric pressure is specified.

2.3.3 Wall Conditions

Wall boundary condition was used to bind the fluid and the solid region. '*No-slip*' boundary condition was imposed at the wall.

$$U_x = 0 \qquad U_y = 0 \qquad U_z = 0 \tag{18}$$

However, to determine the solution of the governing equations at the solid wall, where steep gradients in the flow variables occur, a log law wall function is employed to simulate the turbulence behaviour near the wall.

The whole computational domain is divided into viscosity affected region and fully turbulent region based on turbulence Reynolds number, Re_y, defined as:

$$\text{Rey} = \frac{\rho_c y_w \sqrt{k_c}}{\alpha_c} \tag{19}$$

where y_w is the normal distance from the wall. Standard wall functions, Y+ values in the range of 30-60 (closer to lower bound) are used. The Y+ value of 35 is used to calculate the first grid point from the wall. In viscosity affected region near the wall where turbulent Reynolds number (Re_y) is less than 200, about 8-12 cells of fine spacing are used to resolve the mean velocities and turbulent parameters.

2.3.4 Symmetry Conditions

The turbulent liquid-liquid flows are considered to be symmetric about the center plane. *Symmetry* boundary condition is used to reduce the computational cells to half thus reducing the computational time.

3.0 RESULTS AND DISCUSSION

A finite volume method CFD code FLUENT is employed to solve the governing equations numerically. The computational domain consists of approximately 160,000 hexagonal cells.

In the present study, the mathematical simulations are carried out for the following four cases:

(i) Case I: only effect of different drag force is taken into account as the interphase force to study the phase distribution.

(ii) Case II: using drag expression of case I, effect of lift coefficient is studied using range of positive and negative values.

(iii) Case III: effect of individual forces is studied on phase distribution.

3.1 Case I

Figure 2 shows the comparison of different drag models proposed in literature: drag on rigid sphere [1], drag on single drop [8], drag on single drop in dense dispersion [11] and drag on a single drop in the presence of adjacent drops [3].

The simulations are carried out at 46% water fraction and 2.12 m/s mixture velocity. The drag expression of Schiller and Naumann [1] shows stratification which water hold-up of 80% at the bottom and 20% at the top wall of the pipe. The drag expression for single drop shows comparatively better mixing. The drag expression of Rusche and Issa [11] shows slightly better results then drag expression of Kumar and Hartland [3]. However, drag expression proposed by Rusche and Issa [11] is valid only for dense dispersions and cannot be applied for dispersed phase volume fractions less then 30%, while drag expression proposed by Kumar and Hartland [3] is applicable for dispersed phase volume fractions greater then or equal to unity. Hence, in the present study the drag expression proposed by Kumar and Hartland [3] is used whose predictions lies between drag on a single drop and drag in dense dispersions to predict the phase distribution for dispersed flow in horizontal pipeline.

3.2 Case II

Here the simulations are carried out using three different values of lift coefficient, *i.e.* -0.05, 0 and 1, respectively in conjunction with drag expression proposed by Kumar and Hartland [3] with DPN of 7.5. As shown in Figure 3, for C_L = 1 and 0.5, the phase distribution profiles shows near wall peaking at top wall while at the bottom of the pipe wall the phase is more homogeneously mixed for C_L = 1. For C_L = -0.05, the phase distribution profile shows wall peaking with considerable amount of water hold-up at top and bottom walls. The phase distribution profile for

C_L = -0.05 is similar to that observed by other researchers [4, 12].

3.3 Case III

Figure 4 shows the effect of individual inperphase force on phase distribution profile.

The results in Figure 4 clearly show that there is no considerable effect of lift and turbulent dispersion forces on phase distribution. There is no significant difference observed between the phase distribution profiles using only drag force and with all three interphase forces. When only turbulent dispersion force is used (DPN = 7.5) the flow is almost stratified while with only lift as the interphase force, the phase distribution profile at the bottom of the pipe shows separation while near wall peak is seen at the top wall. The possible reason may be due to the use of constant value of lift coefficient and turbulent dispersion force in the present study.

Figure 5 shows the comparison of the predicted phase distribution profile with experimental data of Soleimani [4].

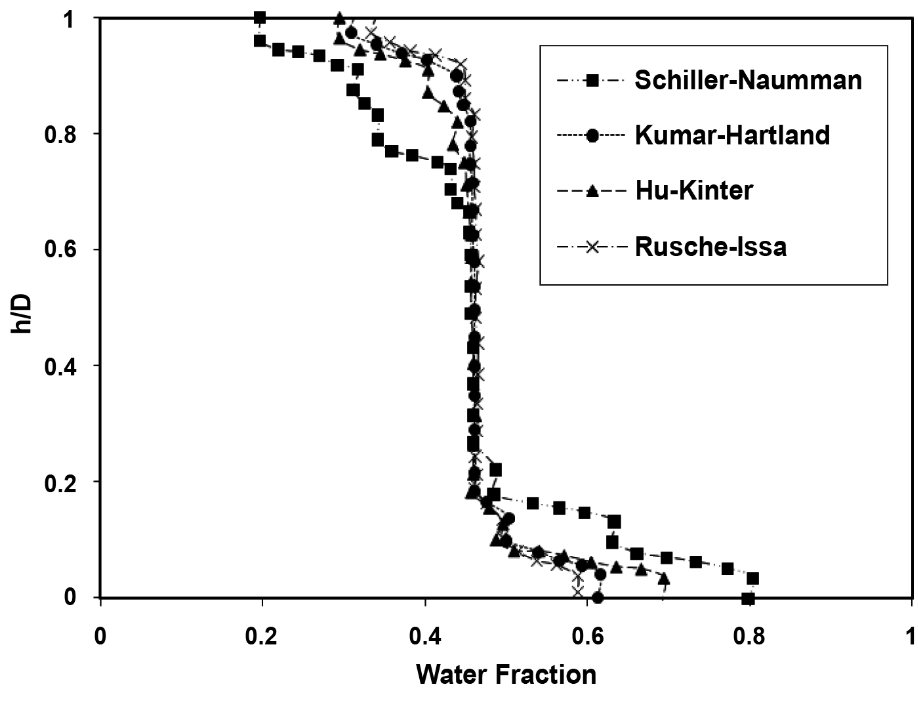

Figure 2: Comparison of drag models to study phase distribution profile at pipe cross section

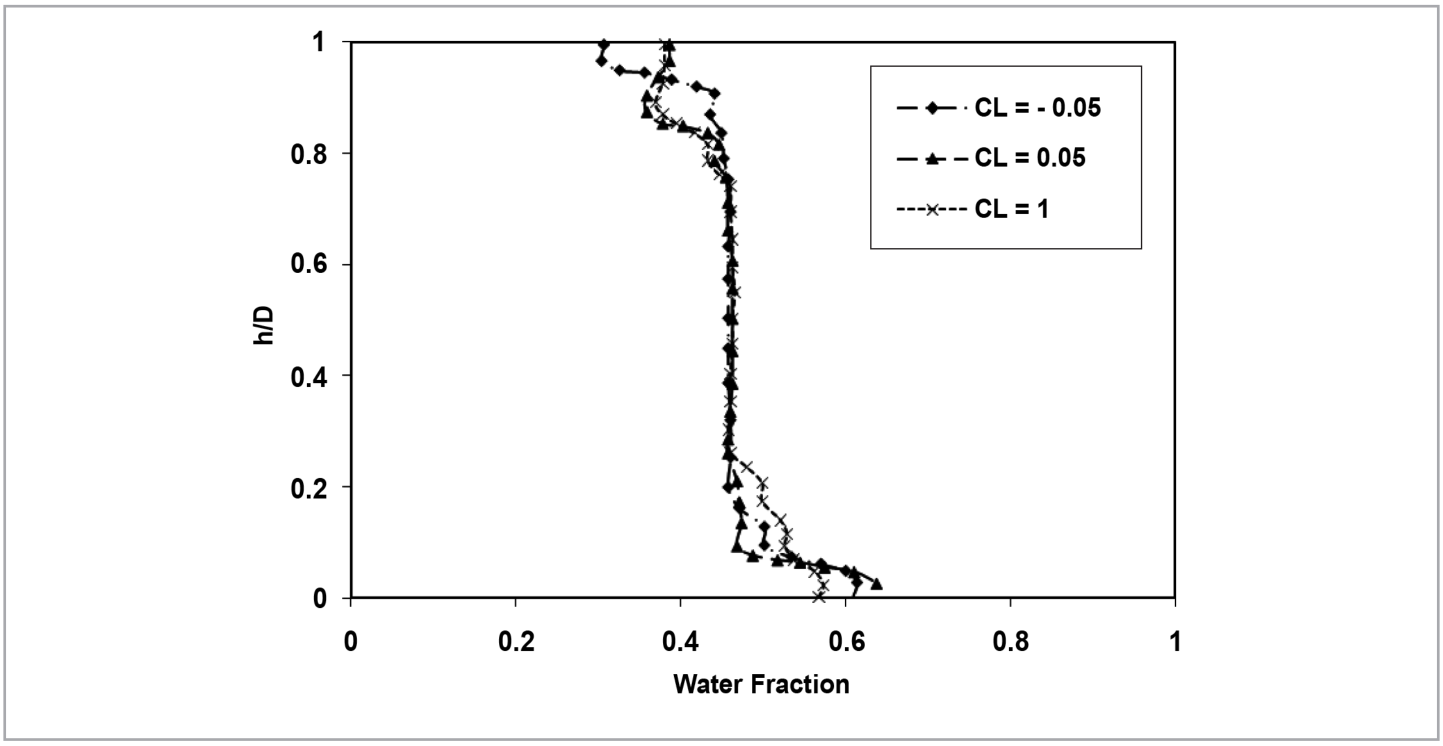

Figure 3: Phase distribution profile for different lift coefficient (C_L)

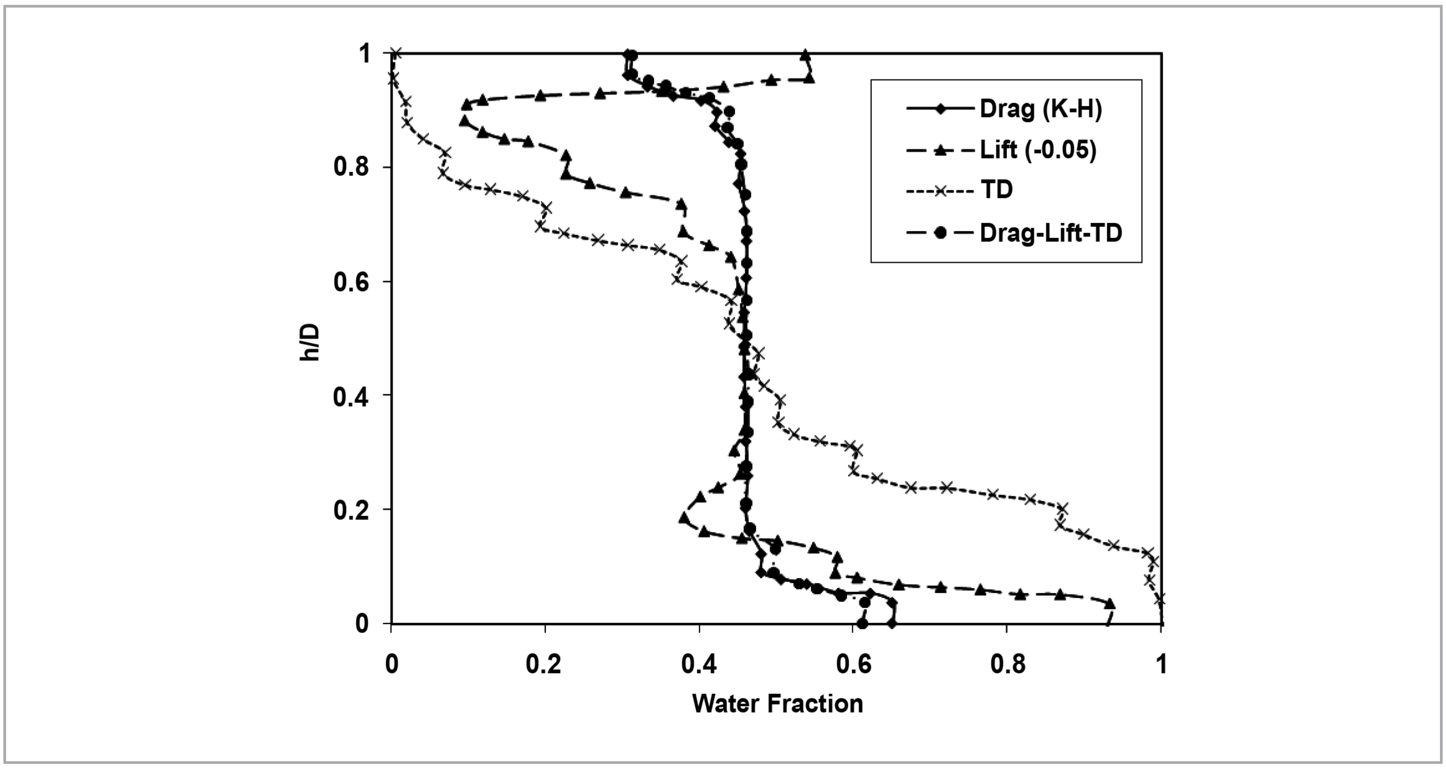

Figure 4: Effect of individual interphase forces on phase distribution profiles

It is observed that the phase distribution across the pipe cross section is in good agreement with the experimental data of Soleimani [4]. Effect of drag, lift and turbulent dispersion forces have been taken into account. All three forces need to be included in order to predict accurately the phase distribution in a dispersed liquid-liquid flow regime.

4.0 CONCLUSION

The effect of interphase forces on dispersion of oil-water mixture in a horizontal pipe is studied using CFD. The phase distribution profiles at pipe cross section are investigated. The results showed that drag is the major interphase force responsible in the phase distribution. However, for accurate prediction, the effect of lift and turbulent dispersion forces should be included.

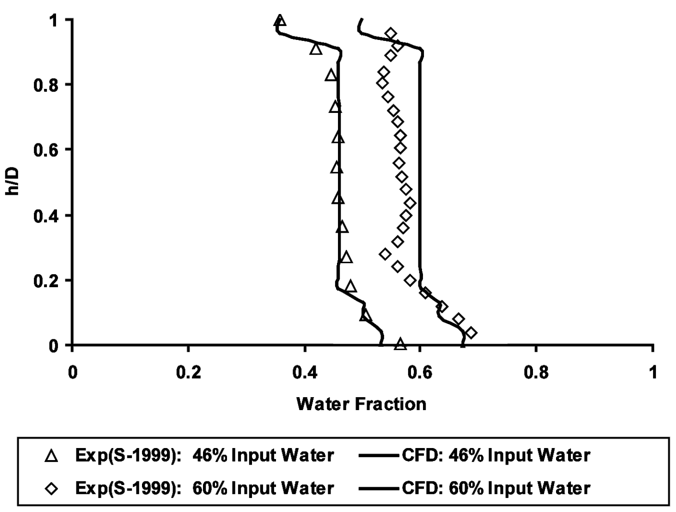

Figure 5: Comparison of vertical phase distribution profile at 46% and 60% input water and 3.0 m/s mixture velocity for data set of Soleimani [4]

5.0 ACKNOWLEDGEMENT

Rahsmi would like to acknowledge Universiti Putra Malaysia for research grant and also to the research team members for their support and guidance throughout this study. ■

NOTATION

C	constant
C_{D0}	Drag coefficient for rigid sphere
C_{DM}	drag coefficient in presence of adjacent drop
C_L	Lift coefficient
D	diffusion
d	drop diameter
F	force
G	rate of generation
g	Acceleration due to gravity
I	turbulence intensity
k	turbulent kinetic energy
l	turbulent length scale
R_e	Reynolds number
S	source term
U,V	velocity
Greek letters	
α	volume fraction
μ	viscosity
ε	turbulent dissipation rate
ρ	density
Γ	exchange coefficient
$\prod$	time
Subscript	
c, q	continuous phase
d, p	dispersed phase
s	slip
t	turbulent

REFERENCES

[1] Schiller, L., and Naumann, Z.Z. (1933). Uber Die Grundlegenden Berechungen Bei Der Schwerkraftbereitung, Z. Ver. Deutsch. Ing 77, 318-320.

[2] Ishii, M., and Zuber, N. (1979). Drag Coefficient and Relative Velocity in Bubbly, Droplet or Particulate Flows. American Institute of Chemical Engineers Journal 25, 843-855.

[3] Kumar, A., and Hartland, S. (1985). Gravity Settling in Liquid/Liquid Dispersions. Canadian Journal of Chemical Engineering 63, 368-376.

[4] Soleimani, A. (1999). Phase Distribution and Associated Phenomena in Oil-Water Flows in Horizontal Tubes. PhD Thesis, Imperial College, London.

[5] Ishii, M. (1975). Thermo-Fluid Dynamic Theory of Two-Phase Flow, Direction des Etudes et Recherches d'Electricité de France, Eyrolles, Paris, France.

[6] Angeli, P. (1996). Liquid-Liquid Dispersed Flows in Horizontal Pipes. PhD Thesis, Imperial College, University of London.

[7] Madhavan, S. (2005). CFD Simulations of Immiscible Liquid Dispersions. M.Sc Thesis, Dalhousie University, Canada.

[8] Hu, S., and Kintner, R. C. (1955). The fall of Single Liquid Drops through Water. American Institute of Chemical Engineers Journal., 1, 42-48.

[9] Klee, A. J., and Treybal, R. E. (1956). Rate of Rise and fall of Liquid Drops. American Institute of Chemical Engineers Journal 2, 444-447.

[10] Grace, J. R., Wairegi, T., and Nguyen, T. H. (1976). Shapes and Velocities of Single Drops and Bubbles Moving Freely Through Immiscible Liquids. Transaction of the Institution of Chemical Engineers 54,167-173.

[11] Rusche, H., and Issa, I. (2000). The Effect on Voidage on the Drag Force on Particles in Dispersed Two-Phase Flow. Japanese-European Two-Phase Flow Meeting, Tsukuba, Japan.

[12] Hussain, S. A. (2004). Experimental and Computational Studies of Liquid-Liquid Dispersed Flows. PhD Thesis, Imperial College, London.

[13] Simonin, O., and Viollet, P. (1990a). Predictions of an Oxygen Droplet Pulverization in a Compressible Subsonic Coflowing Hydrogen Flow. Numerical Methods for Multiphase Flows FED 91, 65-82.

[14] Simonin, O., and Viollet, P. (1990b). Modeling of Turbulent Two-Phase Jets Loaded With Discrete Particles. Proceedings of International Seminar on Phase Interphase Phenomena in Two-Phase Flow, Dubrovnik, ICHMT Belgrad.

IGBT INDUCTION HARDENING AND ITS APPLICATION IN SINGAPORE

(Date received: 17.12.2008)

N L Loh[1], L W Siew[2] and Y M Loh[3]
School of Mechanical and Aerospace Engineering, 50 Nanyang Avenue, Singapore 639798.
27 Woodlands Industrial Park E1, #02-11 Hiangkie Industrial Building IV, Singapore 757718
E-mail: [1]mnlloh@ntu.edu.sg, [2]lw_siew@yahoo.com.sg, [3]ymloh@doxon.com.sg

ABSTRACT

Induction hardening has come a long way. Whilst the vacuum tube power supply is still commonly used in industries, IGBT power supply is fast gaining industrial acceptance. In terms of power efficiency, the IGBT technology is arguably the most advanced, despite its demand for sound technical know-how on the combination of capacitances and inductances to achieve optimal effects. This paper aims to provide a brief review of the induction hardening process and the relationship of induction hardening parameters. This paper will demonstrate the importance of power density, frequency and traverse speed with particular reference to the experimental study on induction hardening of the AISI 4140 material. With these experimental data, two Master curves were achieved as an approach to ensure sound industrial treatment. This takes the form of determining the threshold requirement of power density to obtain maximum surface hardness. Finally, it will provide five case studies of industrial experiences in Singapore.

Keywords: *AISI 4140, Case Depth, Coiling, Frequency, Gear, Hardenability, Huge Part, IGBT Power Supply, Induction Hardening, Industrial Application, Microhardness Profiles, Optimum Surface Hardness, Power Density, Quenchant, Traverse Speed.*

1.0 INTRODUCTION

Induction hardening has been in the world since 1830 when Michael Faraday discovered how an electric current can induce magnetic flux and eddy current in a metallic conductor coupled to it. This breakthrough forms the basis for the induction hardening process.

Induction hardening is widely used and industrially popular particularly in the manufacturing, automotive and heavy engineering industries.(1-5) This is due to the numerous advantages it offers. Some of the more significant advantages is its rapid rate of heating-up as compared to the convection and radiation processes of heat transmission in standard furnaces. This would also mean less scaling losses, and faster startup resulting in higher productivity. The process also offers significant energy savings as power supply can be turned on or off easily without any need to maintain bulk energy inputs in the furnaces. Selective hardening can be performed on desired regions. Hence, only the desired areas need to be heated up and not the entire work piece as in conventional furnaces.

Over the last decade or so, Transitorized Solid State Power Supply is fast replacing the conventional vacuum tube power supply. It uses the Insulated Gate Bipolar Transistor technology (IGBT). The IGBT is fast overtaking the commonly-used silicon controlled rectifier technology (SCR).(6-8) Perhaps, the greatest advantage of employing IGBT power supply is its higher output efficiency as compared to the vacuum tube technology.

2.0 THEORY

2A. Fundamentals of the Induction Process

The basis of induction hardening lies in the ability to induce eddy currents in electrical conductors. A simple induction heating system consists of a coil (*inductor*) and a source of alternating current. The coil, also termed as inductor, is generally made of copper due to its favorable properties such as low electrical resistance and non-magnetism. The coil carries an alternating current surrounding the work piece to be induction hardened. The alternating current generates magnetic fields, which induce eddy current upon the work piece. These eddy currents heats up the work piece and raises the temperature beyond the transformation temperature instantly. Austenitization takes place and the structure is instantly quenched to produce martensite.

Figure 1 shows a typical induction hardening system which comprises of a power control unit, inductor unit, heat exchangers, cooling tower, distilled water system and water tanks.

2B. Parameters

There are many factors that will affect the final outcome of an induction hardening process.(9) In this paper, we will briefly discuss six main parameters. These are the power input, frequency, coil inductance (*turns*), proximity effect, dwelling time and quenching medium.

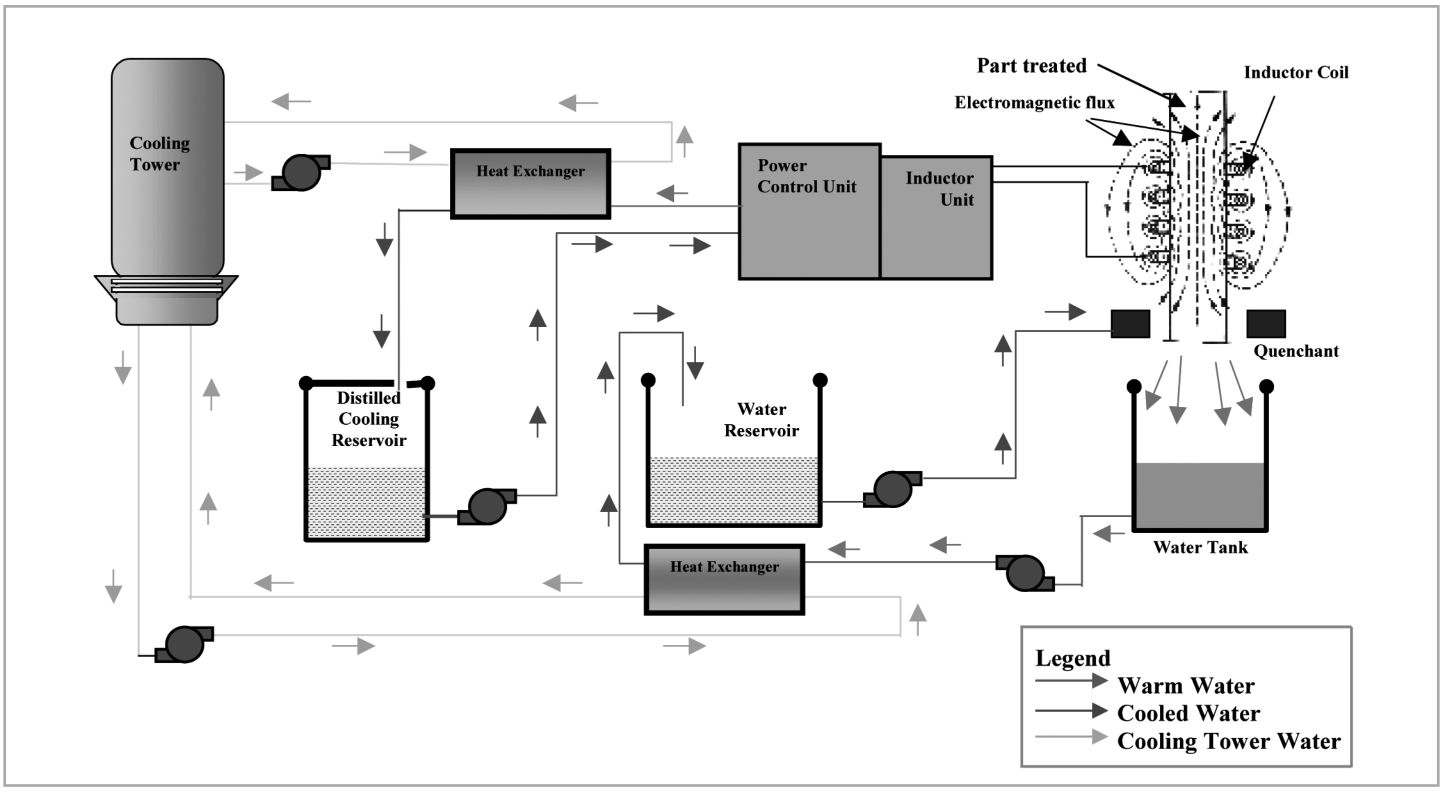

Figure 1: Schematic of a typical induction hardening system

(a) Power Input

In discussing about the power input, we prefer to consider **power density**, which is defined as the applied power divided by the surface area of the work piece.[10] As a general rule, low power density is used for through hardening to prevent overheating at the surface, whereas high power density is used for surface hardening to be achieved within the shortest possible time.

There are basically four main types of power sources: the line frequency system (*supply frequency*, 60*Hz*), motor generator system (*motor alternator*, 500*Hz* – 10*KHz*), solid-state system (*solid state inverter,* 180 – 50*KHz*) and vacuum tube (*radio frequency,* 50*KHz* – 10*MHz*). Figure 2 illustrates these four types of power sources operating at the various frequency zones for different applications. Depending on the nature of the heat treatment requirements, each system will have its unique features with distinctive advantages. Line-frequency system is used mainly in through hardening by the fact of its low operating frequency range. The efficiency of this system is high as no frequency conversion is required, hence power losses is kept to a minimum. In motor generator systems, the line-frequency current is changed to higher frequency current by electromagnetic induction using motors with copper windings. This gives a lower efficiency than the line-frequency system. The solid state system has been slowly replacing motor generator systems in the past few decades as it has lower cost and virtually no power consumption in standby mode, as compared to the motor generator system which requires 15% to 20% of maximum power consumption during standby mode. Apart from its shallow heating depth characteristic, vacuum tube system has the lowest efficiency and highest cost among the four power sources.

Choice of a power source depends primarily on frequency, although there is some overlap among frequency capabilities of the different sources. For high output power efficiency *e.g.*, the solid state power system will render better performances than the vacuum tube power system.

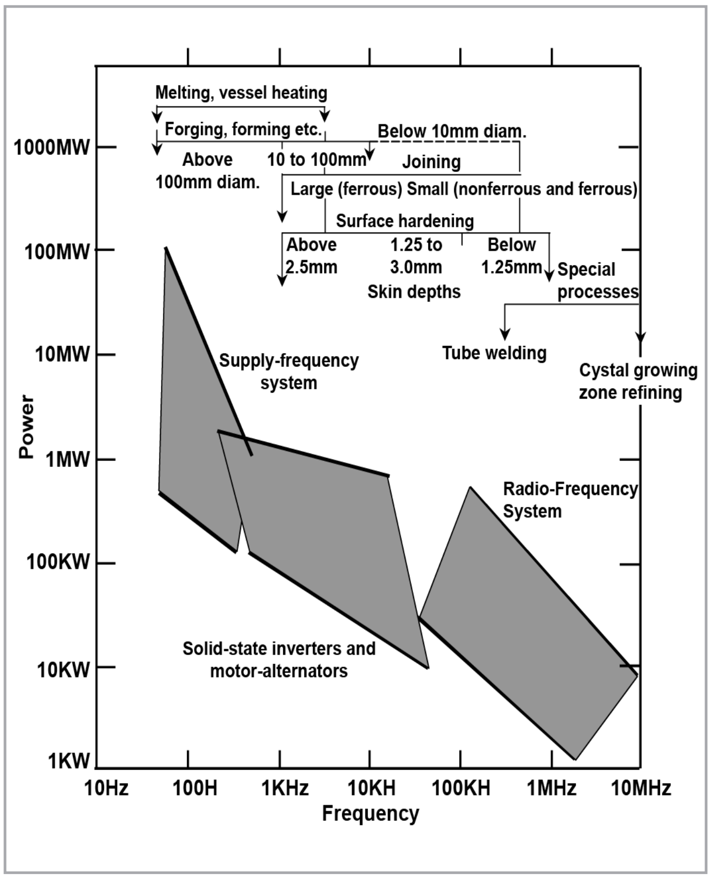

Figure 2: Different types of power sources operating at various frequency zones [11]

(b) Frequency Selection

The relationship of the electromagnetic field strength and the induced depth can be represented with Equation 1[12] :-

$$d = 5000 \sqrt{(\rho/\mu f)} \qquad \text{Equation 1}$$

where 'd' denotes the reference depth in cm, and 'f' as the frequency of the alternating electromagnetic field in hertz, 'ρ' is the resistivity of the work piece in ohm-centimeter, and 'μ' is the relative magnetic permeability of the work piece (*dimensionless*).

'd' is conventionally defined as the depth below surface at which the induced field strength and current are reduced to 37% of their surface values. As it is indicative of the skin effect of induction hardening where eddy currents are most intensive, it serves as a direct proportion of the case depth, which is normally defined by metallurgist as the case of martensitic transformation. Frequency is therefore, inversely proportional to the reference and case depths.

(c) Coiling Design

Coil design and inductance (*number of turns*) have tremendous effects on heating patterns and heat distribution. Depending on the geometry of the work piece and specification of the case depth uniformity and requirement, the inductor should be tailor-made for each application to ensure consistent and reliable treatment.[12-13]

(d) Proximity Effect

Proximity Effect refers to the air space between the work piece and the coil. This affects the heating pattern and intensities on the work piece.[10,12] For a work piece positioned close to the coil, the achievable case depth will be deeper. This is consequential of the higher power density. In this present paper, the air space between the specimens and the coil was kept as a constant to analyze the effect of the other parameters.

(e) Dwelling Time

Dwelling time has a significant effect on the work piece.[10,12] Too long a heat-dwelling time may overheat the surface resulting in melting, while too short a dwell time may not austenitize the surface to a sufficient depth. In the present experimental setup, the dwelling time was translated as the traverse speed of the specimens. Slower traverse speed would mean a longer dwelling time.

(f) Quenching Techniques and Quenchants

Quenching techniques and quenchants are important features of induction hardening. [10,12] The quenching technique used is based on the part size, geometry, hardenability of material and heating specification. Types of quenching medium include water, brine, oil, polyvinyl alcohol and polymeric solutions. The most common quenching medium used industrially is water. Oil is the preferred quenching medium for steels with high carbon content. This ensures slower cooling rates to prevent severe distortion and quench cracking. Water and brine are generally considered as severe quenchants. The cooling rate of polyvinyl alcohol solutions lies in between that of water and oil.

3.0 EXPERIMENTAL

The experiments were carried out with a 40-KW IGBT induction system. AISI 4140 specimens of Ø14 x 120 mm were induction hardened with varying parameters in power input, frequency and traverse speed as shown in Tables 1, 2 and 3. The effect of the variation of these parameters on the surface hardness and effective case depth will be discussed.

The study on the effects of rotational speed on the case depth were also carried out. However, the experimental results will be only presented in another paper. In this paper, the data presented was obtained with a rotational speed of 1.0 rev/sec.

3A Variation of Power Input

Table 1 : Parametric setup with variation in power input

Power	*8KW*	*11.6KW*	*15.2KW*	*19.2KW*	*22KW*
Fixed Parameters	Frequency 46 KHz, Traverse Speed 12.25 mm/s, Rotational Speed 1.0 rev/s				

3B Variation of Frequency

Table 2 : Parametric setup with variation in frequency

Frequency	*44KHz*	*46KHz*	*49KHz*	*52KHz*	*56KHz*
Fixed Parameters	Power 19.2KW, Traverse Speed 12.25 mm/s, Rotational Speed 1.0 rev/s				

3C Variation of Traverse Speed

Table 3 : Parametric setup with variation in transverse speed

Traverse Speed	*10.8 mm/s*	*13.8 mm/s*	*16.6 mm/s*	*19.6 mm/s*	*22.6 mm/s*
Fixed Parameters	Frequency 46 KHz, Power 19.2KW , Rotational Speed 1.0 rev/s				

For consistency of the experiment, induction hardening was started at the same reference level, 40 mm from the specimen base. The induction hardened specimens were sectioned at mid-points of the induction hardened zone. Figure 3 shows the induction hardened zone of the specimens. Table 4 shows the chemical composition of the AISI 4140 specimens.

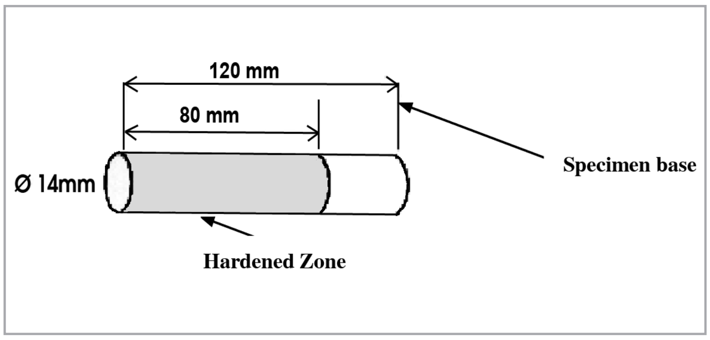

Figure 3: Specimens with induction hardened zone indicated

Table 4 : Chemical composition of AISI 4140 specimen (wt%)

	C	Cr	Mn	P	S	Si	V	Mo
AISI 4140	0.38-0.43	0.8-1.10	0.75-1.0	0.035	0.04	0.15	0.3	0.15-0.35

Induction hardened specimens were sectioned, mounted and prepared using standard metallographic techniques. Microhardness measurements were carried out using a Knoop microhardness indentor with a load of 200gmf held for 15 seconds. The metallographic specimens were etched with 3% Nital and microstructural observations were carried out at 1000 X magnification. Effective case depth is defined to be the distance from the surface where the hardness is 500HK.

4.0 RESULTS AND DISCUSSION

4A. Variation of Power Input

Table 5 shows the variation in power density and the effects in effective case depth with various power inputs, all other parameters being held constant at 46 KHz and traverse speed 12.25 mm/s. The power density is derived from the equation : Power Input / Specimen Circumference x Traverse Speed in Watt/mm^2. Figure 4 shows the microhardness profiles of induction hardened specimens.

Table 5: Variation in power density and its influence on effective case depth

Power	8 KW	11. 6 KW	15.2 KW	19.2 KW	22 KW
Power Density	14.8 W/mm	21.5 W/mm	28.2 W/mm	35.6 W/mm	40.8 W/mm
Effective Case Depth	0	0.85 mm	2.35 mm	4.50 mm	5.20 mm

The results showed that effective case depth increases with increasing power density. For the power density of 14.8W/mm^2, the surface hardness remained at 280 HK. No increase in hardness at the surface was observed. Thus, it was obvious that no martensite was formed – *i.e.*, power was insufficient to reach the transformation temperature.

With power density inputs ≥ 21.5 W/mm^2, surface hardness reached an optimum range of 650 ± 50 HK. As power density increases, effective case depth increases as more materials are raised beyond the transformation temperature.

4B. Variation of Frequency

Using a power input of 19.2 KW and a traverse speed of 12.25 mm/sec, frequency was varied to study its effects on case depth. Consistent with equation 1, case depth increases with decreasing frequency. Of noteworthy, is the observation that the surface hardness range maintained at optimum range of 650 ± 50 HK. Thus, the surfaces were all fully austenitized.

Table 5: Variation in frequency and its influence on effective case depth

Frequency	56KHz	52KHz	49KHz	46KHz	44KHz
Effective Case Depth	3.00mm	3.00mm	4.05 mm	4.50mm	5.80mm

Frequency relates to the "*skin effect*", the depth of which is inversely proportional to the square root of the frequency[11]. The thickness of the skin however, is directly linked to the case depth. Hence, as frequency decreases, it will produce a thicker skin effect that generates a deeper case depth, as indicated in Figure 5.

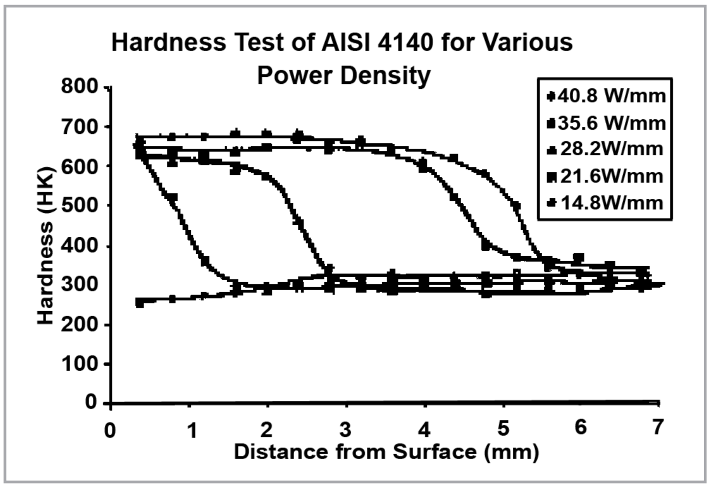

Figure 4 : Micohardness profiles at various power densities

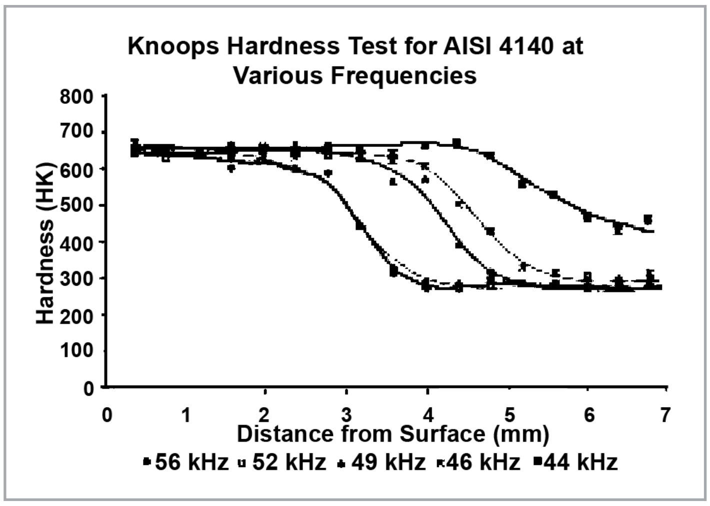

Figure 5 : Micohardness profiles at various frequencies

4C. Variation of traverse speed

Table 6 shows the results obtained by variation in traverse speed with fixed settings of 19.2 KW and 46 KHz. The effective case depth reduces as the traverse speed increases. No hardening effect is observed on the test sample surface with a traverse speed of 22.6 mm/s. This was much attributed to the short dwelling time as a result of high traverse speed such that the surface is unable to achieve the austenitizing temperature during the heating process.

Conversely, the test sample that was treated at a slower traverse speed of 10.8 mm/s has resulted in hardening throughout the entire core.

Table 6: Variation in traverse speed and its influence on effective case depth

Traverse Speed	10.8 mm/s	13.8 mm/s	16.6 mm/s	19.6 mm/s	22.6 mm/s
Effective Case Depth	7 mm	2.75 mm	1.40 mm	0.55 mm	0

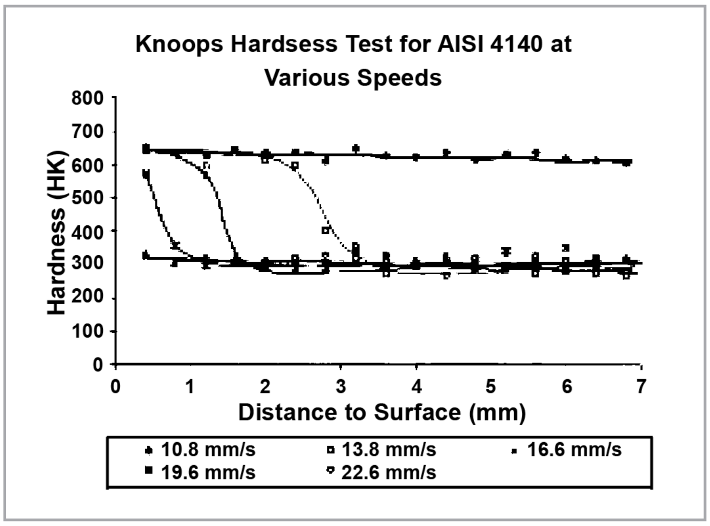

Figure 6 : Micohardness profiles at various traverse speeds

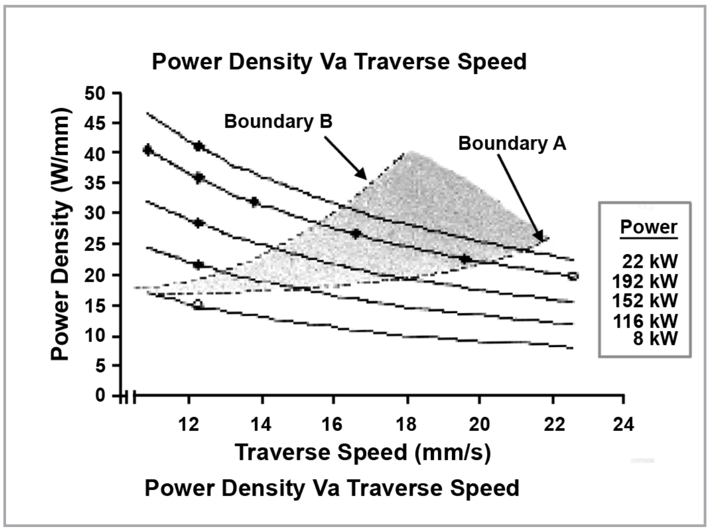

♦*Denotes hardened Surface* o *Denotes non hardened surface*
Figure 7 : Master curves for the induction hardening of Ø14 diameter shaft of AISI 4140 materials

4D. Master Curves

Power density input is related to the traverse speed of the specimen. For a given power input, the power density increases as traverse speed decreases. It is defined as the power input over surface area of specimen per unit time. Industrially then, it is advantageous to link the power density generated to the traverse speed and the power input.

Figure 7 shows a family of curves that were extrapolated from the experimental data with two Master curve boundaries A and B derived. The Master curves can help an operator to ensure sufficient power density input for austenitization to take place. Below boundary A, no hardening will occur as power density input will be insufficient to reach the transformation temperature. Optimum surface hardness range of 650 ± 50 HK is achievable only with parameters beyond boundary B.

When parametric settings between the two boundaries as indicated in the shaded region are used, partial formation of martensite takes place and maximum surface hardness is not realizable.

5.0 INDUSTRIAL CASES

In Singapore, there are numerous in-house facilities for induction heating designed specifically for mass production. These are normally of the vacuum tube power supplies that are known for their easy operations albeit poor power efficiencies. There are reports that power efficiency can be as low as 50%. In 1994, Doxon Engineering acquired an IGBT power supply to serve an American MNC. This proves to be viable and versatile. With sound technical know-how and good quality assurance practices, various material grades such as medium to high carbon steels, low-alloy steels and martensitic stainless steels can be effectively case hardened. To date, the Company has served more than 50 Clients, covering over a broad spectrum of industries to include the automotive, manufacturing, precision, marine and heavy engineering. With the aid of automation, flux intensifiers and coil design know-how, a broad range of engineering components were successfully induction hardened with minimum dimensional distortion and quench cracking. Here are but five examples:

5A. Shafts

Figure 8 shows a crate of shafts of AISI 4140 material with a hardness of about 30 HRC. In this instance, the induction hardening was carried out on one side of the shaft only. Herein is a powerful advantage of selective induction hardening over the conventional hardening process in standard furnaces. An effective and consistent case depth of 1.2 mm with a hardness of 42 – 47 HRC was specified and achieved. Figure 9 shows its typical microhardness profile.

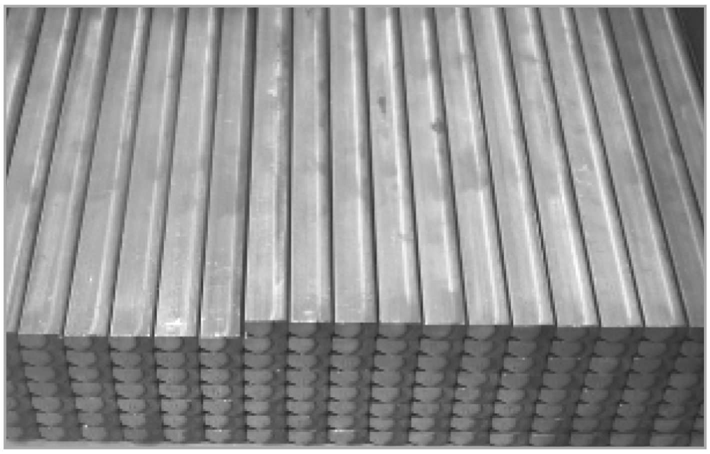

Figure 8: Induction hardened shafts

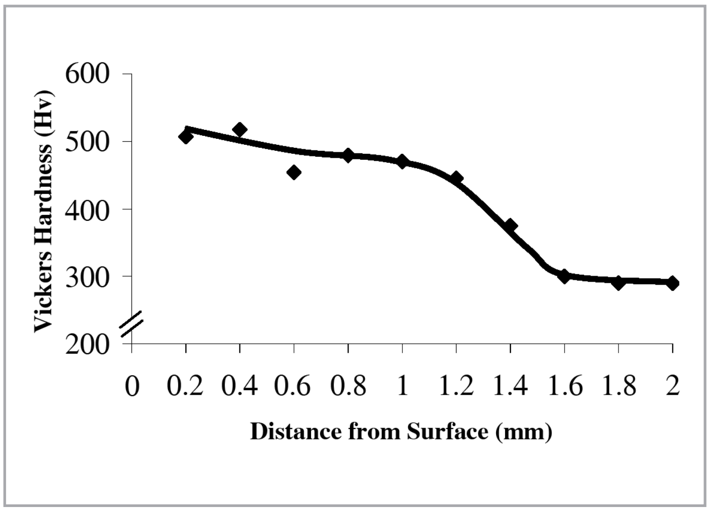

Figure 9: Microhardness profile of Shaft

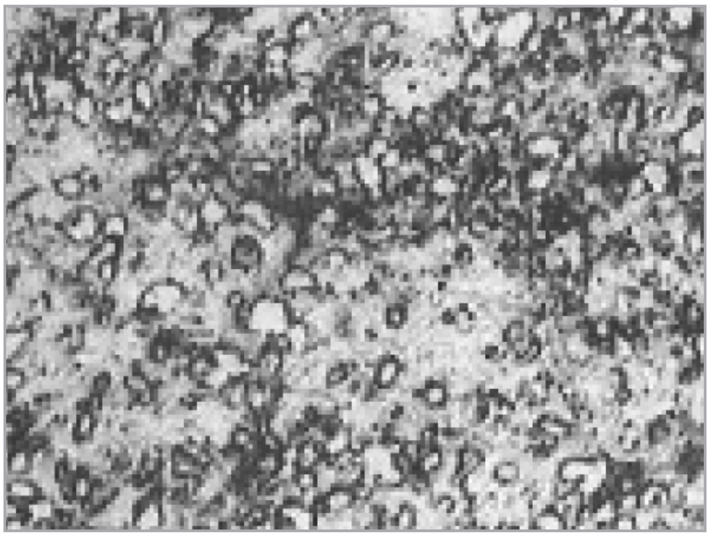

Figure 10 : Microstructure of AISI 4140 shaft. (1000 X Magnification)

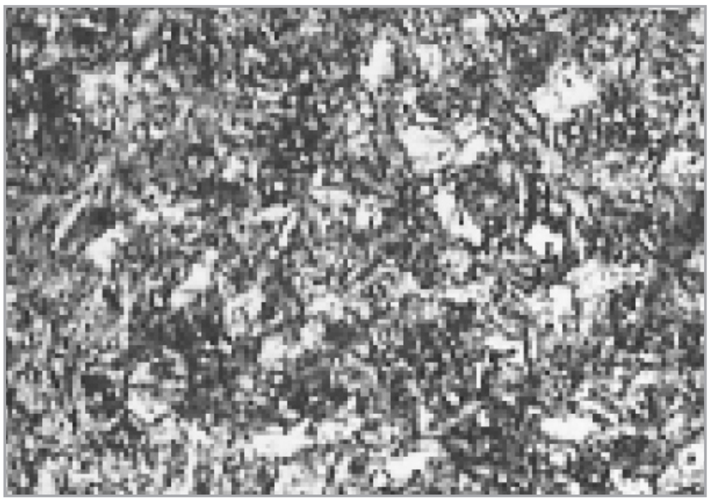

Figure 11 : Microstructure of induction hardened AISI 4140 shaft. (1000 X Magnification)

Figure 10 shows the microstructure of the shaft at 1,000X magnification. It consists of spheroidal carbides in a ferritic matrix. Figure 11 shows the corresponding tempered martensitic structure of the case with some retained austenites.

5B. Heavy Engineering Rollers

Figure 12 shows AISI 4140 rollers of outer diameter 940 mm and inner diameter 360 mm. The height measures about 280 mm and the component weighs some 650 Kg. When vacuum hardened, the rollers exhibited severe quench cracking as shown in Figure 13.

The component was successfully induction hardened at Doxon to a depth of 1.0 to 2.0 mm with 40 to 50 HRC. No cracking was observed and dimensional tolerances fell well within engineering specifications. This particular case highlights the possibility of induction hardening as a viable alternative to vacuum hardening of huge engineering parts.

Figure 12: Induction Hardened Rollers

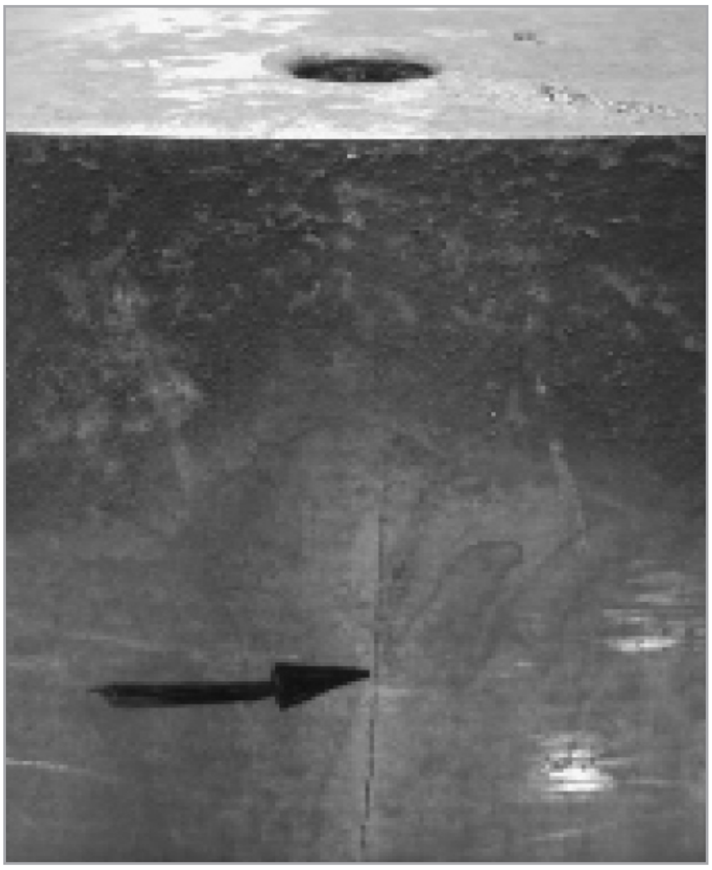

Figure 12: Induction Hardened Rollers

5C. Sprocket Gears

Figure 14a and 14b shows AISI 4140 sprocket gear hubs and shafts with gear teeth of PCD diameters 250 by thickness 50 mm to be induction hardened. The gear profile was treated to a surface hardness range of 45 to 50 HRC with a uniform case depth range of 1 to 2 mm. Figure 15 shows the cross section of the hardened layer obtained after induction hardening.

Figure 14a: Induction hardened sprocket gear hub

Figure 14b: Induction hardened sprocket gear shaft

5D. Elevator Segment

Figure 16 shows the induction hardened elevator segments used for the elevator chain. The material grade is AISI 1045. The induction hardening treatment was localized on the teeth portion of the elevator segment. Surface hardness range and case depth of 40 - 45 HRC and 0.8 - 1.5 mm were achieved respectively. Treatment at other portion particularly the two inner holes of diameter 7mm were avoided to ensure overall toughness in the elevator chain system.

Figure 16 Mass production loads of the elevator segments

Figure 17 Treatment at the inner hole of the taper holder

5E. Taper Holder

Figure 17 shows a taper holder assembled in production machineries. Induction hardening at the inner taper surface and internal diameter of the taper holder was effectively processed with an integrated coiling and fixturing design. The material grade of the holder is AISI 4340. Surface hardness range and case depth of 45 - 52 HRC and 1 - 1.5 mm were achieved respectively.

6.0 CONCLUSION

The experimental results showed the influence on effective case depth with variation in power input, frequency and traverse speed during the induction hardening process. Effective case depth increases with increasing power density, decreasing frequency and traverse speed.

From the results, obtainable optimum surface hardness range for AISI 4140 material grade was 650 ± 50 HK. AISI 4140 shaft of diameter 14 mm will need a power density $\geq$ 21.5 Watts/mm^2 at 46 KHz to achieve effective surface hardening with optimum surface hardness range.

A family of curves was extrapolated from the experimental data and Master curve boundaries A and B were derived. Boundary B can be used to approximate the minimum power density requirement to achieve optimum surface hardness range 650 ± 50 HK for the treatment of AISI 4140 shaft. No hardening will take place with power density lower than boundary A.

Automated IGBT induction hardening is versatile for the case hardening of engineering components. With a sound knowledge of the system, parts varying from 0.2 Kg to 650.0 Kg with various geometrical shapes and sizes have been successfully case-hardened. Huge engineering parts known to suffer quench cracking under vacuum hardening conditions, may be effectively induction hardened to produce uniform case depths.

7.0 ACKNOWLEDGEMENT

The authors wish to acknowledge the sponsorship and support of Nanyang Technological University and Doxon Engineering Pte Ltd, without which this paper would have been impossible. In particular, the experimental work done by M/s Tan S F is respectfully acknowledged. ■

REFERENCES

[1] K.Z. Shepelyakovskii , *Technology Of Heat Treatment Using Induction Heating, 50th Anniversary Of Induction Surface Hardening*, Moscow Institue of Advanced Metallurgy, pp2-10, Aug 1987.

[2] G.F. Golovin, A.N Shamov, *Induction Heat Treatment As A Means Of Increasing Production*, All Union Scientific-Research Institute Of High-Frequency currents, pp15-19, Aug 1987.

[3] Charanjit Charlie Lal, *Induction Hardening Of Cast Iron Cylinder Head Valve Seats*, Materials Science Forum Vols. 102-104, pp 365-372, 1992.

[4] Lain Bates, *Heat Treatment By Induction*, Materials World, May 1996

[5] S. Segerberg, *Magnetic-Field Heating For In-Line Through Hardening*, Heat Treatment Of Metals, pp53-56, 2000.3.

[6] Hidetoshi Umida, Power Electronic Technology Trends and Prospects, Fuji Electric Journal, Vol. 75 No. 8, 2002.

[7] P K Sadu, *Analysis Of A Series Resonant Superimposed Inverter Applied To Induction Heating*, IE Journal, pp 214-217, Vol 8, Mar 2004.

[8] Thomas Luttin, *Modular Power Converter (MPC): IGBT-Converter Series For High Power Applications In Electrical Traction*, Lausanne, Switzerland, pp218, EPE 1999.

[9] Yunwang Ge, *Optimization Control of Induction Hardening Process*, Proceedings of the 2006 IEEE International Conference, pp 1126-1130, June 2006.

[10] E.J Davies, *Conduction and Induction Heating*, Institution of Electrical Engineers, (1990).

[11] J. Davies and P. Simpson, *Induction Heating Handbook*, Mcgraw-Hill London 1979

[12] S.L. Semiatin, D.E. *Stutz, Induction heat treatment of steel*, American Society For Metals (1985).

[13] R.S. Ruffini and R.T. Ruffini, *Advanced Design of Induction Heat Treating Processes and Work Coils*, Heat Treatment of Metals, pp84-89, 1999.

PROFILES

DR LOH NEE LAM

Dr Loh Nee Lam is an Associate Professor of the Nanyang Technological University. Presently, he is the Dean of Admission. He also sits in the Expert Panel Committee of the Institute of Engineers, Singapore. He was the founder President of the Institute of Materials (E Asia). Dr Loh specializes on surface engineering and mechanical properties of engineering materials. He is a co-author of the book "Materials Degradation and its Control by Surface Engineering" published in Imperial College Press,UK.

MR SIEW LEONG WAI

Mr Siew Leong Wai graduated from the Nanyang Technological University with a first class honor in Bachelor Degree in Mechanical and Production Engineering. He has ten years of industrial experiences in heat treatment industry sector and is currently the General Manager of Doxon Engineering Pte Ltd.

MR LOH YEW MINH

Mr Loh Yew Minh graduated from the National University of Singapore with a Bachelor degree in Computer Science. He has four years of industrial experiences in heat treatment industry sector and he is presently the Sales & Project Manager of Doxon Engineering Pte Ltd.

ARIMA MODELS FOR BUS TRAVEL TIME PREDICTION

(Date received: 6.3.2009)

Suwardo[1], Madzlan Napiah[2] and Ibrahim Kamaruddin[3]
[1]Civil Engineering Department, Faculty of Engineering,
Gadjah Mada University, Yogyakarta 55281, Indonesia
[2,3]Civil Engineering Department, Universiti Teknologi PETRONAS,
Bandar Seri Iskandar, 31750 Tronoh, Perak
E-mail: [1]suwardo@yahoo.com

ABSTRACT

In this paper, the time series model, Autoregressive Integrated Moving Average (ARIMA) is used to predict bus travel time. ARIMA model is simpler used for predicting bus travel time based on travel time series data (historic data) compared to regression method as the factors affecting bus travel time are not available in detail such as delay at link, bus stop, intersection, etc. Bus travel time prediction is an important aspect to bus operator in providing timetable for bus operation management and user information. The study aims at finding appropriate time series model for predicting bus travel time by evaluating the minimum of mean absolute relative error (MARE) and mean absolute percentage prediction error (MAPPE). In this case, data set was collected from the bus service operated on a divided 4-lane 2-way highway in Ipoh-Lumut corridor, Perak, Malaysia. The estimated parameters, appropriate model, and measures of model performance evaluation are presented. The analysis of both Ipoh to Lumut and Lumut to Ipoh directions is separately performed. The results show that the predicted travel times by using the moving average, MA(2) and MA(1) model, clearly fit with the observed values for both directions, respectively. These appropriate models are indicated by the minimum MARE and MAPPE values among the tentative models. It is concluded that MA(2) and MA(1) models are able to be appropriately applied in this case, and those models can be used for bus travel time prediction which helping in the timetable design or setup.

Keywords: *Autoregressive Integrated Moving Average, Bus Travel Time, Mean Absolute Percentage Prediction Error, Mean Absolute Relative Error, Time Series Model*

1.0 INTRODUCTION

Bus travel time is an important attributes of trip that many people asking for their traveling purpose by using bus service. Generally, people consider travel time as well as other factors such as ticket fare, bus facilities, comfort, safety, *etc*. They prefer to minimize time spent for moving from a place to other place by choosing the best bus service. Therefore, the transport planner needs to elaborate the importance of bus travel time to improve the performance of bus service.

An important aspect of quality of bus service is service reliability. Reliability is used to ensure that the bus service will depart and arrive on time at certain distance accordingly. Bus arrival time is affected by departure time, travel time and delay, therefore, travel time is important factor of bus service reliability. The reliability is improved further for attracting more passengers use bus. Then, bus travel time series data is compiled for predicting bus travel time. Autoregressive Integrated Moving Average (ARIMA) model is simpler kind of time series data analysis than the regression method for prediction while the travel time series data is available.

Time series data was recorded in term of total bus travel time from start to end terminal which including delay (at link, bus stop, intersection, incident, *etc*.). In this case, delay is not separated in detail from the total time. Thus, ARIMA was applied to predict bus travel time based on travel time series data (historic data). That is the reason to apply ARIMA model in predicting bus travel time.

Based on explanation above, ARIMA model is simpler used for predicting bus travel time based on travel time series data (historic data) than regression method as the factors affecting bus travel time are not available in detail such as delay at link, bus stop, intersection and incident location.

2.0 OBJECTIVE AND SCOPE OF STUDY

The objective of this model is to predict the travel time of bus which running from end-to-end bus terminal based on the time series data or historic data of travel time. For further, transportation engineer/planner will take the benefit of this study in the timetable design or setup.

The time series data of bus travel time were collected starting from January to December 2007 for two typical days a month, workday and weekend. The data collection was performed during the running period of a two way bus trip as named on board survey. This paper focuses on deriving and discussing model of bus travel time prediction by using ARIMA model. Model development stages is described in flow chart and followed with model validation (See sub-section 5.2).

3.0 PREVIOUS STUDY ON BUS TRAVEL TIME

The minimum total travel time spent by users is the one of typical users' objectives in using transit service among other measures such as personal accessibility, excess time, congestion, total travel cost, direct travel cost, coverage, traveler satisfaction, accident rate, and criminal activity [1-2].

With the development of Intelligence Transportation System (ITS), the concept of providing users with reliable information about bus arrival time at bus stops has emerged as Advanced Traveler Information Systems (ATIS) and Advanced Public Transportation Systems (APTS). Some of information for users included bus travel time, bus location, speed, passengers on board and dwell time. The information collected by agencies (manually recorded or real time provided) becomes historical information and assists transit agencies with planning, management, and control of the system as well as the improvement of service.

The primary objective of APTS, relating to transit passengers, is to improve the distribution of information about the public transport system such as, travel time, delay, and vehicle position [3]. Hence, the prediction of bus arrival time at bus stop is found to be valuable information for passengers to help reduce their waiting time.

The importance of bus arrival time prediction models as a component of ATIS has been well argued by numerous researchers [4-6]. Bus arrival prediction has become a critical component of the systems [7]. In the prediction of arrival time, the travel time is a part of system as well as delay. In the analysis of historical bus travel time, the coefficient of variation differed between time-points. The coefficient of variation is related to the mean absolute percentage prediction error (MAPPE) achieved using time series (full autoregressive) prediction models. Links with a higher coefficient of variation had a higher MAPPE and links with a lower coefficient of variation had a lower MAPPE [8].

Some models were used to predict travel time such as, regression method and neural network. Regression method requires the availability of dependent variable and whatever factors as being independent variables. Neural network is more complicated approaches and not simple in application. As generally known, ARIMA From above reason, ARIMA is chosen to predict bus travel time based on the bus travel time series data.

4.0 CASE STUDY AND DATA COLLECTION

Ipoh-Lumut corridor is located at Perak State in Peninsular Malaysia which link the Ipoh City (State Center) and Lumut Port (where the Malaysia Navy and Pangkor Island, tourism place located). A long this corridor, there are many attractive and potential land uses which potentially generate and attract the trips of people. This corridor is categorized into rural area with some important central business district (CBD) including such as residential area, school, state building, and universities. The 82.6 km length of divided multiple lane highway is the main road in this corridor connecting three districts, Kinta (Ipoh City), Perak Tengah and Manjung. The regular bus services are operated from 07:00 to 21:00. Figure 1 shows the illustration of bus service operation, such as location, departure time, distance and travel time. The main bus stop locations are indicated in the figure, but the bus actually can stop any where for boarding and alighting of passengers.

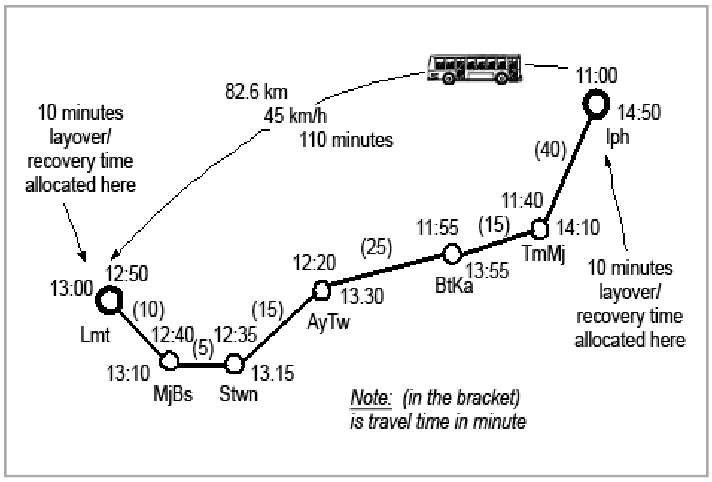

Figure 1: Location and scheduled departure of case study

In this study, data for analysis was collected during full one day period (07:00-21:00), one week period (11:00-15:00) and one year period (11:00-15:00). The data used is primarily collected by on-board survey over the Perak Roadways's 14-hour weekday service, which is playing Ipoh-Lumut corridor. The number of data points used for analysis was 12 months x 2 days per month x 2 trips per day = 48 trips per year. The primary data collected for analysis comprise the following:

a. arrival and departure times of the bus at stop points
b. location of stop points (bus station, bus stop and non bus stop)
c. name of location and environmental situation within the bus route

In addition, secondary data were also used to help surveyor on the primary data collection, such as road network map, timetable and other information on existing bus service.

On-board survey was conducted with more accurate and detailed information gathered about vehicle movement and boarding and alighting of passengers compared to at check point survey. As the survey is conducted by observer getting on a vehicle traveling over the route along a period of time, so that it is called as on-board survey. The observer records the data of location and the time at which the vehicle stop for boarding and alighting of passengers and other data need. For this case the handheld GPS was used for recording the spatial and timely data. For addition, the observer also could count the boarding and alighting passengers over an entire route for a specified time period. At this point, there was no device installed in the bus service system as well as used in more advanced bus service in other city, so that, there was no GPS data collected with advance system in this case.

In this paper, GPS is merely used as instrument or tools in data collection which support in recording the spatial and time based data of bus operation. Here, GPS is not applied specifically in estimating bus arrival in term of providing the real time information.

The type of bus service is regular stage-bus service which operates in mixed traffic. It is true that its travel time is affected by some factors, such as delay at intersection, delay at link and delay at bus stop. The data used for prediction is total bus travel time from the start to the end terminal which is compiled in time series based data. So that this study focus on the total travel time from start to end terminal. The bus travel time in mixed traffic is influenced by factors, such as level of traffic, delay (at link, junction and bus stop), departure time, and number of bus stop. In this case, the focus is not on the detail factors affecting bus travel time. Otherwise, the model is just applied to data series of bus travel time.

5.0 DEVELOPMENT OF ARIMA MODEL

5.1 Time Series Analysis Using ARIMA Model

In this section, it is shortly reviewed the non-seasonal Box-Jenkins Models for a stationary time series data. The Box-Jenkins methodology refers to the set of procedures for identifying, fitting, and checking the ARIMA models with time series data. Prediction or forecasts follow directly from the form of the fitted model [9].

Identification of the type of time series formula within ARIMA models are discussed briefly below.

5.1.1 Autoregressive Model

Autoregressive (AR) is defined as the model of a time series in which the current value of the series is a linear combination of previous values of the series, plus a random error. A p^{th}-order autoregressive model which is noted as AR(p) has the general form,

$$Y_t = \phi_0 + \phi_1 Y_{t-1}, \phi_2 Y_{t-2} + \ldots + \phi_p Y_{t-p} + \varepsilon_t \quad (1)$$

Where,

Y_t = Response (dependent) variable at time t

Y_t–1, Y_{t-2}, …, Y_{t-p} = Response variable at time lags t–1, t–2, …, t–p, respectively

$\phi_0, \phi_1, \phi_2, \ldots, \phi_p$ = Coefficients to be estimated

ε_t = Error term at time $_t$

5.1.2 A.2 Moving Average Model

A Moving Average (MA) is simply a numerical average of the last N data points. The simple moving average is intended for data of constant and no trend nature. A q^{th}-order moving average model which is symbolised as MA(q) has the general form,

$$Y_t = \mu + \varepsilon_t - \theta_1\varepsilon_{t-1} - \theta_2\varepsilon_{t-2} - \ldots - \theta_q\varepsilon_{t-q} \quad (2)$$

Where,

Y_t = Response (dependent) variable at time t

μ = Constant mean of the process

θ_1, θ2, …, θq = Coefficients to be estimated

ε_t = Error term at time t

$\varepsilon_{t-1}, \varepsilon_{t-2}, \ldots, \varepsilon_{t-q}$ = Errors in previous time periods that are incorporated in the response Y_t

5.1.3 Autoregressive Moving Average Model

As a combinatory model, the Autoregressive Moving Average Model is generally noted as ARMA(p,q) which has the general form,

$$Y_t = \phi_0 + \phi_1 Y_{t-1} + \phi_2 Y_{t-2} + \ldots + \phi_p Y_{t-p} + \varepsilon_t$$
$$- \theta_1\varepsilon_{t-1} - \theta_2\varepsilon_{t-2} - \ldots - \theta_q Y_{t-q} \quad (3)$$

Since the time series data prepared, then it can be produced the graph of sample autocorrelation function (ACF) and the sample partial autocorrelation function (PACF) to determine the form of models, which the processes can be summarised by referring Table 1 as follows:

Table 1: How to determine the model by using ACF and PACF patterns

Model	ACF	PACF
AR(p)	Dies down	Cut off after lag q
MA(q)	Cut off after lag p	Dies down
ARMA (p,q)	Dies down	Dies down

5.1.4 Autoregressive Integrated Moving Average

Autoregressive Integrated Moving Average is abbreviated as ARIMA. ARIMA is a general model widely used in time series analysis. Based on the prior investigation of the behavior of a series, it is specified three numbers that represent the order of autoregressive (p), the degree of differencing (d), and the order of moving average (q). Thus, the general form of model is written as ARIMA(p,d,q). The model can be extended to incorporate seasonality.

5.2 Steps In The ARIMA Model Building

The steps in the ARIMA model-building are briefly explained below. Figure 2 shows the flow chart of model development stages and model validation.

5.2.1 Model Identification

First step is to create ACF and PACF graph. A graph of autocorrelation function (ACF) is used to determine whether the series is stationary or not. The time series is considered stationary if the graph of ACF of the time series values either cuts off fairly quickly or dies down fairly quickly. If the graph of ACF dies down extremely slowly, then the time series values should be considered non-stationary. If the series is not stationary, it can be converted to a stationary series by differencing. The original series is replaced by a series of differences. An ARMA model is then specified for the differenced series. Differencing is done until a plot of the data indicates that the series varies about a fixed level, and the graph of ACF either cuts off fairly quickly or dies down fairly quickly.

Model for non-seasonal series are called Autoregressive integrated moving average model, denoted by ARIMA(p,d,q). Here, p indicates the order of the autoregressive part, d indicates the amount of differencing, and q indicates the order of the moving average part. If the original series is stationary, $d = 0$ and the ARIMA models reduce to the ARMA models.

ARIMA (p,d,q) has the general form,

$\phi_p(B)(1 - B)^d Y_t = \mu + \theta_q(B)\varepsilon_t$

or $\phi_p(B)W_t = \mu + \theta_q(B)\varepsilon_t$ (4)

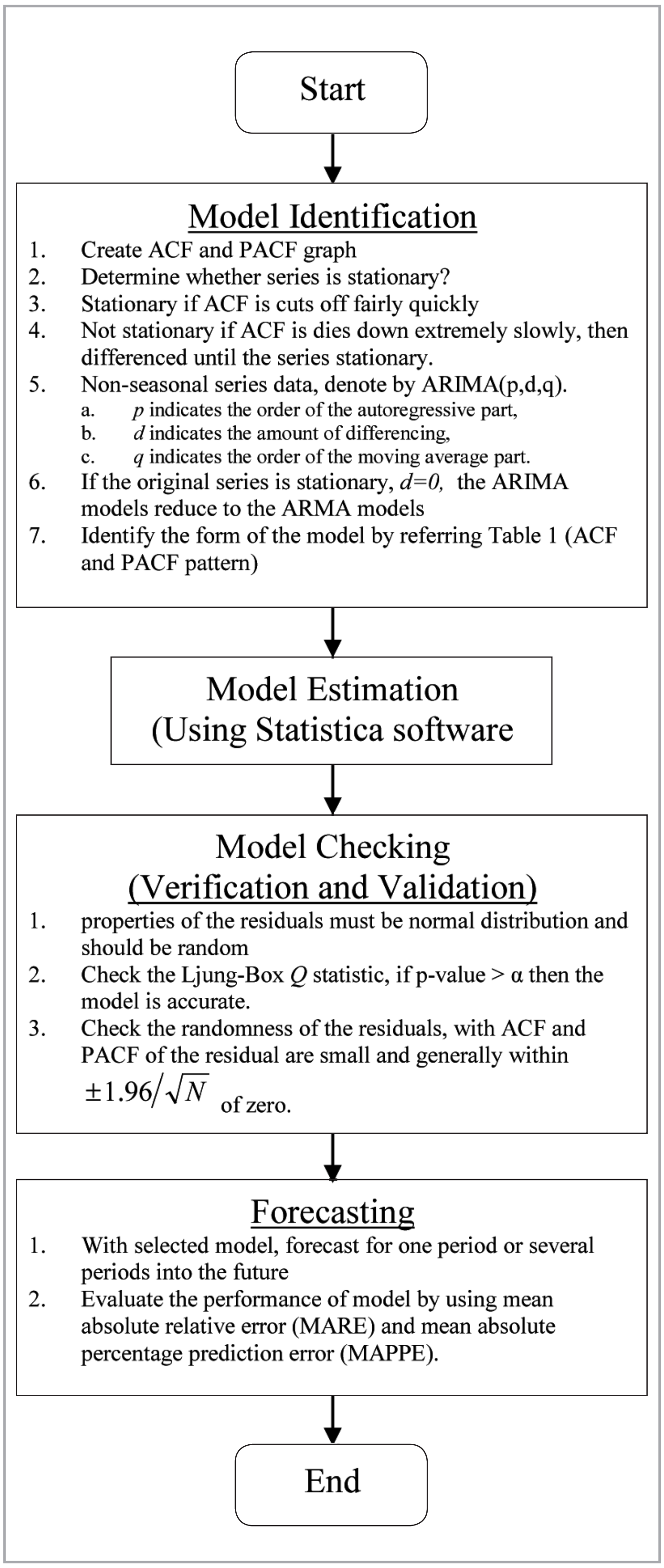

Figure 2: Location and scheduled departure of case study

Where,

ϕ_p = Coefficient to be estimated

B = Lag or backward linear operator defined by $BY_t = Y_t\text{-}1$.

W_t = Stationary series obtained as the d^{th} difference of Y_t, that is $W_t = (1\text{-}B)^d Y_t$

μ = Constant mean of the process

θ_q = Coefficient to be estimated

ε_t = Error term at time t

Second step is to identify the form of the model to be used by using the theory in Table 1, after a stationary series has been obtained.

5.2.2 Model Estimation

Estimate the parameters for a tentative model has been selected.

5.2.3 Model Checking (Verification and Validation)

In this step, model must be checked for adequacy or accuracy by considering the properties of the residuals whether the residuals from an ARIMA model must has the normal distribution and should be random. An overall check of model adequacy is provided by the Ljung-Box Q statistic.

If the p-value associated with the Q statistic is small (p-value $< \alpha$), the model is considered inadequate. The analyst should consider a new or modified model and continue the analysis until a satisfactory model has been determined.

Moreover, it can be checked that the properties of the residual with the graph as follows:

1) Check the normality by considering the normal probability plot or the p-value from the One-Sample Kolmogorov – Smirnov Test.
2) Check the randomness of the residuals by considering the graph of ACF and PACF of the residual. The individual residual autocorrelation should be small and generally within $\pm 1.96/\sqrt{N}$ of zero.

5.2.4 Forecasting with the Model

Forecasts for one period or several periods into the future with the parameters for a tentative model have been selected. Evaluation of forecasting was performed by using mean absolute relative error (MARE) and mean absolute percentage prediction error (MAPPE).

6.0 RESULTS AND DISCUSSION

The results obtained and finding models are presented in the following sub-sections.

6.1 Graphical Data Presentation

Data for analysis were series data of bus travel time collected from January to December 2007. Observation was done for two typical days, workday and weekend each month. The

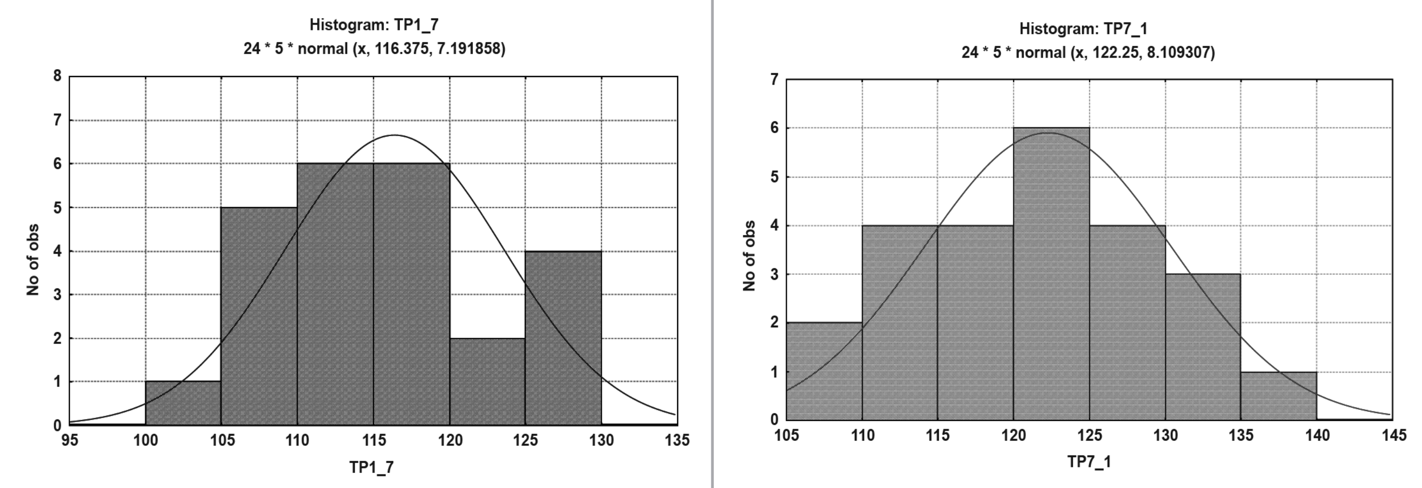

(a) From Ipoh (TP=1) to Lumut (TP=7)

(b) From Lumut (TP=7) to Ipoh (TP=1)

Figure 3: Histogram and normal distribution of bus travel time

unit of travel time is measured in minute, thus, unit of minute is consistently used in the discussion. Descriptive statistics of bus travel time series was summarised in Table 2. From the Figure 3, it was shown that the distribution of travel time met with normal distribution $N(x, 116.38, 7.192)$ for Ipoh to Lumut direction (from time point TP=1 to time point TP=7). Meanwhile, for the opposite direction, Lumut to Ipoh, the normal distribution fitting was $N(x, 122.25, 8.109)$. The difference of average travel time of both directions is 5.9 minutes (5% difference). This is due to the operating speed for Lumut to Ipoh direction is lower (40km/h) with the higher variation of travel time (6.6%) compared to those of Ipoh to Lumut direction. For Ipoh to Lumut direction, the operating speed and variation of travel time are 43 km/h and 6.1%, respectively.

Table 2: Descriptive statistics of bus travel time (ARIMA_TT)

	TP1_7 : ***Travel time from TP=1 to TP=7***	***TP7_1 :*** ***Travel time from TP=7 to TP=1***
Mean	116.375	122.25
Std.Dv.	7.191858	8.109308
Minimum	102	110
Maximum	129	139
First	1	1
Last	24	24
N	24	24

Based on the Box & Whisker plot (See Figure 4), for both directions, the standard deviation and standard error of travel time changed increasing as the distance traveled increased from the starting time point to the downstream time points. The standard deviation plot, for instance, between time points of 1_2, 1_3, 1_4, 1_5, 1_6 and 1_7 tended to increase because there was delay propagation due to various traffic conditions and bus operating speed. The same changes were experienced for other pairs of time points.

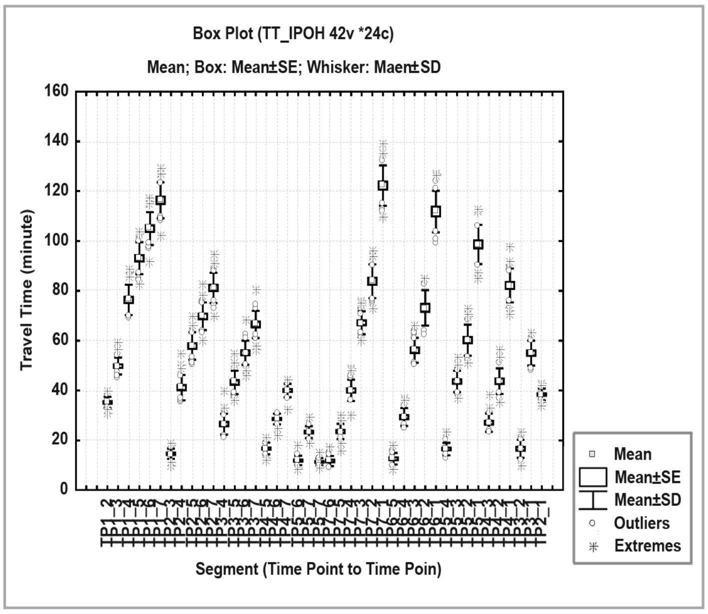

Figure 4: Standard deviation and standard error of bus travel time

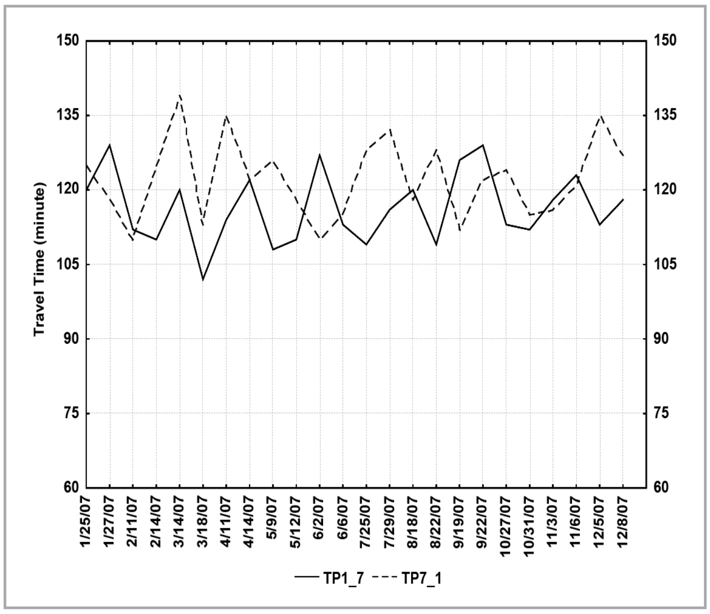

Figure 5: Time series plot of the bus travel time

6.2 The Aart of ARIMA Model Building and Forecasting

By following of the steps in the models-building, the results can be obtained, as shown in Figures 3-5. The time series data are considered stationary at around the mean value. Most of the autocorrelation values are smaller than 1.96 times their standard errors (*i.e*., the probability of 95% confidence limit) as indicated by the dotted line in the ACF plot in Figure 4 and 5. The time series is stationary because the graph of ACF of the time series values either cuts off fairly quickly or dies down fairly quickly. Thus, it was not necessary to make transformation and differencing of the data, in this case *d*=0. To build the proper model, it was reasonable to applied some tentative ARIMA models for Ipoh to Lumut direction such as, ARIMA(0,0,1), ARIMA(0,0,2), ARIMA(1,0,0) and ARIMA(2,0,0). And, for the Lumut to Ipoh direction, the tentative models considered were as follows: ARIMA(0,0,1), ARIMA(0,0,2), ARIMA(1,0,0), and ARIMA(2,0,0).

Table 3 shows the estimated parameters of selected model of bus travel time prediction. Parameter estimation in ARIMA models is completely achieved by maximising the likelihood (probability) of the data. The method for computing maximum likelihood value for ARIMA is Exact (Melard algorithm) [11]. For Ipoh to Lumut direction (from TP=1 to TP=7), the model was without transformation (the amount of difference, *d*=0), named ARIMA(0,0,2) = MA(2) with MS Residual = 46.722. Furthermore, the model for Lumut to Ipoh direction (from TP=7 to TP=1) is ARIMA(0,0,1) = MA(1) with MS Residual = 68.102.

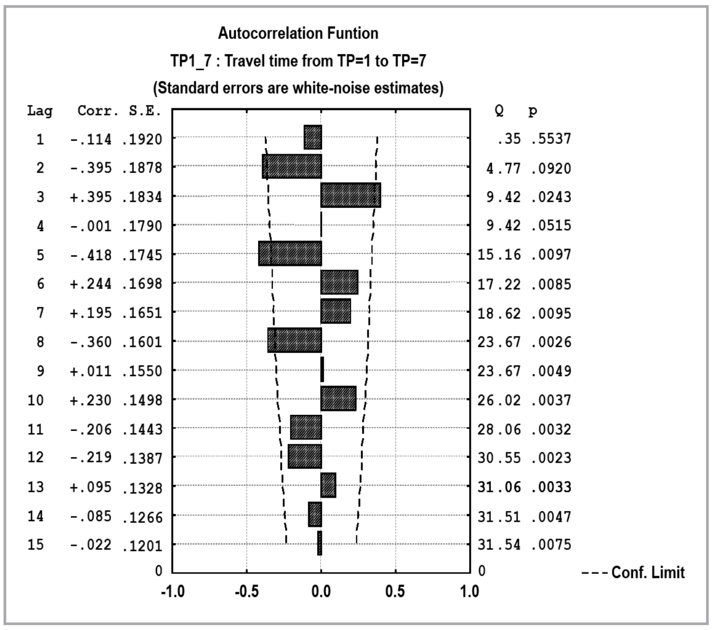

Figure 6: ACF of the bus travel time

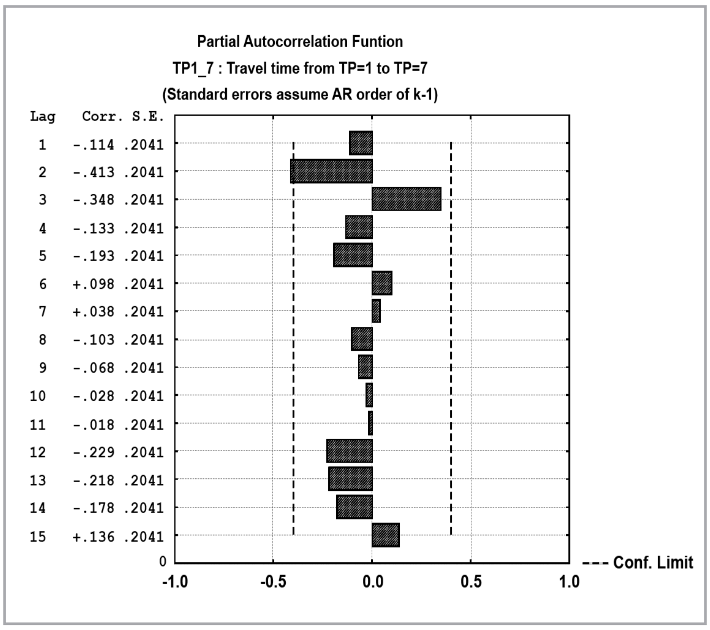

Figure 7: PACF of the bus travel time

For the Ipoh-Lumut corridor, the fitted models are formed as follows:

a) Ipoh to Lumut direction:
$Y_t = 116.1627 + 0.0447*\varepsilon_{t-1} - 0.4289*\varepsilon_{t-2}$ (5)

b) Lumut to Ipoh direction:
$Y_t = 122.2072 - 0.1218*\varepsilon_{t-1}$ (6)

More details, all the tentative ARIMA models were shown below. Based on the estimated model parameters of respective bus travel time resulted by using STATISTICA 7 software, it could be obtained the models in the form as the following in Table 4.

Table 3: Estimated mode parameters of bus travel time

Input: TP1_7 : Travel time from TP=1 to TP=7 (ARIMA_TT) Transformations: none Model:(0,0,2) MS Residual= 46.722						
	Param.	***Asympt.Std.Err.***	***Asympt.t(21)***	***p***	***Lower 95% Conf***	***Upper 95% Conf***
Constant	116.1627	0.9341	124.3513	0.0000	114.2200	118.1053
q(1)	-0.0447	0.2039	-0.2191	0.8287	-0.4687	0.3794
q(2)	0.4289	0.1885	2.2757	0.0335	0.0370	0.8208
Input: TP7_1 : Travel time from TP=7 to TP=1 (ARIMA_TT) Transformations: none Model:(0,0,1) MS Residual= 68.102						
	Param.	***Asympt.Std.Err.***	***Asympt.t(22)***	***p***	***Lower 95% Conf***	***Upper 95% Conf***
Constant	122.2072	1.5267	80.0476	0.0000	119.0411	125.3734
q(1)	0.1218	0.2855	0.4266	0.6738	-0.4703	0.7139

Table 4: Model results of bus travel time

Models	***Equations***	***Note***
1. *For Ipoh to Lumut direction:*		
a) ARIMA(0,0,1) = MA(1)	$Y_t = 116.2890 - 0.2602*\varepsilon t\text{-}1$	1st-order moving average
b) ARIMA(0,0,2) = MA(2)	$\mathbf{Y_t = 116.1627 + 0.0447*\varepsilon_{t-1} - 0.4289*\varepsilon_{t-2}}$	**2nd-order moving average**
c) ARIMA(1,0,0) = AR(1)	$Y_t = 116.3530 - 0.1107*Y_{t-1}$	1st-order autoregressive
d) ARIMA(2,0,0) = AR(2)	$Y_t = 116.1699 - 0.1828*Y_{t-1} - 0.4606*Y_{t-2}$	2nd-order autoregressive
2. *For Lumut to Ipoh direction:*		
a) ARIMA(0,0,1) = MA(1)	$\mathbf{Y_t = 122.2072 - 0.1218*\varepsilon_{t-1}}$	**1st-order moving average**
b) ARIMA(0,0,2) = MA(2)	$Y_t = 121.9329 - 0.5090*\varepsilon_{t-1} - 0.4910*\varepsilon_{t-2}$	2nd-order moving average
c) ARIMA(1,0,0) = AR(1)	$Y_t = 122.2269 - 0.0794*Y_{t-1}$	1st-order autoregressive
d) ARIMA(2,0,0) = AR(2)	$Y_t = 122.1416 - 0.0979*Y_{t-1} - 0.1519*Y_{t-2}$	2nd-order autoregressive

From Figure 8-10, proof that the selected ARIMA(0,0,2) or MA(2) is an appropriate model for bus travel time from Ipoh to Lumut direction, and is better than other tentative ARIMA models. Similarly, by using the other graph for Lumut to Ipoh direction it can be obtained the ARIMA(0,0,1) or MA(1) which is proper model for bus travel time in the case.

The models were checked for accuracy by considering the properties of the residuals whether the residuals from an ARIMA model has the normal distribution and should be random. For overall, as shown in Figure 9, the models are considered adequate as the p-value of associated with the *Ljung-Box Q* statistic is large (p-value > α).

The equation of the final result can be used to approximately generate the historical patterns of bus travel time in a time series and forecast the future value of the time series of bus travel time.

From Figure 8, the histogram shows that it looks like the residuals are normally distributed. Apparently, it seems how well the normal distribution fits the actual distribution of residuals. Moreover, it can be checked the properties (randomness) of the residuals with the graph of ACF and PACF of the residual (See Figure 9-10). The individual residual autocorrelation was small and generally falling within limit $\pm 1.96/\sqrt{N}$ of zero (there is no residual serial correlation). In other words, the residuals are independent of each other as second criteria of ARIMA models.

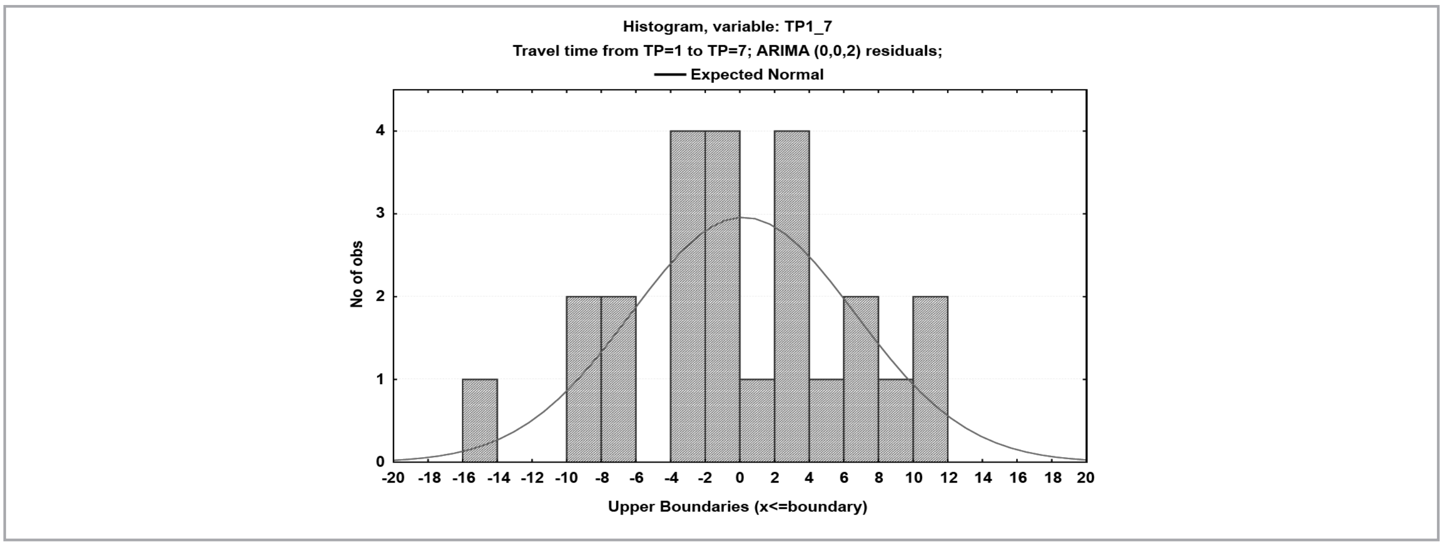

Figure 8: Histogram of the residuals of the bus travel time

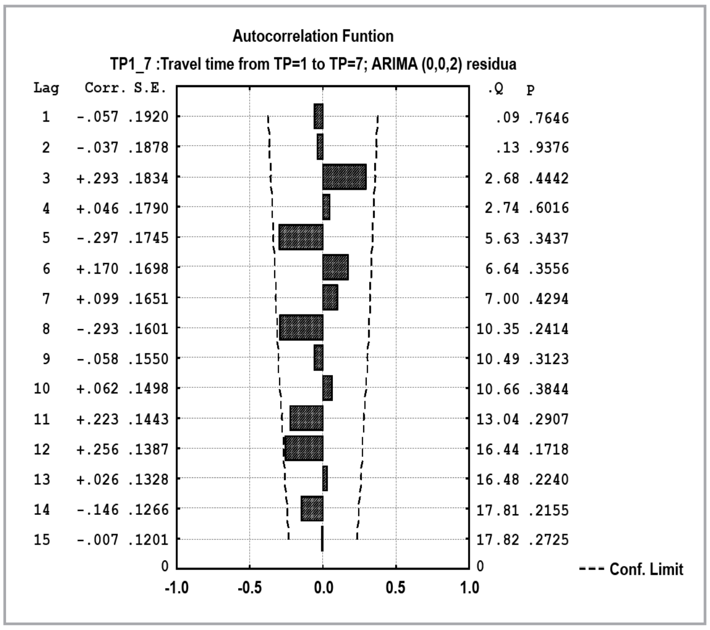

Figure 9: ACF of the residuals of the bus travel time

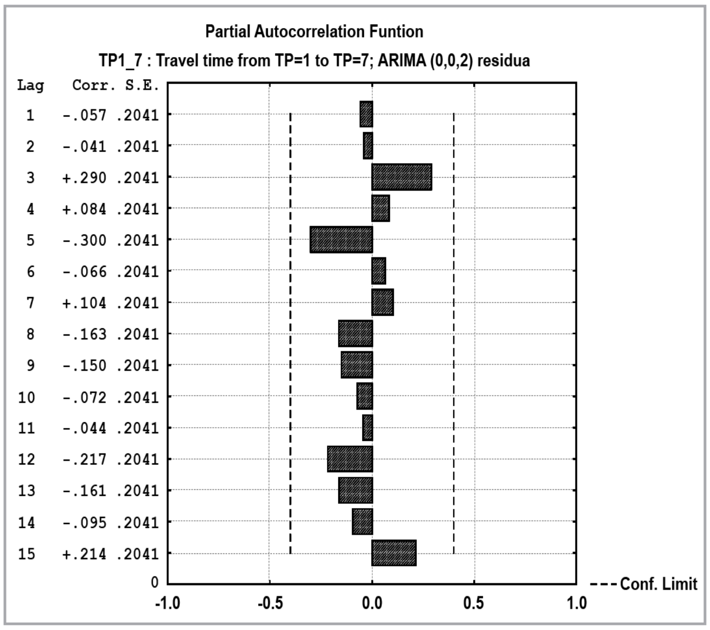

Figure 10: PACF of the residuals of the bus travel time

7.0 APPLICATION OF BUS TRAVEL TIME PREDICTION

Data set used for prediction (validation) consists of data set for model estimation and being added with any observed data else.

The performance of model is measured by the degree of accuracy. Accuracy of the model is indicated by statistical closeness such as mean absolute relative error (MARE) and mean absolute percentage predicting error (MAPPE). Both are indicator of model performance. The model which has minimum value of MARE and MAPPE is the accurate model (the best) among the several tentative models in predicting bus travel time. In other word, the minimum residual (error) indicate high accuracy model.

In this application, the prediction of bus travel time with the model obtained is properly done by considering the value of MARE (mean absolute relative error) and MAPPE (mean absolute percentage prediction error). Performance of models was measured by calculating MARE and MAPPE for each tentative models as being formulated:

$$\text{MARE} = \frac{\sum_{i-1}^{n} \left| ActualValue_i - ForecastValue_i \right|}{n} \tag{7}$$

$$\text{MAPPE} = \frac{\sum_{i-1}^{n} \left| \dfrac{ActualValue_i - ForecastValue_i}{ActualValue_i} \right|}{n} \tag{8}$$

where,
n : number of cases or data points
MARE in respective unit of minute
MAPPE is measured in %

The proper model is determined by comparing the MARE and MAPPE values among the tentative models as indicated by the minimum value of MARE and MAPPE. Table 5 shows the MARE and MAPPE values. ARIMA(0,0,2) = MA(2) and ARIMA(0,0,1) = MA(1) are selected because of the smallest MARE and MAPPE values.

The MA(2) and MA(1) equations can be used to approximately generate the historical patterns of bus travel time in a time series and forecast the future value of the time series of bus travel time. For instant, the residual of travel time of 10% was tolerable, therefore, the route distance of 82.6 km which was traveled in a round trip within 240 minutes (4 hours), then the delay would likely being 24 minutes. The assumption of delay of 10% travel time seemed still reasonable for the regular stage bus which traditionally operated in mixed traffic. Meanwhile, for bus rapid transit (BRT) system generally concern with delay of 5 minutes which was tolerable.

In this case, both the model results could describe well the historical pattern of bus travel time with the minimum MAPPE values less than 10% (See Table 5). On the other hand, the delay as indicated by MARE values, both 4.44 and 6.77 minutes, were quite tolerable because those were not significant delay compared to the bus travel time of 117 and 123 minutes, respectively.

Predicted and actual (observed) bus travel times were plotted with 95% confidence limit in Figure 11-12. It was clearly shown that the bus travel time series vary stationary in mean value of 116.38 minutes for Ipoh to Lumut direction. Similarly, it varies in mean value of 122.25 minutes for Lumut to Ipoh direction. For both directions, there is no trend or linear relation between date and month of the year and bus travel time series. Most of data and predicted travel time for both Ipoh to Lumut and Lumut to Ipoh direction fell within 95% confidence limit, meaning that the models are reasonable and acceptable.

As shown in Figure 11-12, also, the forecasting results indicated that there was no specific trend line showing the changes of bus travel time in the following period. In the following period, the average travel time for both directions would be 117 and 123 minutes, respectively.

The prediction was only based on the historical travel time data, other factors, like as road and traffic conditions were not considered. As well known, the upgrading of the existing highway to be divided 4-lane 2-way highway in this corridor was done from middle of 2006 and finished totally in September 2007. The traffic volume might change from time to time before and after upgrading work. Those factors were not accounted to this study as the upgrading of road was done per segment while data was collected by on board survey. In addition, the mixed-traffic condition would be varies per segment along the corridor regarding the constructing work.

Table 5: Residual analysis and performance of models

Models	*MARE (minute)*	*MAPPE (%)*
1. Ipoh to Lumut Direction:		
a) ARIMA(0,0,1) = MA(1)	5.74	4.67
b) ARIMA(0,0,2) = MA(2)	4.44	3.88
c) ARIMA(1,0,0) = AR(1)	12.83	10.30
d) ARIMA(2,0,0) = AR(2)	74.34	64.24
2. Lumut to Ipoh Direction:		
a) ARIMA(0,0,1) = MA(1)	6.77	5.64
b) ARIMA(0,0,2) = MA(2)	7.86	6.42
c) ARIMA(1,0,0) = AR(1)	10.10	8.06
d) ARIMA(2,0,0) = AR(2)	30.56	24.66

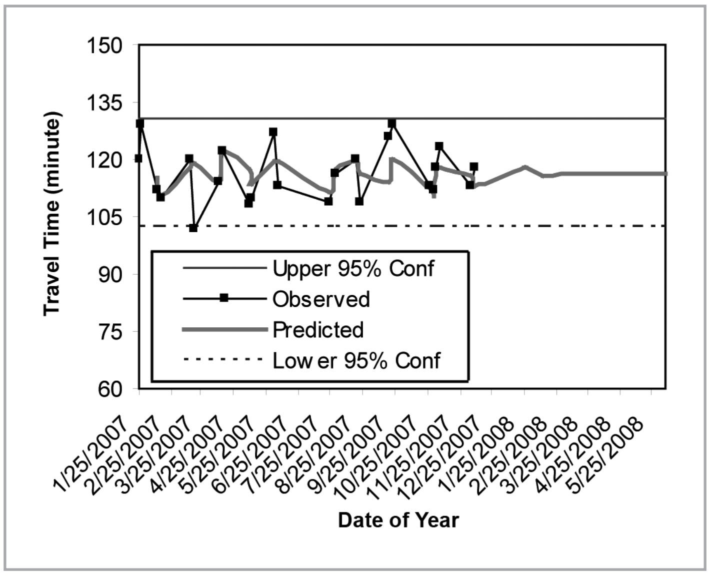

Figure 11: Travel time prediction (Ipoh to Lumut direction)

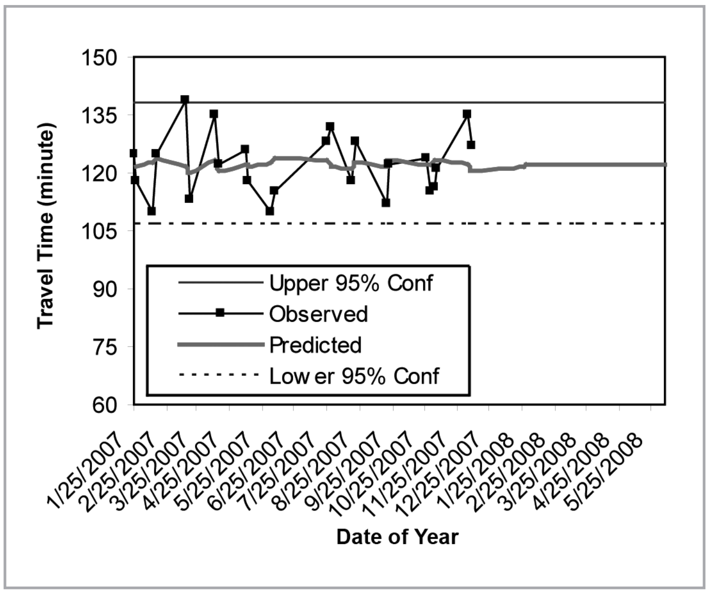

Figure 12: Travel time prediction (Ipoh to Lumut direction)

8.0 CONCLUSION

The results show that the predicted travel times by using the moving average model, MA(2) and MA(1) are close to the observed values. Those are indicated by the MARE and MAPPE values. The moving average models obtained had minimum MARE and MAPPE values compared to other tentative ARIMA models which being assessed. Those mean that MA(2) and MA(1) models are appropriate to be applied for the bus travel time prediction for Ipoh to Lumut and Lumut to Ipoh direction, respectively. And, those models can be used for bus travel time prediction in the case and they were statistical acceptable to be used in timetable design.

9.0 ACKNOWLEDGMENT

The author would thank to the Perak Roadways Sdn. Bhd. for the help to facilitate on conducting the on board survey during data collection. A good appreciation is awarded to the anonymous reviewer for their valuable suggestion on the previous manuscript. And, many thanks are delivered to Universiti Teknologi PETRONAS for the facilities provided and financial support in this research. ■

REFERENCES

[1] Peat, Marwick, Mitchell, and Co., *Transportation SystemsEvaluation Indicators*, U.S. DOT, Washington, DC., 1973.

[2] Khisty, C.J, and Lall, B.K., *Transportation Engineering: An Introduction*, 3rd edition, pp. 464-466, Prentice Hall, New Jersey, 2003.

[3] Dailey, D.J., Wall, Z.R., Maclean, S.D., and Cathey, F.W., "An Algorithm and Implementation to Predict the Arrival of Transit Vehicles", *Intelligent Transportation Systems Conference Proceeding*, Michigan, IEEE, pp. 161-166, 2000.

[4] Dailey, D.J., and Cathey, F.W., "Transit Vehicles as Traffic Probe Sensors", *Transportation Research Board*, 81st Annual Meeting, Washington, D.C., 2002.

[5] Abdelfattah, A.M., and Khan, A.M., "Models for Predicting Bus Delay", *Transportation Research Record 1623*, Transportation Research Board, 1998.

[6] Park, D., Rilett, L.R., and Han, G., "Spectral Basis Neural Networks for Real-Time Travel Time Forecasting", *Journal of Transportation Engineering*, pp. 515-523, 1995.

[7] Chien, I.J., and Kuchipudi, C.M., "Dynamic Travel Time Prediction with Real-Time and Historical Data, *Transportation Research Board*, Washington, D.C., 2002.

[8] Rajat Rajbhandari, *Bus Arrival Time Prediction Using Stochastic Time Series and Markov Chains*, Dissertation, pp. 5-56, January 2005.

[9] Box, G.E.P., and Jenkins, G.M., *Time Series Analysis: Forecasting and Control*, Holden-Day, San Francisco, California, 1970.

[10] Day, R.A., *How to Write and Publish a Scientific Paper*, 3rd edition, Oryx Press, Canada, 1988.

[11] StatSoft, Inc., *STATISTICA (data analysis software system)*, version 7, www.statsoft.com, 2004. Retrieved on 5 January 2009.

PROFILES

SUWARDO
Currently, he is pursuing PhD in Transportation Engineering and Traffic, Civil Engineering Department, Universiti Teknologi PETRONAS, Bandar Seri Iskandar, 31750 Tronoh, Perak Darul Ridzuan, Malaysia.
Tel: +6053688191, Fax: +6053654090.
E-mail: suwardo@yahoo.com
or suwardo@utp.edu.my

His permanent address is Civil Engineering Department, Faculty of Engineering, Gadjah Mada University. Jl. Yacaranda 1, Sekip, Yogyakarta 55281, Indonesia. Tel: +622747112126, Fax: +62274545193

He received his certificate of education and B. Eng in Civil Engineering (Teknik Transportation) from Gadjah Mada University in 1996. He obtained his M.Sc. (Magister Teknik, Rekayasa Transportasi) from Bandung Institute of Technology in 2001. His field of study and the research interest are in urban transportation engineering, public transport, transport project evaluation, traffic engineering, and road safety engineering. He is involved in professional association such as member of Inter-University Transportation Study Forum (FSTPT, Forum Studi Transportasi Perguruan Tinggi), member of Indonesian Road Development Association (HPJI, Himpunan Pengembangan Jalan Indonesia), member of Masyarakat Transportasi Indonesia (MTI), member of Eastern Asian Society for Transportation Studies (EASTS).

MADZLAN B NAPIAH
His current address is Civil Engineering Department, Universiti Teknologi PETRONAS, Bandar Seri Iskandar, 31750 Tronoh, Perak Darul Ridzuan, Malaysia. His academic experience is as follow:

- Doctor of Philosophy, University of Leeds
- Masters of Science (Engineering), University of Leeds
- Bachelor of Science, Michigan State University

Areas of specialization:
Highway and Transport Planning Engineering
Tel: +605-3687281
E-mail: madzlan_napiah@petronas.com.my

IBRAHIM B KAMARUDDIN
His current address is Civil Engineering Department, Universiti Teknologi PETRONAS, Bandar Seri Iskandar, 31750 Tronoh, Perak Darul Ridzuan, Malaysia.
His academic experience is:

- Doctor of Philosophy, University of Leeds
- Masters of Science in Civil Engineering, Louisiana State University
- Bachelor of Science, University of Sussex

Areas of specialization: Highway and Transportation
Tel: +605-3688585
E-mail: ibrakam@petronas.com.my

PENGESANAN KEROSAKAN DALAM RANGKAIAN FTTH DENGAN KEUPAYAAN PEMPROSESAN GUI PERISIAN MATLAB

(Date received: 31.7.2008)

Ng Boon Chuan[1] dan Mohammad Syuhaimi Ab-Rahman[2]
Jabatan Kejuruteraan Elektrik, Elektronik dan Sistem, Fakulti Kejuruteraan dan Alam Bina,
Universiti Kebangsaan Malaysia, 43600 UKM Bangi, Selangor
E-mail: [1]ngbc@vlsi.eng.ukm.my, [2]syuhaimi@vlsi.eng.ukm.my

ABSTRAK

Kajian ini menekankan pembangunan antaramuka pengguna bergrafik (GUI) untuk Sistem Pengesanan Kerosakan Terpusat (CFDS) dengan menggunakan perisian MATLAB untuk meningkatkan keberkesanan, kelengkapan dan keboleharapan rangkaian capaian gentian ke rumah (FTTH). Program yang dibangunkan ini akan ditempatkan di pejabat pusat (CO) untuk memantau setiap talian penghantaran dan mengesan kerosakan yang berlaku dalam sistem rangkaian tersebut secara terpusat. Peralatan OTDR (Optical Time Domain Reflectometer) digunakan dalam proses menganalisa pengecilan (kehilangan) gentian optik. CFDS akan berantaramuka dengan OTDR untuk mengumpulkan semua hasil pengukuran OTDR dan menghasilkan multi paparan pada suatu masa untuk pemantauan secara terpusat. Program yang dibangunkan ini akan mempersembahkan visualisasi bergrafik dan parameter-parameter setiap talian optik termasuk kuasa optik, kehilangan, pengecilan yang berlaku dalam rangkaian tersebut berserta dengan lokasi elemen yang mendorong pengecilan kuasa tersebut dan maklumat-maklumat lain seperti mana yang terpapar pada skrin OTDR. Dengan ini, sebarang kerosakan yang berlaku dalam sistem rangkaian boleh dikesan dan ditentukan dengan kehilangan kuasa optik yang mendadak. Seterusnya status dan maklumat kerosakan dalam sistem rangkaian tersebut akan dihantar kepada jurutera tapak melalui teknologi wayarles untuk mengambil tindakan yang sewajar.

Keywords: *CFDS, GUI, OTDR, Pemantauan Secara Terpusat, Visualisasi Bergrafik*

ABSTRACT

This paper highlights on the graphical user interface (GUI) development for Centralized Failure Detection System (CFDS) by using MATLAB software to increase the efficiency, survivability, and reliability of fibre-to-the-home (FTTH) access network. The developed program will be installed at the central office (CO) to centralised monitor each fibre transmission link and detect the failure location. Optical time domain reflectometer (OTDR) is used to analyze the attenuation (light loss) in an optical fibre. CFDS is interfaced with the OTDR to accumulate every network testing result to be displayed on a single computer screen for centralised monitoring and advanced analyzing. The developed program will provide the graphical visualization and present the parameters of each transmission link such as the optical power level, losses, fibre attenuation, and other details as shown in the OTDR's screen. By monitoring such parameters, any occurrence of fault in the network system can be identified by a drastic drop of optical power level. The analysis results will be sent to the field engineers through the mobile phone using wireless technology for promptly actions.

Keywords: *CFDS, GUI, OTDR, Centralized Monitoring, Graphical Visualisation*

1.0 PENGENALAN

Rangkaian FTTH merupakan teknologi rangkaian yang menggunakan gentian optik sebagai medium penghantaran dari CO sehingga ke kawasan perumahan atau perniagaan untuk membekalkan perkhidmatan *Triple-play* (data, suara dan video). Rangkaian FTTH memainkan peranan yang penting dalam mengurangkan dan menyelesaikan masalah *Bottleneck* capaian terakhir dalam rangkaian capaian lebar jalur khususnya rangkaian capaian optik generasi depan [1]. Dengan gentian optik yang mempunyai lebar jalur yang sangat tinggi, rangkaian FTTH mampu menghantar data dengan keupayaaan yang lebih besar berbanding dengan teknologi yang berdasarkan kabel kuprum [2]. Kini, rangkaian FTTH telah diiktiraf sebagai penyelesaian terbaru bagi pelbagai jenis perkhidmatan komunikasi dan multimedia termasuk telefon, capaian Internet berkelajuan tinggi, televisyen kabel digital (CATV) dan video [3].

Penyambungan dalam rangkaian FTTH khususnya senibina rangkaian optik pasif (PON) merupakan media perkongsian di mana terminal talian optik (OLT) dihubungkan kepada banyak unit rangkaian optik (ONU) atau terminal rangkaian optik (ONT) (yang ditempatkan pada kediaman-kediaman premis pengguna yang berbeza) melalui pencerai optik pasif (*Passive Optical Splitter*) di RN (*Remote Node*) seperti ditunjukkan dalam Rajah 1.

Rangkaian PON dapat diakomodasikan kepada bilangan premis pengguna yang ramai dengan menggunakan peranti pembahagi kuasa optik seperti pengganding optik (*Optical Coupler*) atau pencerai optik pasif (*Passive Optical Splitter*) untuk berkongsi satu gentian suapan (*Feeder Fibre*). Pencerai optik 1x*N* digunakan untuk membahagikan lebar jalur sesuatu gentian di kalangan 16/32/64/128 orang pengguna dengan jarak maksimum yang dibenarkan antara OLT dengan ONU/ONT ialah 20 km.

Isu-isu berkenaan dengan kualiti perkhidmatan rangkaian FTTH sering menjadi perdebatan sejak kebelakangan ini. Antara isu-isu penting yang diketengahkan pengendali-pengendali perkhidmatan dan premis-premis pengguna adalah berhubung dengan keboleharapan perkhidmatan dan kerosakan talian gentian optik. Apabila salah satu titik dalam sesuatu gentian terputus, terutamanya gentian suapan (*Feeder Fiber*) di kawasan suapan (*Feeder Region*), sebarang penghantaran perkhidmatan selepas titik kerosakan (*Break Point*) akan diberhentikan. Isyarat laluan menaik (*Upstream*) atau laluan menurun (*Downstream*) yang dihantar dari ONU/ONT ke OLT atau sebaliknya tidak akan disampaikan [4]. Sebarang kegagalan penghantaran yang berpunca daripada kerosakan talian optik akan mengakibatkan kerugian yang besar kepada pengendali-pengendali perkhidmatan dan juga premis-premis pengguna [5-6].

Sistem komunuikasi optik biasa menggunakan diod laser semikonduktor sebagai sumber optik. Jenis diod tersebut bermonokromat tinggi dan pancarannya sangat bertumpu berbanding dengan sumber laser lain seperti gas laser [2]. Walaupun laser yang berkuasa rendah dengan beberapa miliwatt digunakan dalam pemancaran, tetapi radiasi tersebut adalah sangat membahayakan penglihatan dan kulit manusia apabila ia terdedah kepada persekitaran (Keadaan ini berlaku apabila kabel talian optik terputus dari rangkaian FTTH). Jika mata terkena pancaran laser daripada pemantulan semula jadi, pancaran laser akan memasuki mata dan tertumpu pada retina mata. Cahaya laser boleh mengakibatkan mata seseorang yang terdedah kepadanya rosak kekal (buta) dalam sesaat atau lebih pantas. Di samping itu, cahaya yang terserap akan ditukar kepada bentuk haba dan mengakibatkan pembakaran kulit serta kerosakan tisu-tisu biologi dalam badan manusia.

Pengesanan kerosakan talian optik dalam rangkaian FTTH adalah penting demi meningkatkan keboleharapan penghantaran dan keselamatan perkhidmatan [7]. Peralatan OTDR lazim digunakan untuk mengesan kerosakan yang berlaku dalam talian gentian optik dalam halaan menaik (*Upward*), iaitu daripada ONU/ONT menuju ke OLT. Juruteknik akan dihantar ke kawasan premis pengguna untuk memasangkan OTDR kepada talian yang rosak untuk mengesan lokasi kerosakan apabila didapati ONU tidak berfungsi (seperti ditunjukkan dalam Rajah 1). Kaedah pengujian ini hanya sesuai digunakan sekiranya cuma terdapat satu pengguna sahaja gagal menerima perkhidmatan.

Pengesanan kerosakan talian optik dalam halaan menaik adalah tidak pratikal digunakan dalam rangkaian FTTH terutamanya dalam PON yang bertopologi pokok kerana ianya mempunyai bilangan premis pengguna yang ramai (banyak cabang / gentian guguran) dan liputan kawasan guguran (*Drop Region*) yang begitu luas. Keadaan ini amat membazirkan masa dan wang kerana jarak antara dua ONU/ONT adalah berjauhan. Walaubagaimanapun, pengesanan kerosakan talian tidak dapat dilakukan dalam halaan menurun (*Downward*), iaitu dari CO menuju ke premis pengguna, kerana terdapat elemen pembahagi kuasa, iaitu pencerai optik yang mengumpulkan semua cahaya sebaran balik Rayleigh (*Rayleigh Back-scattering, RBS*) bersama dari setiap cabang dalam kesan OTDR dan mengakibatkannya tidak dapat dibezakan secara berasingan [5].

2.0 SISTEM PENGESANAN KEROSAKAN TERPUSAT (CFDS)

Pemantauan dan pengesanan kerosakan talian optik adalah penting untuk meningkatkan keboleharapan perkhidmatan di samping mengurangkan kos dan masa penyelenggaraan rangkaian FTTH. Selain itu, proses pengesanan kerosakan perlu dijalankan tanpa menggangu perkhidmatan saluran lain untuk memaksimumkan penggunaan rangkaian [5, 8]. Justeru itu, CFDS yang mampu memantau status setiap talian optik dan mengesan kerosakan talian yang berlaku dalam kawasan guguran rangkaian FTTH secara terpusat pada CO dalam halaan menurun dibangunkan dalam kajian ini.

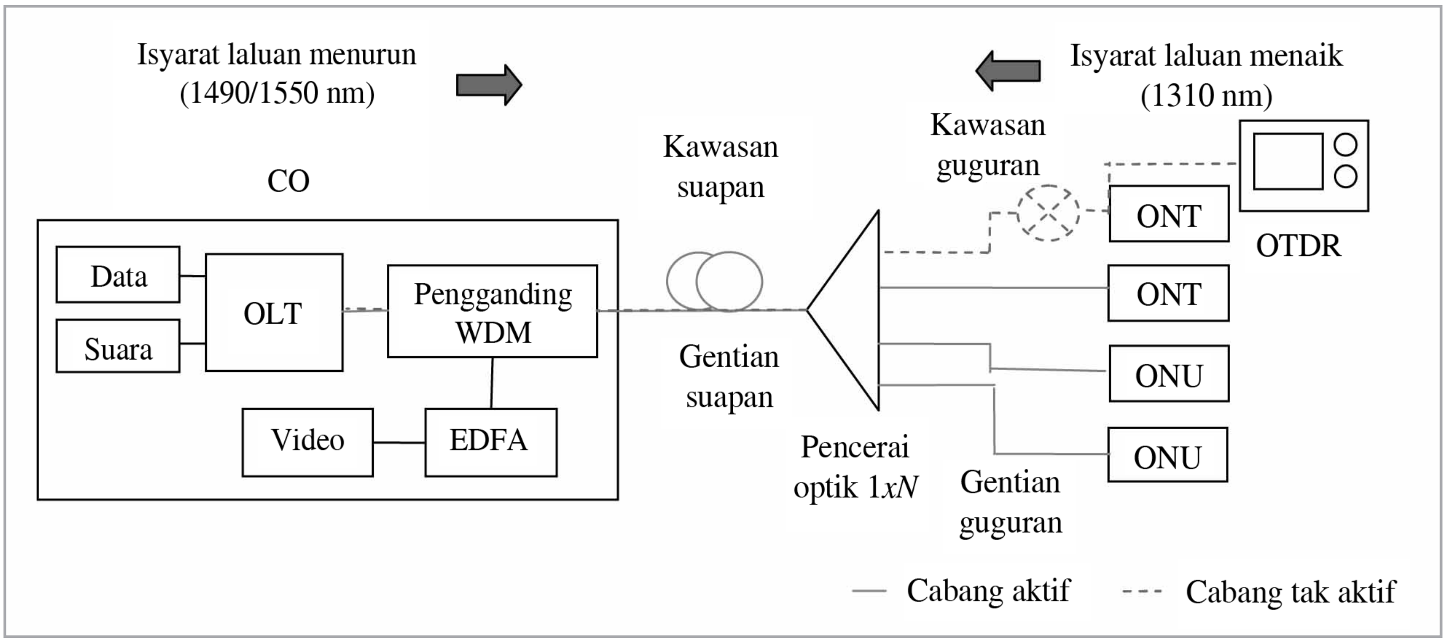

Rajah 1: Pengesanan kerosakan dalam rangakaian PON secara halaan menaik

CFDS merupakan satu program pemantauan terpusat dan kawalan capaian yang membolehkan pengendali perkhidmatan mengawasi aliran isyarat optik dan mengesankan kerosakan dengan keupayaan pemprosesan GUI perisian MATLAB. Program yang dibangunkan ini mempunyai pencirian-pencirian yang sama seperti OTDR dan *Computer-based Emulation Software* untuk pemprosesan paparan OTDR (*OTDR Trace*) yang lebih terperinci, tetapi lebih fleksibel dan boleharap digunakan dalam sistem komunikasi optik khususnya dalam pengujian rangkaian capaian FTTH.

2.1 Konsep Rekabentuk CFDS

Dalam skema cadangan ini, sebuah OTDR akan ditempatkan di CO dan disambungkan kepada sebuah komputer peribadi (PC) melalui sambungan liang sesiri (DB-9) untuk mempaparkan segala hasil pengukuran OTDR secara kawalan jauh. OTDR menggunakan panjang gelombang 1625 nm (dalam kawasan tetingkap keempat / *Fourth Window Region*) yang berasingan dengan panjang gelombang pengoperasian perkhidmatan *Triple-play* (1310 nm, 1490 nm dan 1550 nm) untuk pengujian talian gentian optik supaya tidak menggangu penghantaran perkhidmatan *Triple-play* dalam rangkaian FTTH. Prinsip pengoperasian CFDS terdiri daripada tiga bahagian utama, iaitu (a) Pengujian rangkaian optik dengan OTDR, (b) Pengantaramukaan CFDS dengan OTDR, dan (c) Pemantauan dan penganalisaan data secara terpusat. Seluruh proses pengoperasian CFDS diringkaskan dalam carta alir berikut.

Ketiga-tiga jenis isyarat perkhidmatan *Triple-play* (1310 nm, 1490 nm dan 1550 nm) dimultiplekskan bersama dengan 1625 nm isyarat pengujian OTDR di CO dengan menggunakan pengganding panjang gelombang terpilih (*Wavelength Selective Coupler,* WSC). Apabila keempat-empat panjang gelombang tersebut diagihkan dari CO kepada lapan premis pengguna, pengganding WSC hanya membenarkan isyarat 1625 nm memasuki litar pengetip (*Tapper Circuit*) dan menapiskan isyarat-isyarat lain (1310 nm, 1490 nm dan 1550 nm) yang boleh mengganggu hasil pengukuran OTDR [9]. Isyarat laluan menurun akan melalui WSC dan kemudian sampai di ONU. Jarak maksimum antara OLT dengan ONU adalah 20 km. Isyarat OTDR yang telah didemultiplekskan dengan WSC akan diceraikan lagi pada nisbah kuasa 99:1 dengan menggunakan pengganding berarah (*Directional Coupler*, DC) untuk mengaktifkan sistem pemproses mikro. 99% isyarat ini dikonfigurasikan dengan menggunakan pencerai optik, di mana setiap keluaran akan

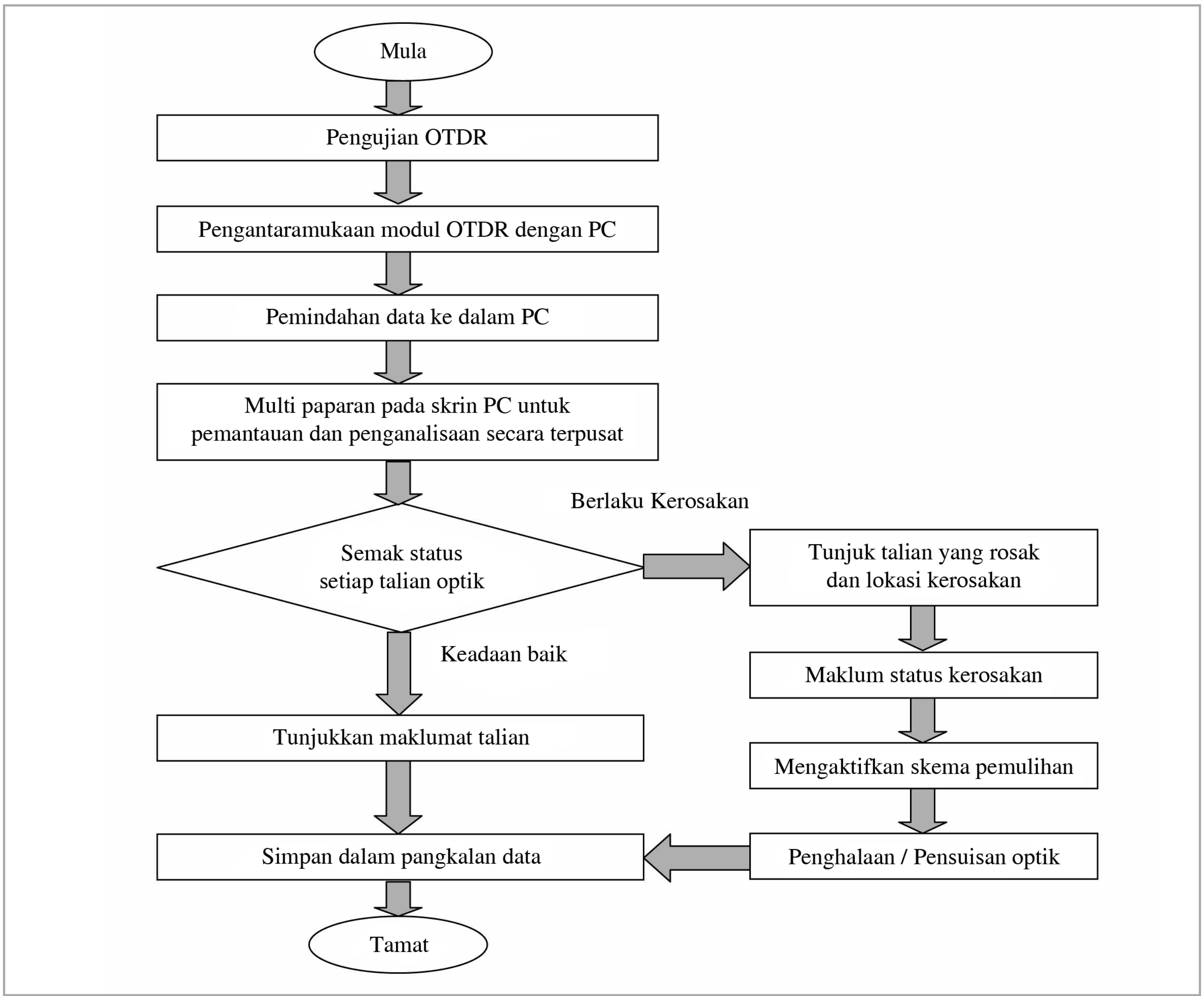

Rajah 2: Carta alir bagi mekanisme pengesanan kerosakan talian dalam rangkaian FTTH

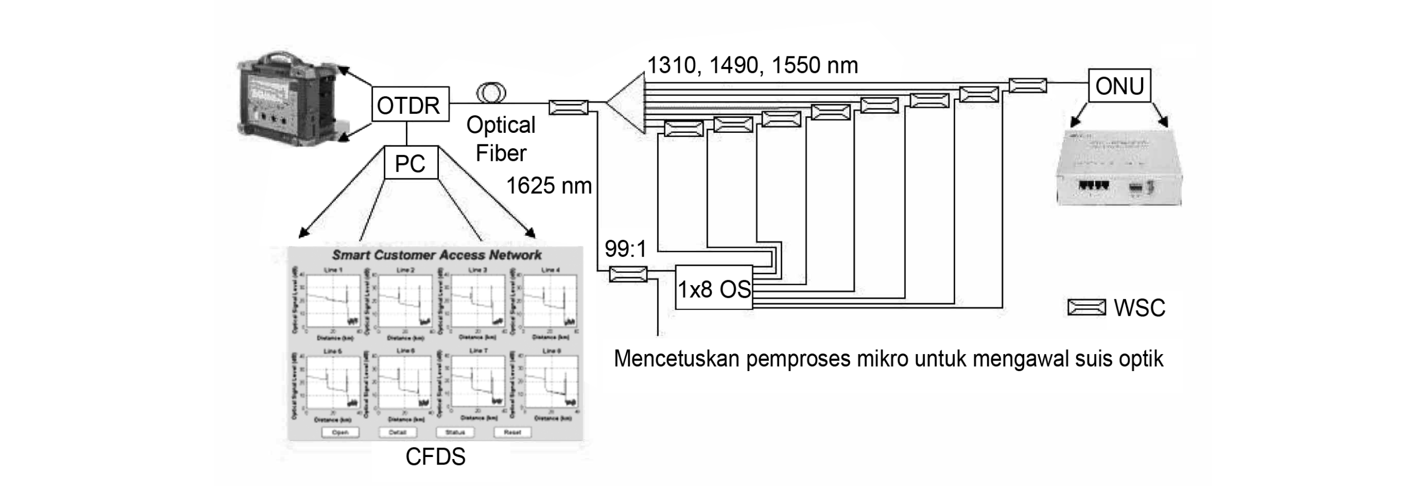

Rajah 3: Penyambungan suis optik kepada sistem pencerai dan pemproses mikro

disambungkan kepada satu ONU secara berasingan. Seterusnya pengoperasian suis optik akan dikawalkan oleh sistem pemproses mikro yang diaktifkan oleh 1% isyarat (seperti dalam Rajah 3).

2.2 Pengujian Rangkaian Optik

Pengujian rangkaian optik dijalankan pada peringkat permulaan untuk mengukur pencirian-pencirian talian optik dalam keadaan baik (bekerja / *Working Condition*) dan keadaan rosak (tidak bekerja / *Failure condition*) dengan rangkaian berikut. Peralatan *Optical Attenuator* digunakan sebagai DUT (*Device Under Test*) untuk mengurangkan aras kuasa optik atau mewakili titik kerosakan yang berlaku dalam talian optik yang diuji. Nilai pengecilan pada *Attenuator* ditetapkan pada 1 *dB* dan ditambahkan secara berkala sehingga mendapat isyarat OTDR yang menunjukkan kerosakan berlaku dalam talian optik yang diuji. Dalam pengujian ini, isyarat optik akan terputus ketika nilai pengecilan ditambahkan sehingga 8 *dB*. Ini menggambarkan talian optik terputus pada jarak (lokasi) tersebut dalam keadaan sebenar.

2.3 Pengantaramukaan CFDS dengan OTDR

CFDS berantaramuka dengan OTDR untuk mengumpulkan dan mempaparkan setiap hasil pengujian rangkaian (pengukuran OTDR) di atas satu skrin PC kawalan jauh (*Remote PC*) pada suatu masa untuk dianalisakan lagi. Hasil pengujian disimpan sebagai format TRC (*Trace*) dalam OTDR dan kemudian dipindahkan ke dalam komputer dengan menyambungkan liang sesiri DB-9 jantan (RS-232) pada OTDR dan PC dengan menggunakan kabel sambungan dua hujung DB-9 betina (*Serial Port Extension Cable*).

2.4 Penganalisaan Data dengan Menggunakan CFDS

Selepas proses pemindahan berjaya dilakukan, semua hasil pengujian perlu ditukarkan kepada format ASCII (*American Standard Code for Information Interchange*) seperti ditunjukkan dalam Rajah 5 dan kemudian disimpan dalam pangkalan data. Program yang dibangunkan ini akan mempersembahkan visualisasi bergrafik dan menganalisakan segala hasil pengujian yang diperolehi. CFDS menggunakan kaedah pengenalan kejadian (*Event Identification*) untuk membezakan mekanisme isyarat optik dalam keadaan baik dan keadaan rosak. Dalam kajian ini, kehilangan yang berlaku pada kejadian '*Reflective Fault*' akan mewakili status keadaan talian yang sedang diuji.

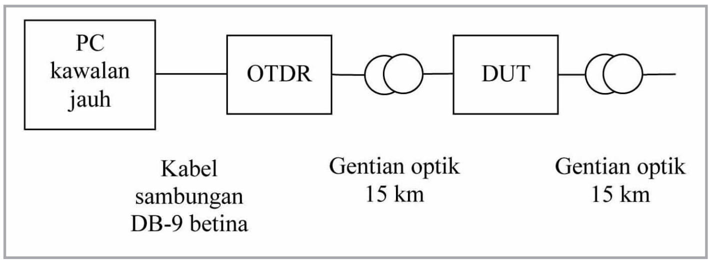

Rajah 4: Rajah blok bagi susunan perkakasan dalam pengujian rangkaian optik

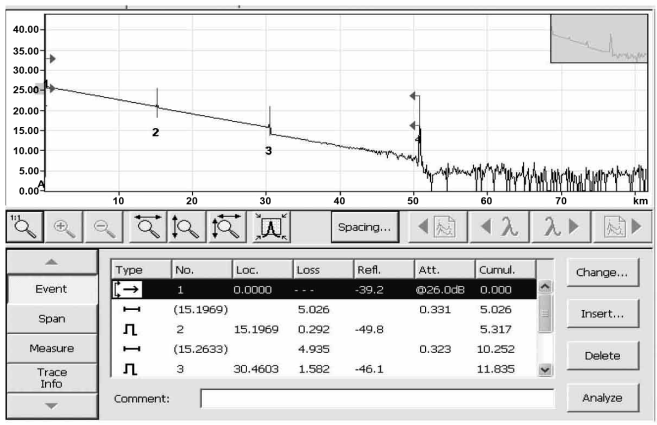

(a) Contoh fail TRC dalam Emulation Software

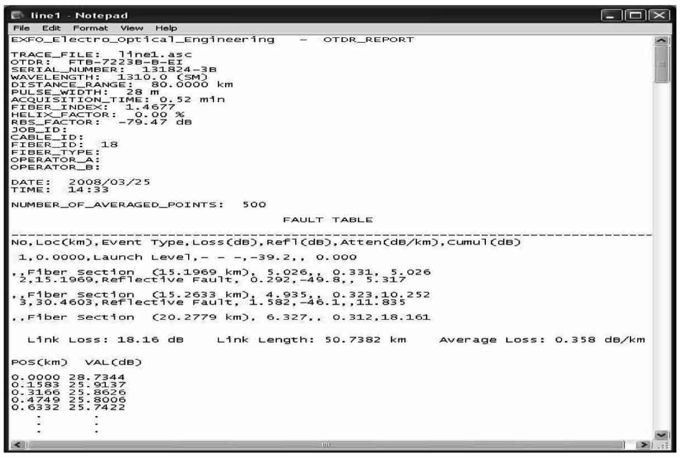

```
line1 - Notepad
File Edit Format View Help
EXFO_Electro_optical_Engineering    -   OTDR_REPORT

TRACE_FILE:   line1.asc
OTDR:   FTB-7223B-B-EI
SERIAL_NUMBER:   131824-3B
WAVELENGTH:   1310.0 (SM)
DISTANCE_RANGE:   80.0000 km
PULSE_WIDTH:   28 m
ACQUISITION_TIME:  0.52 min
FIBER_INDEX:   1.4677
HELIX_FACTOR:   0.00 %
RBS_FACTOR:   -79.47 dB
JOB_ID:
CABLE_ID:
FIBER_ID:  18
FIBER_TYPE:
OPERATOR_A:
OPERATOR_B:

DATE:   2008/03/25
TIME:   14:33

NUMBER_OF_AVERAGED_POINTS:   500
                                        FAULT TABLE
------------------------------------------------------------------------------------
No,Loc(km),Event Type,Loss(dB),Refl(dB),Atten(dB/km),Cumul(dB)
 1,0.0000,Launch Level,- - -,-39.2,, 0.000
,,Fiber section  (15.1969 km), 5.026,, 0.331, 5.026
 2,15.1969,Reflective Fault, 0.292,-49.8,, 5.317
,,Fiber section  (15.2633 km), 4.935,, 0.323,10.252
 3,30.4603,Reflective Fault, 1.582,-46.1,,11.835
,,Fiber section  (20.2779 km), 6.327,, 0.312,18.161

  Link Loss: 18.16 dB    Link Length: 50.7382 km    Average Loss: 0.358 dB/km

POS(km)  VAL(dB)
0.0000 28.7344
0.1583 25.9137
0.3166 25.8626
0.4749 25.8006
0.6332 25.7422
   .       .
   .       .
   .       .
```

(b) Contoh fail ASC dalam Notepad

Rajah 5: Contoh hasil pengujian rangkaian dalam fail TRC dan ASCII

Dalam keadaan baik, tiada kehilangan atau kejatuhan kuasa optik berlaku dan satu mesej '*Good condition*' terpapar pada kerangka status talian (*Line's Status*) dalam tetingkap *Line's Detail*. Sebaliknya satu mesej '*Decreasing y dB at z km*' terpapar untuk memaklumkan kejatuhan kuasa optik dan lokasi kehilangan dalam talian tersebut. Dalam keadaan rosak, tiada sebarang nilai dapat dikesan daripada kejadian '*Reflective Fault*', maka satu mesej kerosakan '*Line x FAILURE at z km from CO!*' dipaparkan dalam tetingkap *Line's Status* dan *Line's Detail* untuk memberitahu lokasi kerosakan talian. Dengan ini, CFDS dapat membezakan setiap status talian penghantaran dalam sistem rangkain FTTH semasa menganalisiskan hasil pengujian OTDR.

Keterangan lanjut mengenai analisa akan diperolehi dalam tetingkap *Line's Detail* apabila menklik pada individu talian tersebut. Antara maklumat-maklumat yang akan dipaparkan termasuk kuasa optik, kehilangan, pengecilan yang berlaku dalam rangkaian tersebut berserta dengan lokasi elemen yang mendorong pengecilan kuasa tersebut dan maklumat-maklumat lain seperti mana yang terpapar pada skrin OTDR. Semua maklumat-maklumat ini bergantung kepada hasil pengujian yang didapati melalui pengukuran dengan OTDR dan ditunjukkan dalam unit-unit yang telah ditetapkan. Dengan ini, sebarang kerosakan yang berlaku dalam sistem rangkaian boleh dikesan dan ditentukan dengan kehilangan kuasa optik yang mendadak.

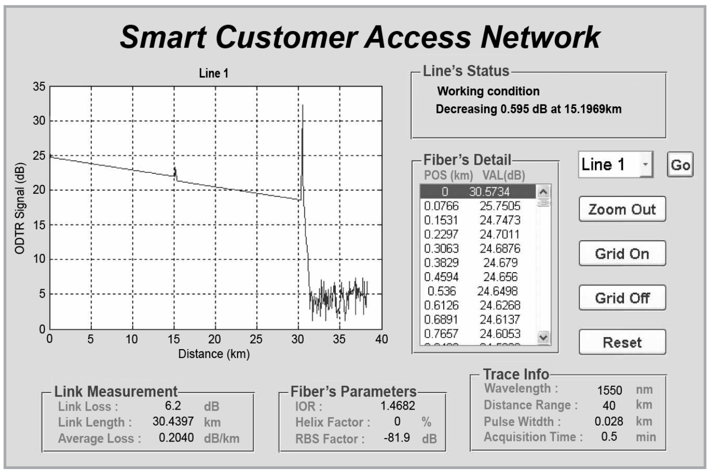

Rajah 8: Hasil pengujian talian 1 yang berada dalam keadaan baik. Satu mesej 'Working condition' dan 'Decreasing 0.595 dB at 15.1969 km' terpapar di kerangka status talian (Line's Status) dalam tetingkap Line's Detail untuk memaklumkan kejatuhan kuasa optik dan lokasi kehilangan dalam talian 1.

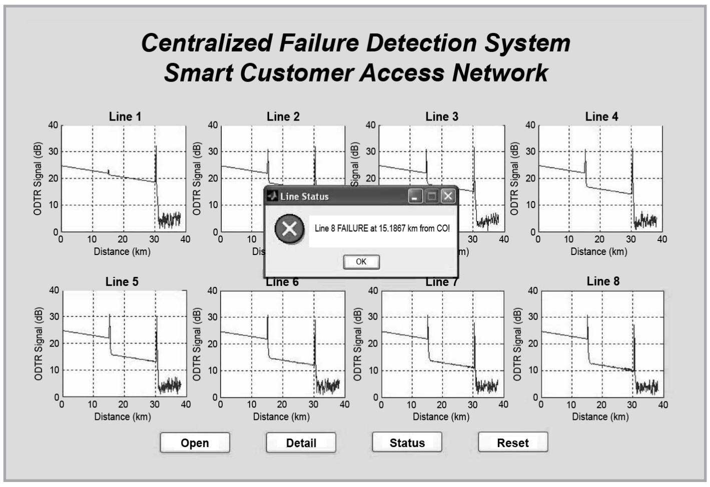

Rajah 6: Multi paparan hasil pengujian rangkaian optik pertama dalam tetingkap Line's Status untuk - pemantauan secara terpusat di CO (terdapat satu kerosakan berlaku pada talian 8 di jarak 15.1867 km)

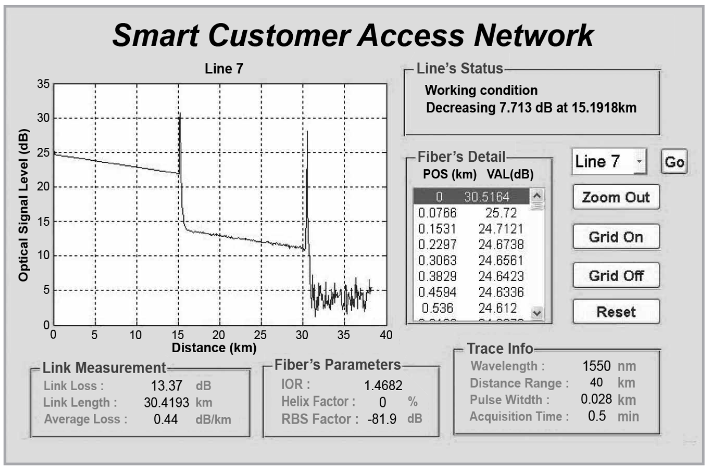

Rajah 9: Hasil pengujian talian 7 yang berada dalam keadaan baik dengan kejatuhan kuasa optik sebanyak 0.7.713 dB pada jarak 15.1969 km.

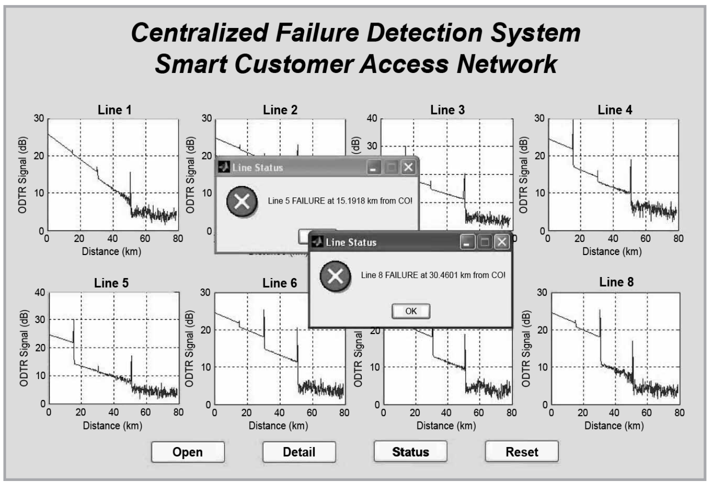

Rajah 7: Multi paparan hasil pengujian rangkaian optik kedua dalam tetingkap Line's Status untuk pemantauan secara terpusat (terdapat dua kerosakan berlaku pada talian 5 di jarak 15.1918 km dan talian 8 di jarak 30.4601 km)

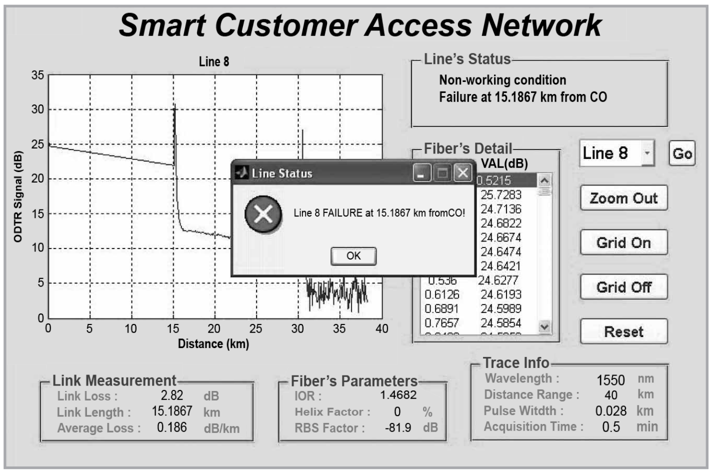

Rajah 10: Talian 8 mengalami kerosakan pada jarak 15.1867 km. Satu mesej 'Non working condition' dan 'FAILURE at 15.1867 km from CO' terpapar di kerangka status talian dalam tetingkap Line's Detail untuk memaklumkan lokasi kerosakan yang berlaku dalam talian 8.

Semua hasil penganalisaan akan disimpan dalam pangkalan data untuk rujukan masa depan.

Seterusnya status dan maklumat kerosakan dalam sistem rangkaian akan dihantar kepada pengendali perkhidmatan dan keterangan lanjut mengenai kerosakan talian akan dihantar kepada jurutera tapak untuk mengambil tindakan yang selanjut melalui teknologi wayarles seperti telefon bimbit atau komputer WiFi / Internet. Sementara itu, trafik dalam talian yang rosak akan dialihkan ke talian perlindungan (*Protection Line*) untuk mengekalkan aliran trafik. Dengan adanya CFDS, kedudukan atau lokasi kerosakan dalam rangkaian yang diuji dapat ditentukan dengan mudah dan cepat tanpa membazirkan wang dan masa.

3.0 PAPARAN PROGRAM YANG DIBANGUNKAN

CFDS memuatkan semua hasil ujian dari pangkalan data ke dalam *MATLAB Current Directory* semasa butang *Open* dalam tetingkap *Line's Status* ditekan. Setiap lapan graf yang mewakili ciri-ciri talian dalam rangkaian optik diplotkan untuk pemantauan terpusat, di mana paksi-x menunjukkan jarak (km) dan paksi-y menunjukkan aras kuasa optik (dB). Satu mesej kerosakan yang menunjukkan talian yang rosak bersama dengan lokasi kerosakan akan terpapar seperti ditunjukkan dalam Rajah 6 dan 7 apabila CFDS mengesan sebarang kerosakan dalam sistem rangkaian tersebut. CFDS melancarkan tetingkap *Line's Detail* untuk memaparkan maklumat talian yang lebih terperinci semasa menekan butang *Detail* dalam tetingkap *Line's Status* seperti ditunjukkan dalam Rajah 8 hingga 10.

4.0 KESIMPULAN

CFDS telah berjaya dibangunkan untuk membantu pengendali-pengendali perkhidmatan FTTH dan juga jurutera-jurutera tapak untuk memantau status setiap talian optik dan mengesan sebarangan kerosakan yang berlaku dalam sistem rangkaian FTTH secara terpusat pada CO dalam halaan menurun. Dengan adanya CFDS ini, setiap kerosakan yang berlaku dalam rangkaian FTTH boleh dikesan dan kerja penyelesaian masalah juga dapat diproseskan dengan secepatnya. Secara langsung, ini boleh mengurangkan kos dan masa penyelenggaraan, sebaliknya meningkatkan keberkesanan, kelengkapan, kebolehharapan dan keselamatan rangkaian FTTH.

5.0 PENGHARGAAN

Projek penyelidikan ini disumbang oleh Kementerian Sains, Teknologi dan Inovasi, Kerajaan Malaysia, melalui Dana Sains Kebangsaan (NSF) 01-01-02-SF0493. ■

RUJUKAN

[1] C.H. Yeh and S. Chi, "Optical Fiber-fault Surveillance for Passive Optical Networks in *S*-band Operation Window", *Optics Express*. 13(14):5494-5498, 2005.

[2] G. Keiser, *Optical Fiber Communication*, 3rd ed. New York: McGraw Hill Inc, 2000.

[3] K.L. Lee, S.B. Kang, D.S. Lim, H.K. Lee, and W.V. Sorin, "Fiber Link Loss Monitoring Scheme in Bidirectional WDM Transmission using ASE-injected FP-LD", *IEEE Photon. Technol. Lett.,* Vol. 18, No. 3, pp. 523-525, 2006.

[4] C.H. Yeh, C.S. Lee, and S. Chi, "A Protection Method for Ring-type TDM-PONs Against Fiber Fault", *Proc. of Optical Fiber Communication and the National Fiber Optic Engineers Conference (OFC/NFOEC 2007)*, 25-29 March, 2007, Anaheim, CA, JThA76.

[5] C.K. Chan, F. Tong, L.K. Chen, K.P. Ho, and D. Lam, "Fiber-fault Identification for Branched Access Networks Using a Wavelength-sweeping Monitoring Source", *IEEE Photon. Technol. Lett.*, Vol. 11, No. 5, pp. 614-616, 1999.

[6] D.R. Anderson, L. Johnson, and F.G. Bell, *Troubleshooting Optical Fibre Networks Understanding and Using Optical Time-domain Reflectometers*, California, US: Academic Press, Elsevier, 2004.

[7] J. Prat, "Optical Networks: Towards Bandwidth Manageability and Cost Efficiency", Available: http://www.e-photon-one.org/ephotonplus/servlet/Utils.MostrarFitxerPublic?fitxer=D_VD-A_3.pdf&pathRelatiu=E-Photon+One+%2B%2FPublic%2FPublic+Deliv erables%2F, 2007.

[8] I. Sankawa, S.I. Furukawa, Y. Koyamada, and H. Izumita, "Fault Location Technique for In-service Branched Optical Fiber Networks", *IEEE Photon. Technol. Lett.*, Vol. 2, No. 10, pp. 766-768, 1990.

[9] A. Girard, *FTTX PON Technology and Testing*, Quebec City, Canada: EXFO Electro-Optical Engineering Inc, 2006.

PROFILES

NG BOON CHUAN

Ng Boon Chuan received the B.Eng. in Communication and Computer Engineering from Universiti Kebangsaan Malaysia (UKM) in 2008. He is now pursuing his M.Sc. degree in Electrical, Electronics and Systems Engineering at UKM. His research interests focus on optical communication, intelligent network, and network management, in which he had authored several publications and conference presentations. Recently, he was involved with the research, development, and application of optical networking technology in intelligent fiber-to-the-home (i-FTTH). The majority of his time was spent in the Networking System Laboratory (NetLab), UKM.

MOHAMMAD SYUHAIMI AB-RAHMAN

Mohammad Syuhaimi Ab-Rahman received his B.Eng., M.Sc. and Ph.D. degrees in Electrical, Electronics and Systems Engineering from Universiti Kebangsaan Malaysia (UKM), Malaysia, in 2000, 2003 and 2007 respectively.

He joined the Institute of Micro Engineering and Nanoelectronics (IMEN), UKM in 2003. Currently, he is a senior lecturer in Faculty of Engineering and Built Environment, UKM. He is also an associated research fellow of IMEN since 2006. His current research interests are in the area of photonic networks and optical communication technologies such as optical security nodes, device fabrication, photonic crystal, laser technology, active night vision, plastic optical fiber, fiber in automotive, FTTH, and optical code division multiplexing (OCDM). The current and interest project is development of survivability and smart network system for customer access network, which also named as intelligent FTTH (*i*-FTTH), collaborated with Ministry of Science, Technology and Innovation (MOSTI), Government of Malaysia.

EMAIL TO THE EDITOR

A critical review of ***"Development and behaviour of light weight foamed concrete wall panel"*** by Mohd Arif Sulaiman, Siti Hawa Hamzah, Sabarudin Mohammad, Rokiah Othman and Alex Liew Chung Meng.

This article was published on ***IEM Journal, March 2009, Vol 70 No. 1 (pp. 14 – 20)***. Ir. Tu Yong Eng requested a thorough study on the article was carried out and the followings required for further clarification from the author:

[1] *Light weight foamed concrete* (LFC) is not even concrete, but rather mortar. Reference to concrete codes may not be suitable. Please refer to Section 5, BS 8110 – 2.

[2] For the experimental set-up, the description, figure 1 and figure 2 are different. Based on Figure 2, the effective height will be very much reduced. Furthermore, the effect of the supports shall be thoroughly studied to understand its effect.

[3] The loading arrangement may not be able to produce uniform loading condition. (*i.e.* steel bar welded to steel plate). Stress concentration may be induced.

[4] Actual density of LFC is not given. This may be crucial if the variance of the density is too high.

[5] Insufficient test cubes were prepared and hence variation of the strength can not be ascertained. Furthermore, the characteristic strength of the LFC cannot be ascertained as well.

[6] Results for T6 and T7 were not given. It should be a good comparison and an indication for the behaviour of the edge.

[7] Initial curvature is not measured. This is an important parameter since the comparison of the capacity was made to BS 8110 and ACI308 where the initial curvature has already taken into considerations. Furthermore, initial curvature will determine the direction of the horizontal deflection after loading.

[8] Initial eccentricity is also not measured.

[9] For the stress strain relationship, it is expected that uniform stress is used instead of actual stress at the location of the strain gauge. This estimation may not be accurate enough since the wall has high curvature after loading.

[10] W1400 and W1600 at Figure 7 looks mixed up. Please clarify.

[11] By comparing plots for S1W1400 and S2W1400 (as well as S1W1600 and S2W1600) in figure 7 also suggested that the location of the strain gauges may not be suitable. The results were inconsistence.

[12] It is strange to compare the modulus of LFC (with such a low strength) with conventional concrete of grade 30 (C30 concrete).

[13] Brittleness is not measured by modulus of elasticity. Hence, the last sentence of paragraph 3.3 is not justified.

[14] Failure debris does not necessarily shown that it was buckling failure because buckling normally shown the crushing at (or near to) the mid span. Confirmation of the mode of failure needed.

[15] Lateral displacement also shown that the LFC wall is weak for eccentricity loading.

[16] f_{cu} in formula (2) (ACI 308) should be cylindrical strength, and not the cube strength. *Likewise* for formula (3) and (4).

[17] Formula (5) (equation 44 in BS 8110, part 1) is also not correct. It should be $2e_a$ instead of $3e_a$.

[18] To have meaningful comparisons with BS 8110 and ACI 308, proper eccentricity and curvature shall be simulated, otherwise the ultimate strength will be over estimated. Factor of safety was built into the formulae of BS 8110 and ACI 308. For a meaningful comparison, these factors shall be removed.

[19] Reference is made to Section 5.8.3, BS 8110 part 2 for light weight aggregate concrete, e_a for equation 44 of BS 8110 part 1 shall be revised to $l_e/1700h$. (most probably $l_e^2/1700h$) (*Remark:* This is for comparison purposes only, since BS 8110 did not provide guidelines to LFC).

[20] Tabulation of Table 4 seems to be incorrect. Please confirm. For example, based on formula (2) and (3), ultimate strength predicted by ACI is actually higher than that of Orberlender and Overard but shown otherwise in Table 4.

[21] Since the failure is expected to be buckling, why Euler buckling load was not computed?

[22] First sentence of the *conclusion - What is* "lightweight forward concrets"?

[23] Is it significant to compare test cube strength between C1400 and C1600 based on single sample result?

[24] Two wall panel - . *What* is the effect of the variation of the strength of the material, initial curvature and eccentricity?

• Author's reply

Your critical review on ***'Development and behaviour of light weight foamed concrete wall panel'*** is highly appreciated and we regret some of the mistakes occurred in this article as pointed out by you. Your comments become serious matter to us and we are highly concern. In actual fact, this particular article is the preliminary study for the lightweight foamed concrete wall panel because the use of the light weight foamed concrete is relatively new in Malaysia and there is no set of standard which provide us with clear guideline to follow or to refer to just as yet.

With that said, our response to your comment is as follow;

[1] The density of *light weight foamed concrete* (LFC) ranges between 300 kg/m^3 to 1800 kg/m^3. According to LCM Sdn.Bhd and BCRC, the densities for wall panel are recommended to be in the range of 1400 kg/m^3 to 1600 kg/m^3. Therefore this study was carried out to investigate the structural behavior of lightweight foamed concrete wall panel in term of ultimate load and mode of failure.

[2] Table 2 presents the average compressive strength for LFC cube test. A series of cubes were tested at age 7, 14, 28 and 60 days whereby 3 cube specimens were tested each day.

[3] The experiment was set-up at the Heavy Structures Laboratory, Faculty of Civil Engineering, UiTM Malaysia. Figure 1 and Figure 2 represent the experimental set-up and arrangement of LVDTs respectively. In this study, the arrangement of LVDT's and ESG's was adopted from Siti Hawa Hamzah at al. (*Wire Fabric Reinforced Concrete Wall Panel., World Housing Congress, Terengganu, Malaysia 1-5 July 2007*).

[4] The loading system was well designs and the loads were well distributed. The Figure A shows the cast iron trapezium shape was tight to the load cell. The steel bar was welded to steel plate to make sure that the wall panel tested under pure axially load (*eccentricity* = 0).

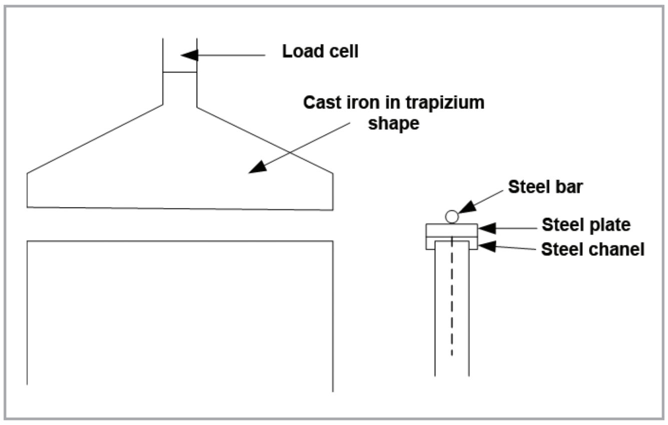

Figure A

[5] Table 4 shows the comparison between experimental and theoretical values of ultimate load for wall panel. We concur that a few mistakes occur in the Formula (2), (3) and (4) were due to our *'misinterpretation'* of the value of the fcu. Benayoune at al (Respond of pre-cast reinforced composite sandwhich panel to axial loading sciece direct) also defined f_{cu} in the formula as a compressive strength of cube concrete not cylinder concrete.

[6] In Formula (5), it should be read as $2e_a$ instead of $3e_a$. By recalculating, the ultimate load should be 286.90 kN and 203.66 kN for wall panel W1600 and W 1400 respectively.

[7] The wall panel was failed by abrupt fracture but referring to the lateral displacement profile, the wall panel also failed by buckling.